九州大学学術情報リポジトリ
Kyushu University Institutional Repository

Deposition Mechanism and Characterization of a-C:H Films Deposited using Ar + H2 + C7H8 Plasma CVD

董, ?

https://doi.org/10.15017/1654913

出版情報：九州大学, 2015, 博士（学術）, 課程博士
バージョン：
権利関係：全文ファイル公表済

Deposition Mechanism and Characterization of a-C:H Films Deposited using Ar + H_2 + C_7H_8 Plasma CVD

Xiao Dong

Department of Electrical and Electronic Engineering

Graduate School of Information Science and Electrical Engineering

Kyushu University

December 2015

Ar + H_2 + C_7H_8 プラズマ CVD で形成した a-C:H 薄膜の成長機構と特性評価

董 琥

九州大学大学院

システム情報科学府

電気電子工学専攻

平成 27 年 12 月

Abstract

Extreme ultraviolet (EUV) lithography at 13.5 nm is the major candidate of next-generation lithography technologies for printing the intricate patterns onto semiconductor wafers. The shallow depth of focus (DOF) of EUV lithography requires thin photoresist films, which leads to worse plasma etch resistance of them. Formation of protective coatings on the surface of EUV photoresists is one of the methods to solve this issue. Moreover, the rapid growth of sub-14 nm multigate devices in semiconductor industry requires a new process. It is able to bring about high deposition rate under atmospheric condition without vacuum pump, and to realize anisotropic deposition profiles to overcome resolution limit of EUV lithography. Hydrogenated amorphous carbon (a-C:H) is one of the most important materials used as protective coatings in manufacturing multigate devices due to their wide range of electronic, optical, and mechanical properties. Therefore, the study of depositing a-C:H film on EUV photoresists as protective coatings by anisotropic high-speed method is crucial to develop sub-14 nm multigate devices. Here, we investigated deposition mechanism of a-C:H films using Ar + H_2 + C_7H_8 plasma CVD, and characterized H content and bonding configurations in the deposited films.

From the study on emission intensities by optical emission spectroscopy, it is found that the generation rates of plasma species are higher near the mesh powered electrode of the main discharge. The effective electron temperature decreases significantly with increasing the total pressure from 0.1 to 5 Torr, while it is independent on discharge voltage and gas flow rate ratio. The Ar $1s_5$ metastable density and/or low-energy electron density decrease with increasing the total pressure from 0.1 to 5 Torr and with increasing the gas flow rate ratio ($R = [H_2]/([H_2] + [Ar])$) from 11 to 55%, while they increase with increasing the discharge voltage from 150 to 180 V. Moreover, all of them are almost

constant irrespective of the spatial distance.

From the study of improving deposition rate, it is 25.5 times as high as previous results. The balance between deposition rate of carbon-containing neutral radicals and etch rate by H atoms determines net deposition rate. Bombardment of ions hardens films, and decreases the etch rate. The highest deposition rate of 94.5 nm/min is obtained under the conditions of gas pressure of 5 Torr, discharge voltage of 170 V, gas flow rate ratio of 11%, and spatial distance of 20 mm from the substrate electrode. By control of carbon-containing neutral radical flux and ion flux, we have succeeded in depositing high mass density a-C:H films with a high deposition rate.

From the study of ion bombardment effects, we find the threshold ion energy of structural transition of a-C:H films from soft polymer-like a-C:H (PLCH) to hard diamond-like a-C:H (DLCH) is 84 eV. The mass density of PLCH films deposited from without ion bombardment to the ion energy of 84 eV only depends on C−H sp^3 to C−H sp^2 ratio (H content) in films, while the mass density of DLCH films deposited in the ion energy range of 84 to 114 eV simultaneously depends on C−H sp^3 to C−H sp^2 ratio (H content) and C−C sp^3 to C=C sp^2 ratio in films. The highest mass density of 1.92 g/cm^3 is obtained at the ion energy of 109 eV. In addition, we succeeded in depositing a-C:H films on poly(methyl methacrylate) (PMMA) at a low substrate temperature of 100℃.

Table of Content

Chapter 1 Introduction 1
1.1 Amorphous Carbon 1
1.1.1 Thin Film Coating 1
1.1.2 Different Forms of Amorphous Carbon 1
1.2 Deposition Mechanism of a-C:H Films 6
1.3 Background and Motivation 10
1.3.1 Extreme Ultraviolet Lithography 10
1.3.2 Minimal Fabrication 16
1.3.3 Anisotropic Deposition 18
1.3.4 Objectives 20
1.4 Outline of Thesis 22
References: 23

Chapter 2 Experimental Methods 28
2.1 a-C:H Film Deposition 28
2.2 Plasma and Film Characterization 31
2.2.1 Optical Emission Spectroscopy 31
2.2.2 Scanning Electron Microscopy 35
2.2.3 Fourier Transform Infrared Spectroscopy 36
2.2.4 Elastic Recoil Detection Analysis 37
2.2.5 Raman Spectroscopy 38
2.2.6 X-ray Photoelectron Spectroscopy 39
2.3 Ion Energy and Plasma Potential 40
References: 43

Chapter 3 Emission Spectroscopy of Ar + H_2 + C_7H_8 Plasmas 46
3.1 Introduction 46
3.2 Experimental Details 46
3.3 Results and Discussion 48
3.4 Summary 53
References: 54

Chapter 4 Effects of Gas Pressure, Discharge Voltage, and Gas Flow Rate Ratio on the formation of a-C:H Films 55
4.1 Introduction 55
4.2 Effects of Gas Pressure for Film Deposition 56
4.2.1 Experimental Details 56
4.2.2 Results and Discussion 57
4.2.3 Summary 60
4.3 Effects of Discharge Voltage for Film Deposition 60
4.3.1 Experimental Details 60
4.3.2 Results and Discussion 61
4.3.2.1 Hydrogen bonding configuration 61
4.3.2.2 Hydrogen content in films 65
4.3.2.3 Plasma parameters 69
4.3.3 Summary 70
4.4 Effects of Gas Flow Rate Ratio for Film Deposition 71
4.4.1 Experimental Details 71
4.4.2 Results and Discussion 72
4.4.2.1 Optical emission intensity 72
4.4.2.2 Film deposition 74
4.4.2.3 Infrared absorption spectra of films 76
4.4.2.4 Hydrogen content in films 77

4.4.3 Summary 79
References: 80

Chapter 5 Effects of Ion Flux and Ion Energy on Characteristics of a-C:H Films 83
5.1 Introduction 83
5.2 Experimental Details 84
5.3 Results and Discussion 86
5.3.1 Spatial Profiles of Plasma Emission Intensities 86
5.3.2 Film Deposition 88
5.3.3 Infrared Absorption Spectra 90
5.3.4 XPS C1s Spectra 93
5.3.5 Bonding Configurations in Films 95
5.3.6 Hydrogen Content in Films 100
5.3.7 Raman Spectroscopy of Films 105
5.4 Summary 111
References: 112

Chapter 6 Deposition of a-C:H Films on PMMA 115
6.1 Introduction 115
6.2 Experimental Details 115
6.3 Results and Discussion 117
6.4 Summary 122
References: 124

Chapter 7 Conclusions and Future Recommendations 125
7.1 Conclusions 125
7.2 Future Recommendations 126
References: 128

Acknowledgements 129

List of Publications 130

Chapter 1 Introduction

1.1 Amorphous Carbon

1.1.1 Thin Film Coating

The environmental sustainability and life cycle costing have received increasing attention in chemical and material industry nowadays [1-4]. Surface engineering, which spans a wide range of processes, is a valuable technology to modify and improve the surface properties of materials in achieving both of these [5-6]. By covering the underlying material (substrate) with another material, surface engineering alters or enhances the properties of the original material such as electrical, mechanical, chemical, and optical.

The covering material as a layer with thickness ranging from fractions of a nanometer (monolayer) to several micrometers is called thin film [7]. The desired properties for required applications of thin films are commonly synthesized by physical vapor deposition (PVD) and chemical vapor deposition (CVD) [8,9]. Electronic semiconductor devices and optical coatings are the main applications benefiting from thin film coating.

As one of the representative materials in thin film coating, carbon ranging from fullerene (C_{60}) [10], carbon nanotube (CNT) [11], carbon nanowalls [12,13], graphene [14-17], and amorphous carbon (a-C) [18-19] can be found everywhere in our surroundings. All kinds of these structures exhibit unique and adjustable properties, thus they are widely concerned and studied in the fields of developing novel nanomaterials and new devices [20,21].

1.1.2 Different Forms of Amorphous Carbon

The a-C films, owing to their high mechanical hardness, optical transparency, chemical inertness, and biological compatibility, have been widely used as protective coatings in areas of silicon wafers, disk storage, hip joint, micro-electromechanical systems, Ge windows, car parts, etc [22-26]. This is because of the ability of a-C forms a variety of crystalline and disordered structure to contain a mixture of sp^3 (diamond-like), sp^2 (graphite-like), and even sp^1 configurations [27-29].

In the sp^3 configuration as in diamond, four valence electrons of a carbon atom are assigned to sp^3 hybrid orbital respectively, which forms strong σ bond with adjacent atoms as shown in Fig. 1.1 [30]. It is also known as the tetrahedral structure of diamond, this structure with directional σ bond leads diamond to have superior mechanical properties, higher atom density, larger thermal conductively in room temperature, and smaller thermal expansion coefficient as compared to other materials.

In the sp^2 configuration as in graphite, three of the four valence electrons of a carbon atom enter sp^2 hybrid orbital, which forms σ bond in a trigonal plane as shown in Fig. 1.2 [30]. The fourth electron forms a weaker π bond with one or more neighboring carbon atoms, lying in normal to the σ bonding plane. These π bonding atoms are attracted to each other by the weak van der Waals forces resulting in the layered structure of graphite.

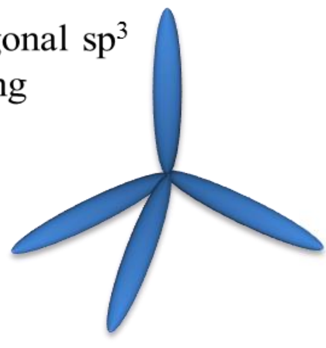

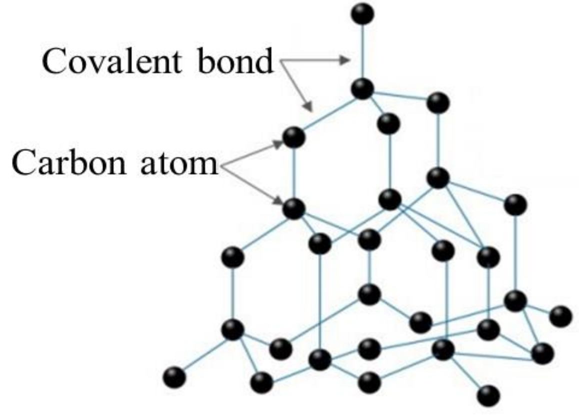

Fig. 1.1. sp^3 hybridized bonding and structure of diamond [30].

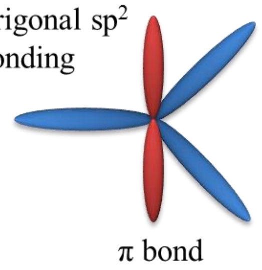

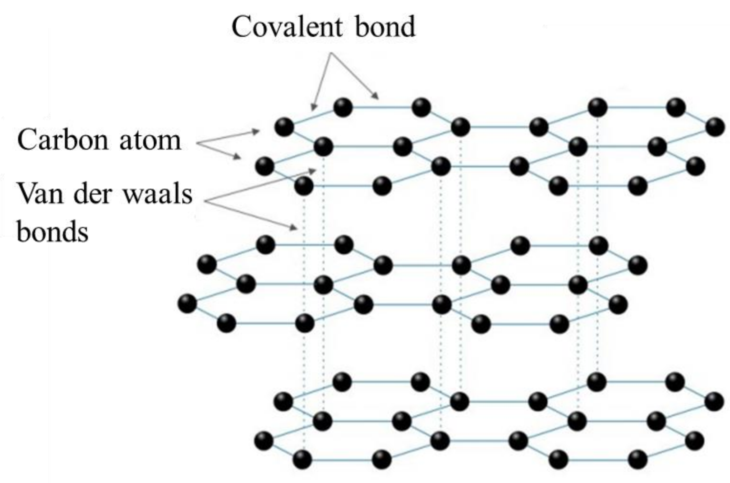

Fig. 1.2. sp^2 hybridized bonding and structure of graphite [30].

The a-C films are composed of two groups based on the atomic H content, H-free amorphous carbon (a-C) and hydrogenated amorphous carbon (a-C:H). Owing to the atomic H content passivates the dangling bonds in amorphous structure and thus affects the chemical bonding configuration, it plays a crucial role in optical properties, electrical properties and internal stresses of films [31]. In this present work, we classify a-C:H films into three types as shown in Fig. 1.3 [32,33].

(1) a-C:H with high sp^3 configurations (~60%) and a high hydrogen content (40–60 at.%) is called polymer-like a-C:H (PLCH) [34]. In PLCH, the majority of sp^3 configurations are hydrogen-bonded and it is soft. PLCH films have a low mass density of 1.2–1.6 g/cm^3 deposited by plasma CVD at low bias voltage [35].

(2) a-C:H with lower overall sp^3 configurations (~40%) and an intermediate hydrogen content (20–40 at.%) is called diamond-like a-C:H (DLCH) [32]. Owing to the presence of more C–C sp^3 configurations in DLCH than in PLCH, DLCH has a mass density of 1.6–2.2 g/cm^3 and it is hard. DLCH films are usually deposited by plasma CVD, electron cyclotron resonance (ECR), or reactive sputtering at moderate bias voltage [36,37].

(3) a-C:H with high sp^2 configurations and a low hydrogen content (<20 at.%) is called graphite-like a-C:H (GLCH). GLCH films are usually deposited by plasma CVD at high bias voltage [32], dc glow discharge (GD) systems [38], or magnetron sputtering (MS) [39].

Typical properties of these types of a-C:H films compared to diamond, graphite, and other forms of carbon are summarized in table I [40-43].

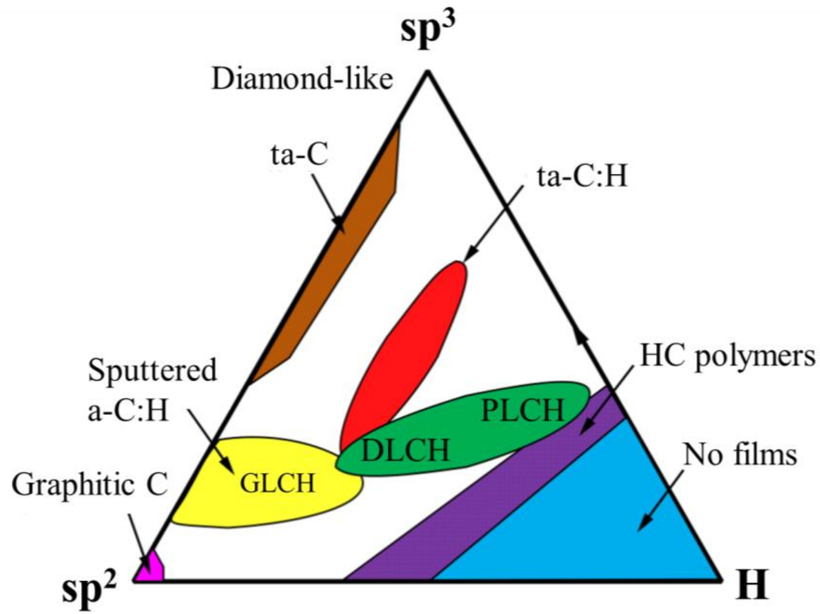

Fig. 1.3. Ternary phase diagram of various H free and hydrogenated amorphous carbon forms [32].

Table I. Comparison of major properties of a-C:H films with diamond, graphite, and other forms of carbon [40-43].

	sp^3 (%)	H (at.%)	Density (g/cm^3)	Gap (eV)
Diamond	100	0	3.515	55
Graphite	0	0	2.267	0
Glassy C	0	0	1.3–1.55	0.01
Evaporated C	0	0	1.9	0.4–0.7
Sputtered C	5	0	2.2	0.5
ta-C	80–88	0	3.1	2.5
a-C:H hard	40	20–40	1.6–2.2	1.1–1.7
a-C:H soft	60	40–60	1.2–1.6	1.7–4
ta-C:H	70	30	2.4	2.0–2.5

1.2 Deposition Mechanism of a-C:H Films

The C–C sp^3 to C=C sp^2 ratio plays the most important role in the properties of a-C:H films. The concentration of sp^3 configurations is depended on the ion energy and depositing species [44]. The highest sp^3 fractions are considered to be formed with ion energy around 100 eV [32]. Moreover, the variation of sp^3 fractions with ion energy for each source gas (such as CH_4, C_2H_2, C_2H_4, and C_6H_6) can be redefined on a scale of ion energy per C atom in that molecule [45]. It is elaborated as follows. When an energetic molecular ion is bombarded on the growing film surface, it breaks up into atomic ions that bombard independently with evenly distributed energy.

Firstly, we describe the physical processes in the deposition of a-C films. A great variety of analytical and numerical simulations denoted the process of ions incident on surface of a-C films as subplantation (low energy subsurface implantation) [46-48]. On the basis of the elastic collisions of ions in solids are simplified as a sequence of independent pair collisions. The cross-section of the collisions decreases with increasing ion energy [49]. Thus, Owing to the large atomic radii and narrow interstices, the surface is as an impenetrable wall to block incident ions from penetrating the surface layer at low ion energy. At higher ion energy, the decreased atomic radii result in the wider interstices. So ions can pass through the interstices and penetrate the surface layer. The penetration threshold E_{p} which is the energy required to penetrate the surface layer is about 30 eV for carbon [50].

The carbon ions incident on the surface of a-C films is described in Fig. 1.4 [45]. The incident ions having energy $E_{\mathrm{inc}} < E_{\mathrm{p}}$ will not penetrate the surface, so they just reside on the surface and remain in the lowest energy state by forming sp^2 bonds. If the incident ions with higher energy than E_{p} ($E_{\mathrm{inc}} > E_{\mathrm{p}}$), they will penetrate the surface and enter subsurface which subplantation occurs in two different ways as shown in Fig. 1.5 [51]. The

indirect penetration by knock-on only occurs for the case of ion assisted deposition. On the assumption of in the highly energetic conditions of ion bombardment during film growth, the local bonding will reform around that atom according to the local density increased by subplantation. That is, atomic hybridizations will adjust to changes in the local density, becoming more sp^2 bonding while the local density is low and more sp^3 bonding while the local density is high.

The ion range increases with further increasing the ion energy. If the energy of incident ions is much higher than E_{p} ($E_{inc} \gg E_p$), the ions will penetrate deeper into the films. In this case, only a small fraction of energy is assigned to penetrate the surface. The excess energy is dissipated in atom displacements as the form of phonons (heat) resulting in the relaxation of the mass density [52]. This whole process consists of a collisional stage, a thermalization stage, and a relaxation stage. The processes of thermalization and relaxation relax the increased density and cause a loss of sp^3 bonding.

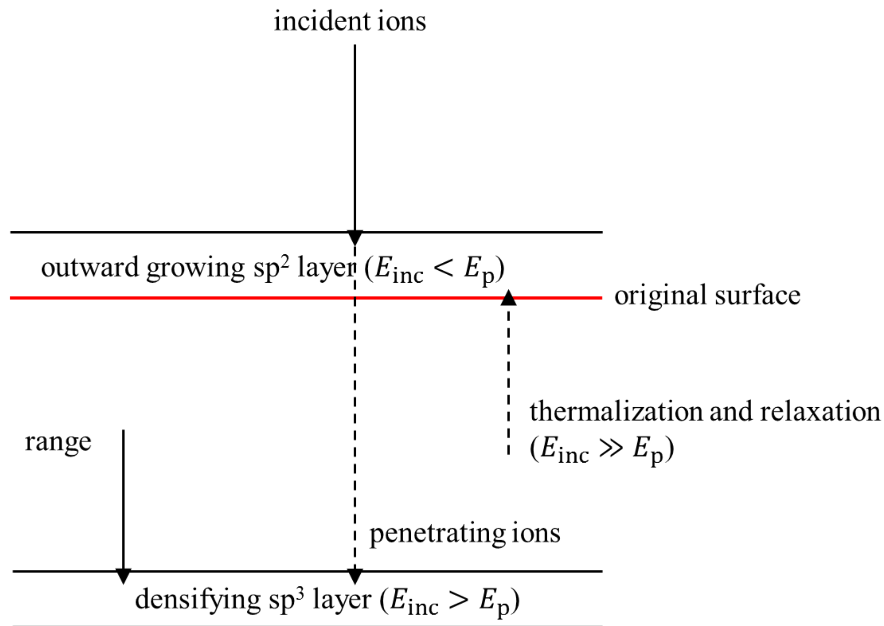

Fig. 1.4. Schematic diagram of densification by subplantation for the growth of a-C films [45].

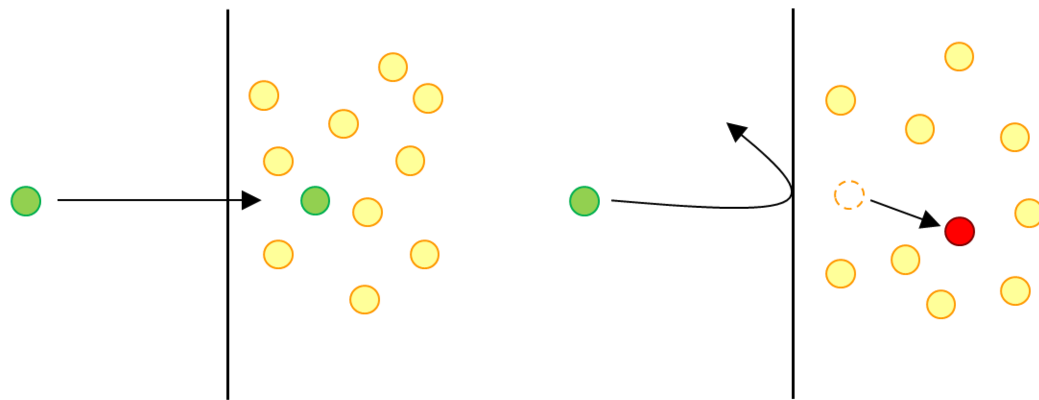

Fig. 1.5. Schematic of two processes of (a) direct penetration and (b) indirect penetration by knock-on in subplantation [51].

As well as the physical process of subplantation, there are many plasma enhanced chemical processes in the deposition of a-C:H films as shown in Fig. 1.6 [32]. The plasma deposition can be divided into the reactions in the plasma, the plasma-surface interaction, and the subsurface reactions [53]. The plasma species consist of carbon-containing neutral radicals (C_xH_y), ions, and H atoms. Figure 1.7 shows the deposition rate decreases with increasing the substrate temperature [54,55]. It is known that the etch rate by H atoms increases with temperature [56], whereas the deposition rate by carbon-containing neutral radicals and ions are independent on temperature, so the net deposition rate decreased with temperature.

The contribution of each carbon-containing neutral radical to the deposition rate depends on respective sticking coefficient [57]. Biradicals and other unsaturated species such as C_2H_4 and C_2H_2 can directly insert into the surface bonds, indicating strong reaction with the film. The effect of closed shell molecules such as CH_4 is negligible due to their low sticking coefficients. Monoradicals such as CH_3 can only react with dangling bond on the film surface to form a carbon-carbon bond. The dangling bond is created by removal of H (an ion displacing H, a H atom or a radical abstracting H) from a carbon-hydrogen bond

[58]. All of the carbon-containing neutral radicals can only react at the film surface.

Because of the small size and low mass of H atoms, they can penetrate into the film about 2 nm [59]. They abstract H from carbon-hydrogen bonds to create subsurface dangling bonds again. Moreover, some of these dangling bonds will be repassivated by H atoms. Hydrogen ions have the same effects with H atoms, whereas they penetrate deeper into the film than H atoms and reach the longest range. Besides subplantation, another important role of carbon and hydrocarbon ions in a-C:H film deposition is to displace H from carbon-hydrogen bonds. The dissociated H atoms recombine to form H_2 molecules, and eventually desorb from a-C:H films. It is the main process that causes dehydrogenation in a-C:H films with increasing the bias voltage during plasma CVD deposition.

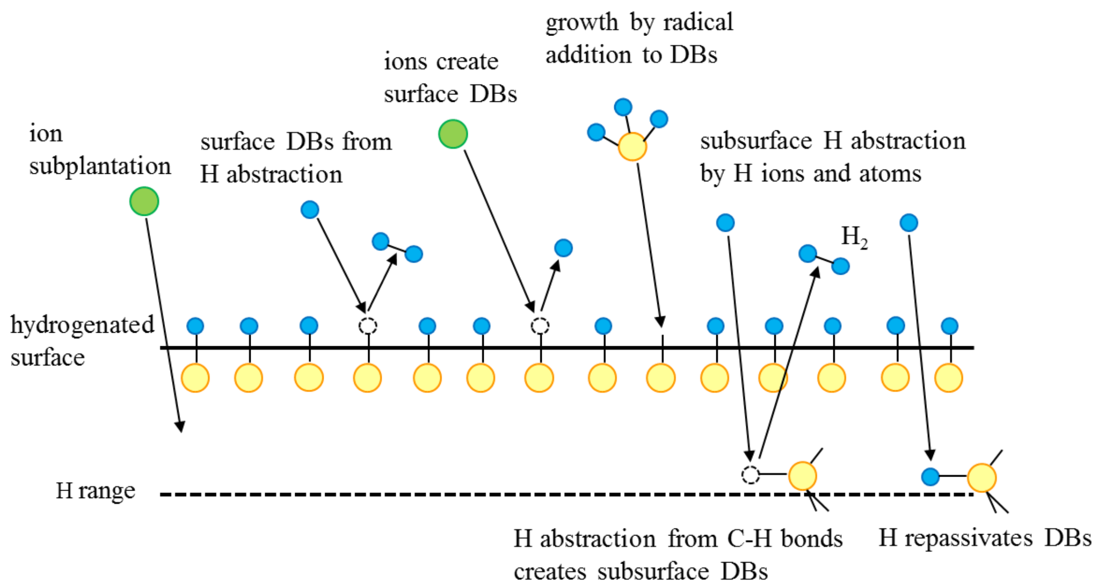

Fig. 1.6. Schematic of component processes in the deposition mechanism of a-C:H films [32].

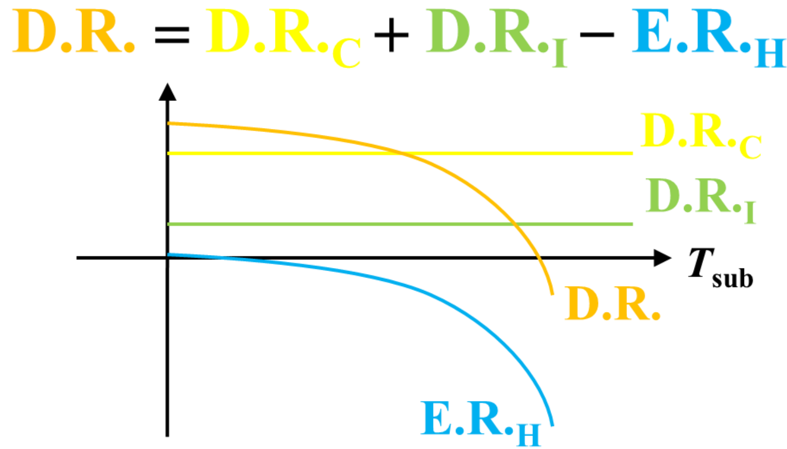

D.R.: experimental deposition rate
$D.R._C$: deposition rate by carbon-containing neutral radicals
$D.R._I$: deposition rate by ions
$E.R._H$: etching rate by H atoms

Fig. 1.7. Schematic of substrate temperature dependence of net deposition rate [54,55].

1.3 Background and Motivation

1.3.1 Extreme Ultraviolet Lithography

Lithography is a technology used to define integrated circuits by printing the intricate patterns onto semiconductor wafers. Extreme ultraviolet (EUV) lithography at 13.5 nm is the major candidate of next-generation lithography technologies for patterning integrated circuits as shown in Fig. 1.8 [60]. It involves a dramatic shrinking in wavelength compared with ArF immersion. EUV light sources taken out from high-temperature and high-density plasma have been under the development of laser produced plasma (LPP) and discharge produced plasma (DPP). The LPP method produces plasma by condensing a strong laser beam onto a certain material, and the DPP method produces plasma by a pulsed high-current discharge between electrodes in an atmosphere of certain material. Owing to the requirement of high-power in DPP, the LPP method is considered to be dominated in semiconductor factory for mass production.

For an imaging system, there are two fundamental characteristics: resolution (RES) and depth of focus (DOF) as shown in Fig. 1.9. These characteristics are usually expressed as [61]

$$\mathrm{RES} \propto \lambda/\mathrm{NA} = k_1\, \lambda/\mathrm{NA} \tag{1.1}$$

and

$$\mathrm{DOF} \propto \lambda/(\mathrm{NA})^2 = k_2\, \lambda/(\mathrm{NA})^2 \tag{1.2}$$

where λ is the wavelength of radiation, NA is the numerical aperture of the imaging system, k_1 and k_2 are constants depended on optics, photoresist, and process latitude (such as DOF and exposure latitude). From Eqs. (1,1) and (1.2) we can see that better resolution are achieved by reducing λ and increasing NA. However, the penalty for doing this is the decreased DOF.

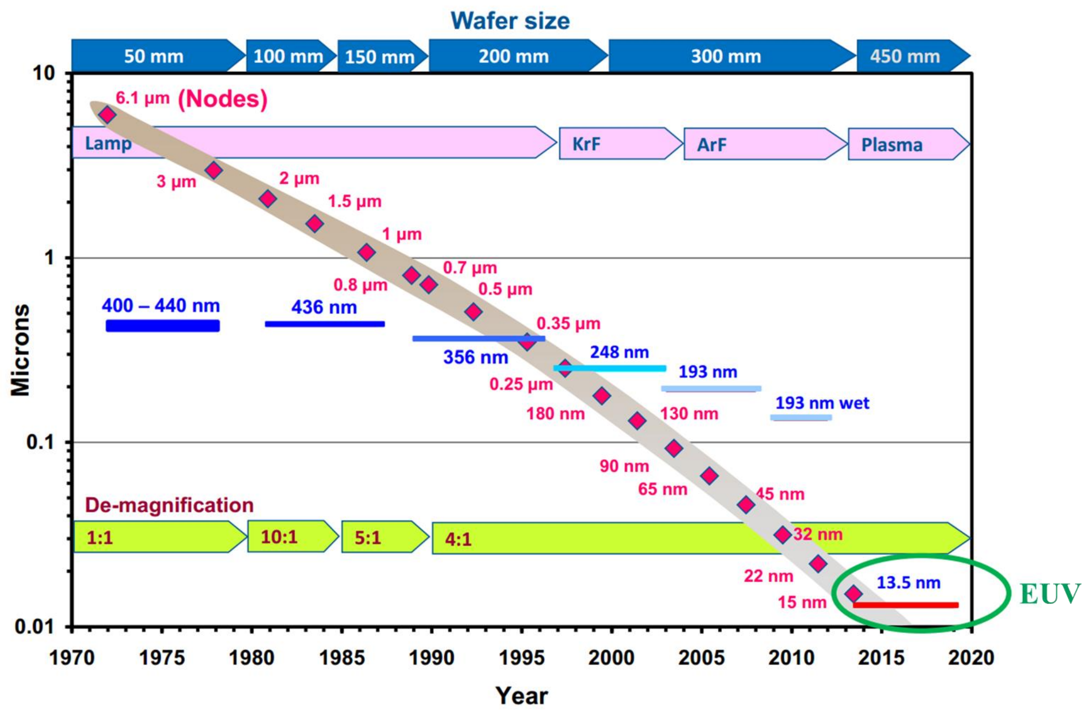

Fig. 1.8. Ramp-ups in chip scaling and lithography technology [60].

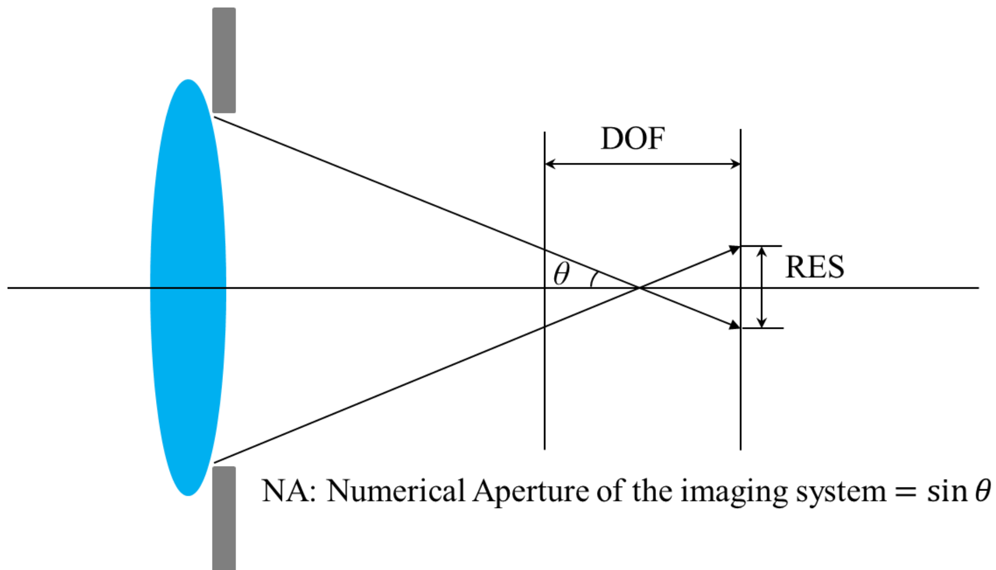

Fig. 1.9. Schematic diagram of resolution and depth of focus for an imaging system.

In lithography, the pattern printed on a wafer is not the completely same with the mask pattern in practice. Critical dimension (CD) is defined as the linewidth of photoresist line printed on a wafer and reflects whether the exposure and development are proper to produce geometries of the correct size. The CD loss, caused mainly by over-exposure or over-development, leads to most lithography reworks. Therefore, a desired CD control is essential for the achievement of high-volume manufacture and the final performance of the devices.

The k_1 and k_2 have a major impact on CD control. Historically, values of k_1 and k_2 greater than 0.6 have been comfortably used in high-volume manufacture. Recently, ever better resolution requires smaller values of k_1 and k_2 in the extending imaging technologies, which leads to the problem of poor CD control. As shown in Fig. 1.10, double patterning for ArF 193 nm immersion reduces k_1 via splitting of features or pattern, EUV (13.5 nm) lithography offers higher k_1 value and then improves optical image quality [62].

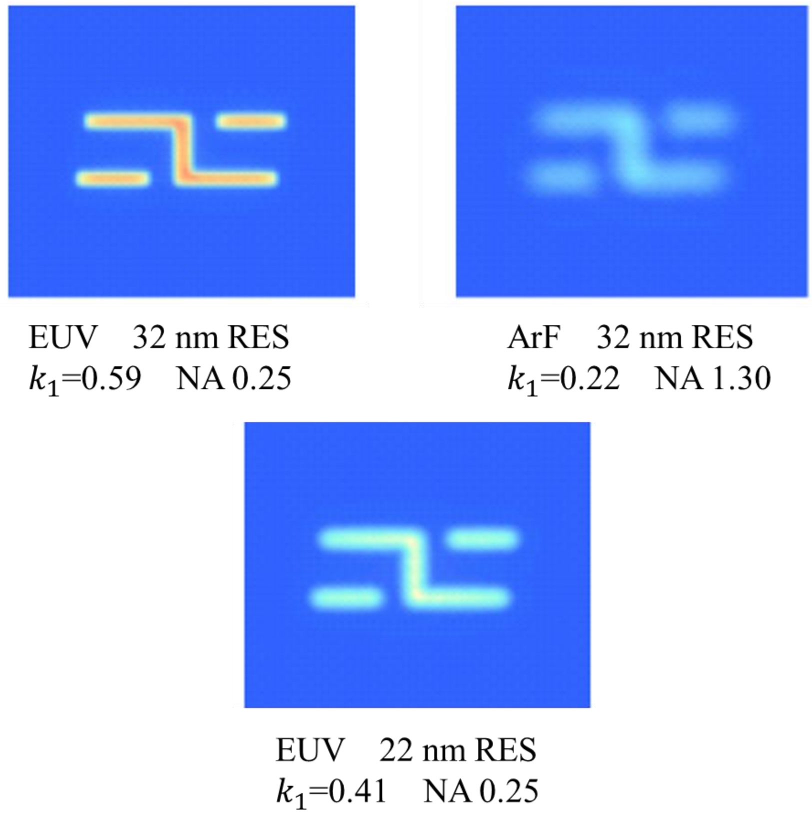

Fig. 1.10. k_1 value versus optical image quality [62]

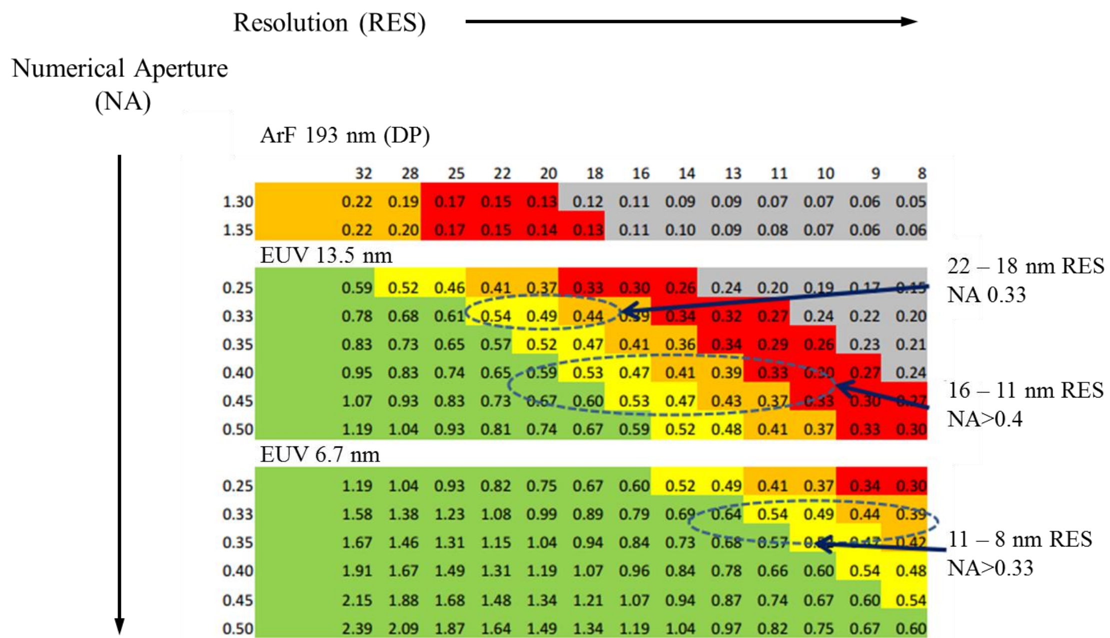

ArF 193 nm (DP)

NA	32	28	25	22	20	18	16	14	13	11	10	9	8
1.30	0.22	0.19	0.17	0.15	0.13	0.12	0.11	0.09	0.09	0.07	0.07	0.06	0.05
1.35	0.22	0.20	0.17	0.15	0.14	0.13	0.11	0.10	0.09	0.08	0.07	0.06	0.06

EUV 13.5 nm

NA	32	28	25	22	20	18	16	14	13	11	10	9	8
0.25	0.59	0.52	0.46	0.41	0.37	0.33	0.30	0.26	0.24	0.20	0.19	0.17	0.15
0.33	0.78	0.68	0.61	0.54	0.49	0.44	0.39	0.34	0.32	0.27	0.24	0.22	0.20
0.35	0.83	0.73	0.65	0.57	0.52	0.47	0.41	0.36	0.34	0.29	0.26	0.23	0.21
0.40	0.95	0.83	0.74	0.65	0.59	0.53	0.47	0.41	0.39	0.33	0.30	0.27	0.24
0.45	1.07	0.93	0.83	0.73	0.67	0.60	0.53	0.47	0.43	0.37	0.33	0.30	0.27
0.50	1.19	1.04	0.93	0.81	0.74	0.67	0.59	0.52	0.48	0.41	0.37	0.33	0.30

EUV 6.7 nm

NA	32	28	25	22	20	18	16	14	13	11	10	9	8
0.25	1.19	1.04	0.93	0.82	0.75	0.67	0.60	0.52	0.49	0.41	0.37	0.34	0.30
0.33	1.58	1.38	1.23	1.08	0.99	0.89	0.79	0.69	0.64	0.54	0.49	0.44	0.39
0.35	1.67	1.46	1.31	1.15	1.04	0.94	0.84	0.73	0.68	0.57	[illegible]	0.47	0.42
0.40	1.91	1.67	1.49	1.31	1.19	1.07	0.96	0.84	0.78	0.66	0.60	0.54	0.48
0.45	2.15	1.88	1.68	1.48	1.34	1.21	1.07	0.94	0.87	0.74	0.67	0.60	0.54
0.50	2.39	2.09	1.87	1.64	1.49	1.34	1.19	1.04	0.97	0.82	0.75	0.67	0.60

Fig. 1.11. k_1 factors, numerical aperture, and resolution for ArF and EUV [63].

One of the issues for introducing EUV lithography into industry manufacturing is the photoresists. As shown in Fig. 1.11 [63], owing to the dramatic shrinking in wavelength, DOF of EUV lithography with a feature size of 14 nm is just 31.3 nm ($k_1 = k_2$ =0.47, NA=0.45), and it will become even smaller at sub-14 nm feature size. The shallow DOF of EUV lithography requires thin photoresist films, which leads to worse plasma etch resistance of them. Moreover, each EUV photon carries 14 times as much energy as an ArF photon, the increased energy per photon means that fewer photons are available. An important potential source of line edge roughness (LER) for EUV photoresists is the photon shot noise aggravated by a random distribution of high photon energy [64]. The LER also increases as photoresist films get thinner.

Another issue for high-volume manufacture EUV lithography is related to the EUV light source. As the most promising solution, the CO_2 laser produced Tin plasma EUV light source (CO_2-Sn-LPP) requires output power of 200 W [65]. It is obvious that more output power will be required for smaller device feature sizes, which makes it difficult for the EUV light source system to operate continuously in a stable performance.

Owing to the requirement to simultaneously achieve the other characteristics such as low LER and high sensitivity for photoresists, the stable performance for EUV light source, development of high etch resistance EUV photoresists is difficult. We choose the method of formation of protective coatings on the surface of EUV photoresists to solve this issue. Etch rate ratio of protective coatings to photoresists is expected to be lower than 0.25. The a-C:H films have been widely used as protective coatings due to their mechanical hardness (~30 GPa), wide bandgap (1.1–4 eV), optical transparency (600 nm–50 mm), chemical inertness, and biological compatibility. There are four potential merits for a-C:H as coatings of photoresists. (1) Low substrate temperature (100℃) for deposition protects photoresists from thermal damages. (2) Mechanical hardness and chemical inertness

improves etch resistance of photoresists. Figure 1.12 shows mass density dependence of etch rate of a-C:H films. For both the reactors in Kyushu University and Nagoya University [66], the etch rate of a-C:H films decreases exponentially with increasing the film mass density. The mass of DLCH is 1.6–2.2 g/cm^3, while the mass of photoresists such as poly(methyl methacrylate) (PMMA) is 1.18 g/cm^3. Therefore, the etch rate ratio of DLCH to photoresists is 0.1–0.38 depending on film mass density. (3) Similar component elements to photoresists makes it easy to remove with photoresists together by plasma ashing. (4) A variety of deposition profiles on trench substrates are expected to overcome the resolution limitation of EUV lithography. Figure 1.13 shows the processes of forming patterning by overcoming the resolution limitation of EUV lithography in detail. The most significant one of these processes is to deposit protective coatings on nano-patterned photoresists.

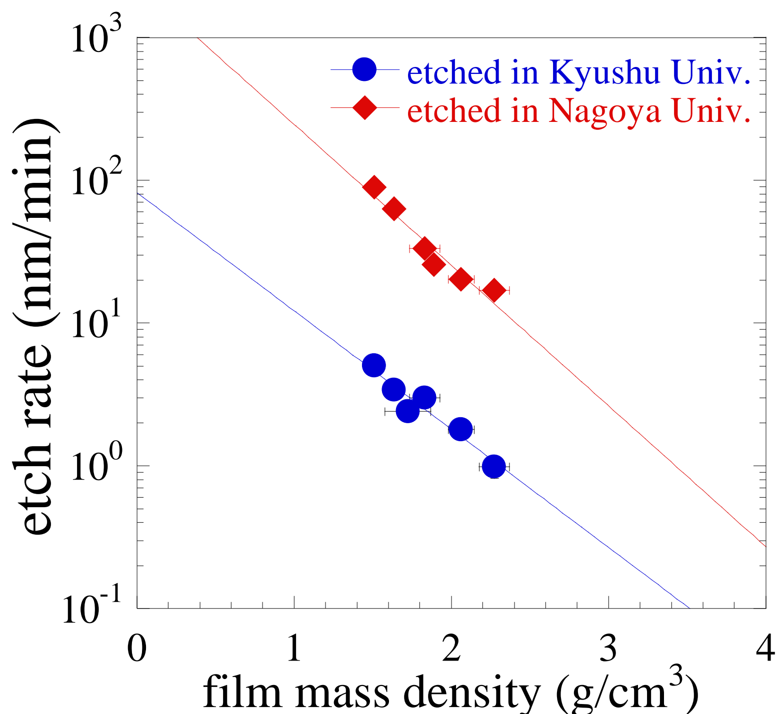

Fig. 1.12. Dependence of etch rate of a-C:H films on mass density using two reactors.

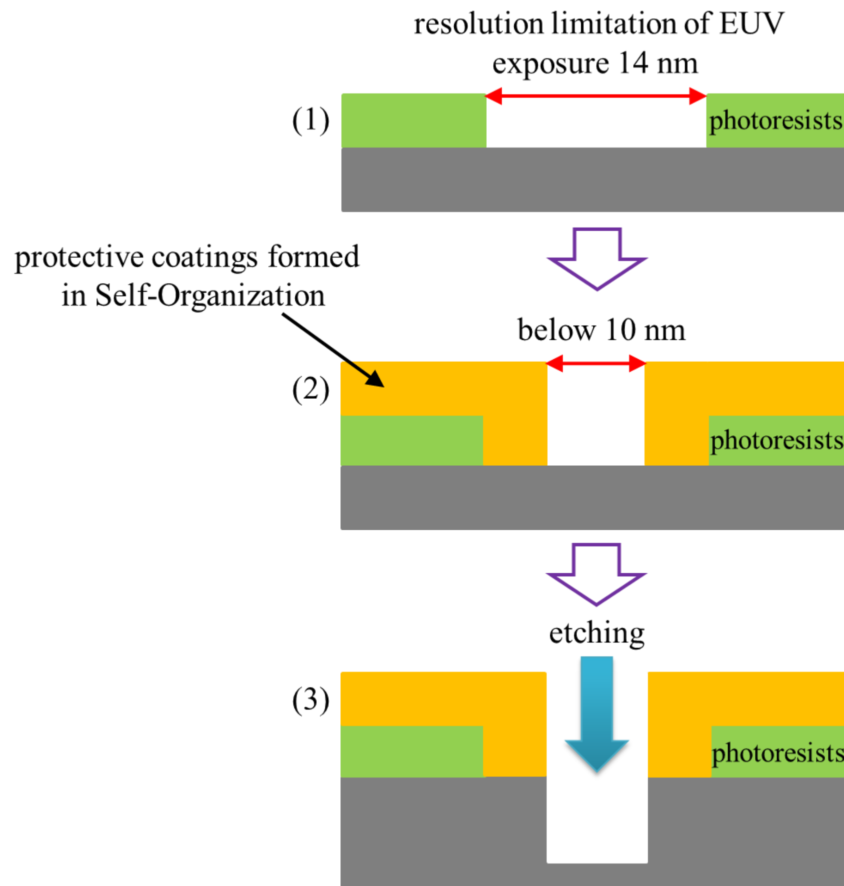

Fig. 1.13. Schematic diagram of forming patterning by overcoming the resolution limitation of lithography with EUV exposure.

1.3.2 Minimal Fabrication

Semiconductor industry has been developed by using miniaturization and large area processes. It is possible to improve performance, acquire high integration and reduce cost based on miniaturization. Similarly, average cost of a chip has been reduced by improving productivity based on large area processes. In contrast, it is needed huge investments in the production apparatuses due to the large area, and the expenses such as fabricating masks (which is necessary to semiconductor industry) are increasing due to the miniaturization.

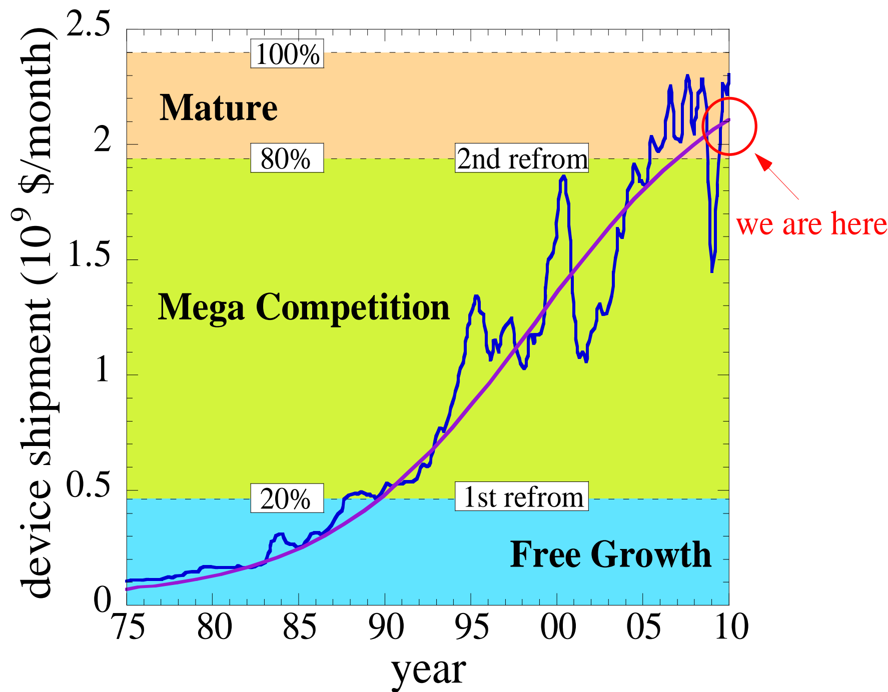

Fig. 1.14. Transition of the world-wide device shipments in semiconductor industry.

Recently the semiconductor device industry is entering the saturation period as shown in Fig. 1.14 [67], which leads to recoup the investments in the production apparatuses difficultly. Therefore, Japan has put forward the minimal fabrication (minimal fab) by using new half-inch wafers according to the development of LSI market. Minimal fabrication is a production system suitable for mature period, which is able to meet the minimum production when necessary. In order to obtain a sufficient productivity in minimal fab, high speed process (one process per minute) is essential. So a variety of technologies of LSI fabrication and the apparatuses corresponding to each process must be devised immediately [68,69].

To minimal fab, there are two basic conditions as follows. (1) One process per minute, is essential to obtain a sufficient productivity. It means that there are a plenty of wafers in assembly line, then the fabrication time of every wafer can be taken as one minute. So the production capacity per month is 43200 chips (1×60 mins×24 hours×30 days, on the premise that a wafer is used to produce a chip).

(2) Wafer of half-inch size, is expected to decrease the processes in fabrication. It shows that using 1/2 inch wafer has quite a few merits, such as also fit large size chips, dicing process for thinning is unnecessary, can exposure under a maskless condition, utility of beam technology will increase, and apparatus is compact (30 cm^2) and movable.

1.3.3 Anisotropic Deposition

Thus far, we have succeeded in controlling deposition profiles of a-C:H films on trench substrates using a H-assisted plasma CVD method, and realized conformal, subconformal, and anisotropic deposition profiles as shown in Fig. 1.15. There are two types of anisotropic deposition profile: in one, carbon is deposited in trenches with only top deposition; in the other, carbon is deposited in trenches without sidewall deposition [70-74]. The anisotropic deposition method can reduce the total number of processes in device fabrication, that is, the iterative processes of resist coating, exposure, etching, and film deposition. Thus, it can be expected that the productivity of chips in minimal fab will increase by anisotropic deposition method.

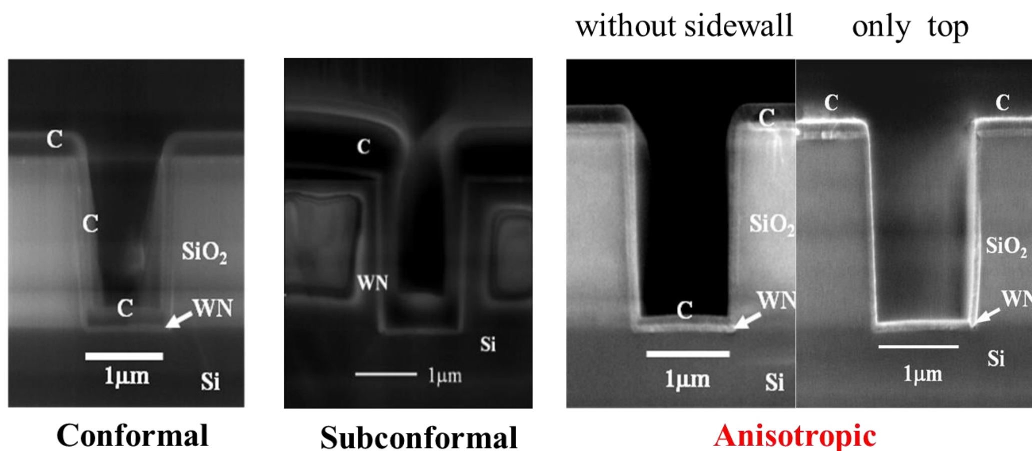

Fig. 1.15. Cross-section SEM images of carbon films deposited on trench substrates.

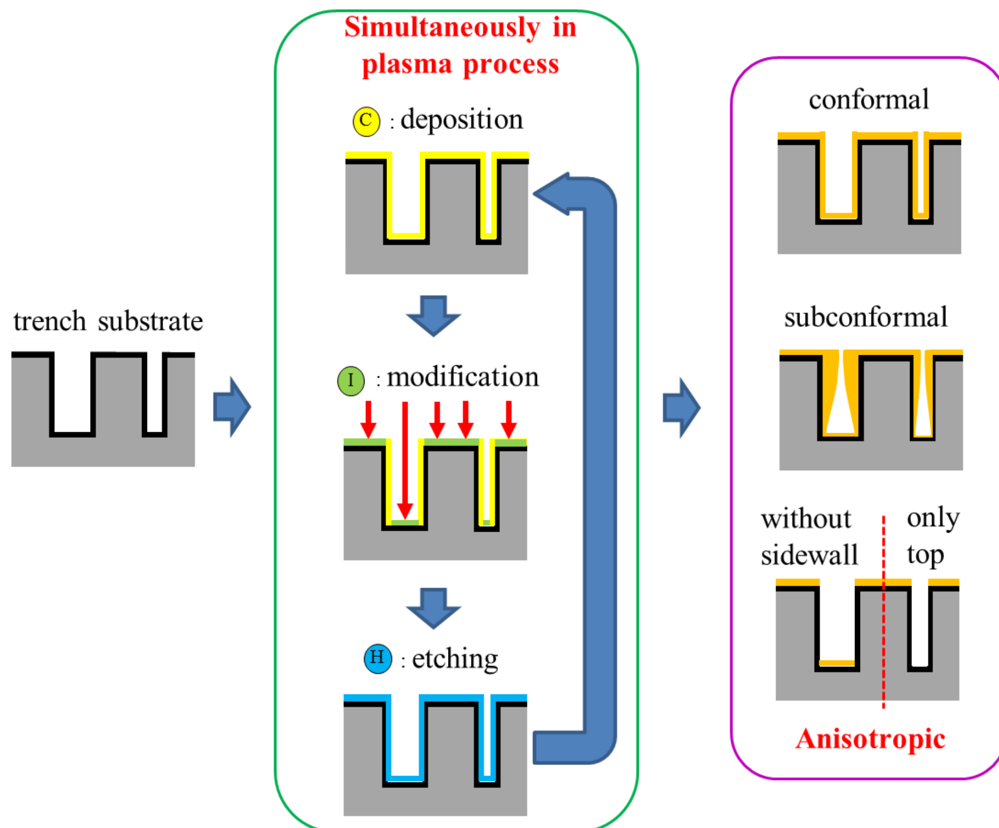

Fig. 1.16. Schematic diagram of anisotropic plasma CVD and a variety of deposition profiles.

For the control of deposition profiles, the key parameters are the flux of carbon-containing neutral radicals, flux of H atoms, flux of ions, and substrate temperature as shown in Fig. 1. 16. Experimental deposition profiles are determined by the balance between deposition rate of carbon-containing neutral radicals and etch rate by H atoms. Bombardment of ions hardens the films and hence decreases the etch rate. When the etch rate surpasses the deposition rate of carbon-containing neutral radicals, no deposition takes place there.

Figure 1.17 shows the principle of anisotropic deposition in details. Irradiation of ions induces structural modification at the film surface, the etch rate for the modified hard films is significantly lower than that for the unmodified films. The incident ion fluxes to the top and bottom of the trench substrate are higher than that to the sidewall, so etch rates at the

top and bottom are lower than that at the sidewall. Moreover, incident fluxes of carbon-containing neutral radicals per surface area at the bottom and sidewall are lower than that at the top. Because of the lower incident fluxes of deposition radicals per surface area and the higher etch rate, the deposition rate at the sidewall is the lowest. Therefore, anisotropic deposition profiles are realized by increasing H atom flux to suppress sidewall deposition.

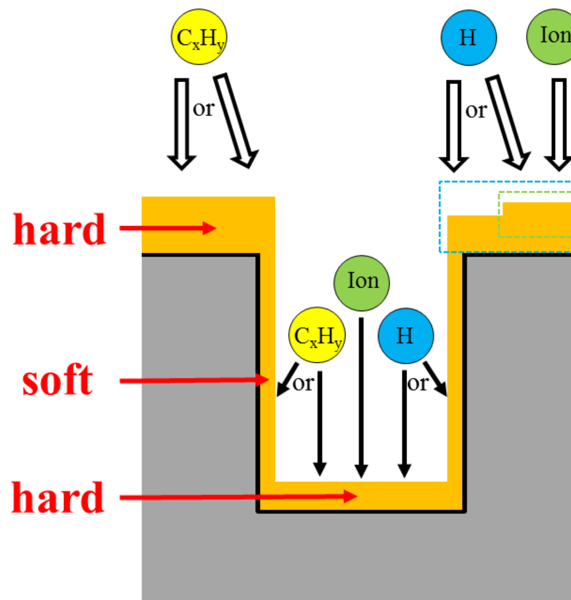

Fig. 1.17. Schematic diagram of incident fluxes of plasma species to trench substrate.

1.3.4 Objectives

In order to meet the demands of fabrication technologies in EUV lithography and minimal fabrication, there are still several issues in our anisotropic deposition method. One of the most important of them is the low deposition rate [75]. Deposition rate of 100 nm/min is required for minimal fabrication in mass production with 1/2 inch size wafers, whereas the maximum deposition rate in our previous study was only few nm/min as shown in Fig. 1.18(a) (Although the film mass density of 2.27 g/cm^3 is obtained at the ion energy of 90 eV in Fig. 1.18(b)). Another important one is the profiles of anisotropic

deposition. The deposition profile, carbon deposited in trenches with top and sidewall deposition, is the one that we urgently want to realize to apply as protective coatings on nano-patterned photoresists. In addition, unlike Si substrate photoresists such as PMMA is weak against both plasma and thermal damages, on which make it rather difficult to deposit a-C:H films.

To solve these issues, we need investigate the deposition mechanism of soft and hard a-C:H films, namely, synergistic effects of the deposition of carbon-containing neutral radicals, etching of H atoms, bombardment of ions, and chemical sputtering due to combined exposure to argon ions and H atoms [76-79]. It is also necessary for us to characterize the deposited a-C:H films to make certain of threshold condition for structural transition from soft PLCH films to hard DLCH films.

Although a variety of materials (methane (CH_4), acetylene (C_2H_2), ethylene (C_2H_4), benzene (C_6H_6), etc.) were introduced as precursor gases in the study of a-C:H film deposition [80-83]. Toluene (C_7H_8), with many merits such as low ionization potential, thermal stability, and low hydrogen to carbon ratio, have been little studied yet.

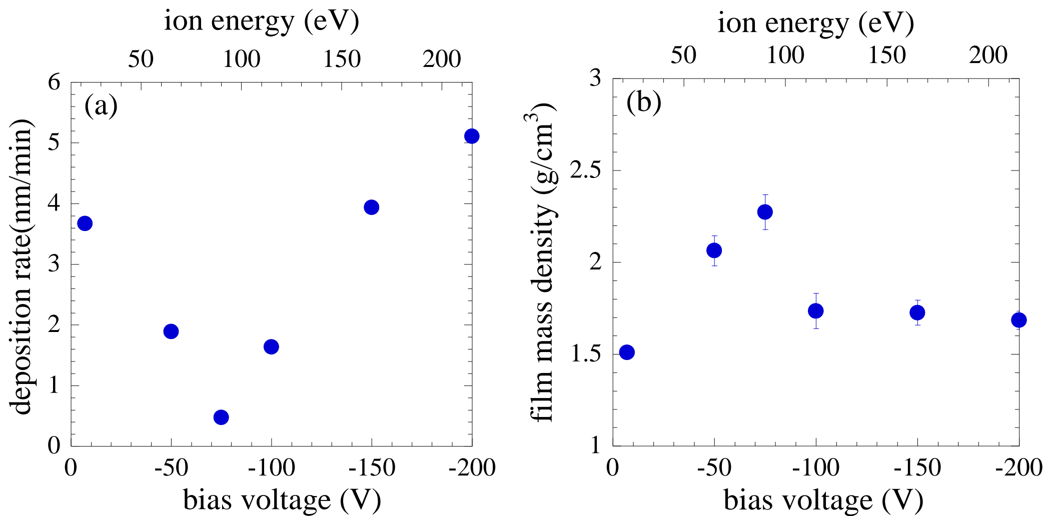

Fig. 1.18. Dependence of (a) deposition rate and (b) film mass density of a-C:H films on bias voltage/ ion energy at the pressure of 0.1 Torr.

1.4 Outline of Thesis

The objectives of this work are included as follows.

(1) Obtainment of the information on plasma parameters during deposition.

(2) Improvement of the deposition rate of a-C:H films to meet mass production.

(3) Investigation of deposition mechanism of soft and hard a-C:H films.

(4) Deposition of a-C:H films on the surface of photoresists.

Following these objectives, chapter 1 gives some fundamental background and introduction relates to this research including properties of a-C:H films. Chapter 2 discusses the experimental setup and experimental methods. In Chapter 3, emission intensities giving information on the generation rates of plasma species and other related parameters are investigated by OES. Chapter 4 describes the effects of pressure, discharge voltage, and gas flow rate ratio on characteristics, especially for deposition rate, of a-C:H films respectively. In chapter 5, it is investigated that the effects of ion bombardment (including ion flux and ion energy) on properties of a-C:H films. Chapter 6 describes the results of depositing a-C:H films on the surface of PMMA. The main results of the thesis are summarized in the conclusions. The future work recommendation is also presented.

References:

[1] P. Gluch and H. Baumann, Build Environ. **39**, 571 (2004).

[2] C. Scheuer, G. A. Keoleian, and P. Reppe, Build Environ. **35**, 1049 (2003).

[3] D. Hunkeler, K. Lichtenvort, and G. Rebitzer, *Environmental Life Cycle Costing* (Taylor, London, 2008).

[4] L. Aye, N. Bamford, B. Charters, and J. Robinson, Constr. Manage. Econ. **18**, 927 (2000).

[5] I. M. Hutchings, Tribology: Friction and Wear of Engineering Materials (Butterworth, Oxford, 1992).

[6] T. Burakowski and T. Wierzchon, *Surface Engineering of Metals: Principles, Equipment, Technologies* (Liliental, Boca Raton, 1998).

[7] J. L. Vossen and W. Kern, *Thin Film Processes II* (Jovanovich, Boston, 1991).

[8] J. E. Mahan, *Physical Vapor Deposition of Thin Films* (Wiley, Vancouver, 2000).

[9] D. Dobkin and M. K. Zuraw, *Principles of Chemical Vapor Deposition* (Kluwer, Netherlands, 2003).

[10] M. Prato, J. Mater. Chem. **7**, 1097 (1997).

[11] S. Iijima, Nature **354**, 56 (1991).

[12] E. Stratakis, R. Giorgi, M. Barberoglou, Th. Dikonimos, E. Salernitano, N. Lisi, and E. Kymakis, Appl. Phys. Lett. **96**, 043110 (2010).

[13] K. Enke, H. Dimigen, and H. Hübsch, Appl. Phys. Lett. **36**, 291 (1980).

[14] S. Stankovich, D. A. Dikin, G. H. B. Dommett, K. M. Kohlhaas, E. J. Zimney, E. A. Stach, R. D. Piner, S. T. Nguyen, and R. S. Ruoff, Nature **442**, 282 (2006).

[15] J. C. Meyer, A. K. Geim, M. I. Katsnelson, K. S. Novoselov, T. J. Booth, and S. Roth, Nature **446**, 60 (2007).

[16] K. S. Novoselov, A. K. Geim, S. V. Morozov, D. Jiang, M. I. Katsnelson, I. V. Grigorieva, S. V. Dubonos, and A. A. Firsov, Nature **438**, 197 (2005).

[17] K. S. Novoselov, A. K. Geim, S. V. Morozov, D. Jiang, Y. Zhang, S. V. Dubonos, I. V. Grigorieva, and A. A. Firsov, Science **306**, 666 (2004).

[18] T. Mori, M. Hiramatsu, K. Yamakawa, K. Takeda, and M. Hori, Diamond Relat. Mater. **17**, 1513 (2008).

[19] K. Holmberg and A. Matthews, *Coatings Tribology: Properties, Mechanisms, Techniques and Applications in Surface Engineering* (Elsevier, Amsterdam, 1994).

[20] N. A. Kaskhedikar and J. Maier, Adv. Mater. **21**, 2664 (2009).

[21] V. C. Tung, L. M. Chen, M. J. Allen, J. K. Wassei, K. Nelson, R. B. Kaner, and Y. Yang, Nano Lett. **9**, 1949 (2009).

[22] J. Robertson, Surf. Coatings Technol. **50**, 185 (1992).

[23] A. A. Voevodin, M. S. Donley, Surf. Coatings Technol. **82**, 199 (1996).

[24] Y. Lifshitz, Diamond Rel. Mater. **8**, 1659 (1999).

[25] X. Dong, R. Torigoe, K. Koga, G. Uchida, N. Itagaki, M. Shiratani, K. Takenaka, Y. Setsuhara, M. Sekine, M. Hori, JPS Conf. Proc. **1**, 015072 (2014).

[26] J. Robertson, Jpn. J. Appl. Phys. **50**, 01AF01 (2011).

[27] A. Zeng, V. F. Neto, J. J. Gracio, Q. H. Fan, Diamond Relat. Mater. **43**, 12 (2014).

[28] R. Kleber, K. Jung, H. Ehrhardt, I. Muhling, K. Breuer, H. Metz, F. Engelke, Thin Solid Films **205**, 274 (1991).

[29] T. Y. Leung, W. F. Man, P. K. Lim, W. C. Chan, F. Gaspari, S. Zukotynski, J. Non-Cryst. Solids **254**, 156 (1999).

[30] K Mallika, R.C. DeVries, R. Komanduri, Thin Solid Films **339**, 19 (1999).

[31] A. Grill, Diamond Relat. Mater. **8**, 428 (1999).

[32] J. Robertson, Mater. Sci. Eng. R **37**, 129 (2002).

[33] W. Jacob and W. Moller, Appl. Phys. Lett. **63**, 1771 (1993).

[34] P. Koidl, C. Wild, B. Dischler, J. Wagner, M. Ramsteiner, Mater. Sci. Forum **52-53**, 41 (1991).

[35] M. A. Tamor, W. C. Vassell, K. R. Carduner, Appl. Phys. Lett. **58**, 592 (1991).

[36] S. F. Yoon, H. Yang, A. Rusli, J. Ahn, Q. Zhang, Diamond Relat. Mater. **7**, 70 (1998).

[37] O. Durand-Drouhin, M. Lejeune, M. Benlahsen, J. Appl. Phys. **91**, 867 (2002).

[38] B. Meyerson and F. Smith, J. Non-Cryst. Solids **35-36**, 435 (1980).

[39] B. Popescu, A. Tagliaferro, F. De Zan, and E. A. Davis, J. Non-Cryst. Solids **266-269**, 803 (2000).

[40] J. E. Field, in *Properties of natural and synthetic Diamond* (Academic Press, London, 1992).

[41] B. T. Kelly, in *Physics of Graphite* (Applied Science, London,1981).

[42] G. M. Pharr, D. L. Callahan, S. D. McAdams, T. Y. Tsui, S. Anders, A. Anders, J. W. Ager, I. G. Brown, C. S. Bhatia, S. R. P. Silva, and J. Robertson, Appl. Phys. Lett. **68**, 779 (1996).

[43] M. Weiler, S. Sattel, K. Jung, H. Ehrhardt, V. S. Veerasamy, and J. Robertson, Appl. Phys. Lett. **64**, 2797 (1994).

[44] J. Robertson, Philos. Trans. R. Soc. A **342**, 277 (1993).

[45] J. Robertson, Diamond Rel. Mater. **3**, 361 (1994).

[46] H. P. Kaukonen and R. M. Nieminen, Phys. Rev. B **61**, 2806 (2000).

[47] N. A. Marks, Phys. Rev. B **56**, 2441 (1997).

[48] K. Kohary, S. Kugler, Phys. Rev. B **63**, 193404 (2001).

[49] C.A. Davis, Thin Solid Films **226**, 30 (1993).

[50] Y. Lifshitz, Diamond Rel. Mater. **5**, 388 (1996).

[51] J. F. Ziegler, J. P. Biersack, and U. Littmark, *The Stopping and Range of Ions in Solids* (Ryssel, Oxford, 1985).

[52] H. Hofsass, H. Feldermann, R. Merk, M. Sebastian, and C. Ronning, Appl. Phys. A **66**, 153 (1998).

[53] W. Jacob, Thin solid Films **326**, 1 (1998).

[54] W. Moller, Appl. Phys. A **56**, 527 (1993).

[55] W. Moller, Jpn. J. Appl. Phys. **34** 2163 (1995).

[56] A. Von Keudell, W. Jacob, J. Appl. Phys. 81 1531 (1997).

[57] C. Hopf, T. Schwarz-Selinger, W. Jacob, and A. von Keudell, J. Appl. Phys. 87, 2719 (2000).

[58] A. Von Keudell, T. Schwarz-Selinger, W. Jacob, J. Appl. Phys. 89, 2979 (2001).

[59] A. Von Keudell, T. Schwarz-Selinger, W. Jacob, J. Vac. Sci. Technol. A 19, 101 (2001).

[60] M. Neisser and S. Wurm, presented at FCMN8, 8th Int. Conf. on Frontiers of Characterization and Metrology for Nanoelectronics, 2013.

[61] J. E. Bjorkholm, Intel Technol. J. **3**, 1 (1998).

[62] T. Miura, presented at 2006 International EUVL Symposium, 2006.

[63] V. Bakshi, *EUV Lithography* (Wiley, Washington, 2008).

[64] M. Neisser, K. Cho, and K. Petrillo, J. Photopolym. Sci. Technol. **25**, 87 (2012).

[65] H. Tanaka, A. Matsumoto, K. Akinaga, A. Takahashi, and T. Okada, Appl. Phys. Lett. **87**, 041503 (2005).

[66] T. Urakawa, R. Torigoe, H. Matsuzaki, D. Yamashita, G. Uchida, K. Koga, M. Shiratani, Y. Setsuhara, K. Takeda, M. Sekine, and M. Hori, Jpn. J. Appl. Phys. **52**, 01AB01 (2013).

[67] http://www.industrie.com/it/mediatheque/6/4/7/000004746.pdf.

[68] K. Yukimura, H. Ogiso, and S. Nakano, Surf. Coatings Technol. **250**, 26 (2014).

[69] G. Comina, A. Suska ,and D. Filippini, Lab Chip **14**, 424 (2014).

[70] J. Umetsu, K. Inoue, T. Nomura, H. Matsuzaki, K. Koga, M. Shiratani, Y. Setsuhara, M. Sekine, and M. Hori, J. Plasma Fusion Res. **8**, 1443 (2009).

[71] T. Nomura, K. Koga, M. Shiratani, Y. Setsuhara, M. Sekine, and M. Hori, MRS Proc. **1222**, 203 (2009).

[72] T. Nomura, T. Urakawa, Y. Korenaga, D. Yamashita, H. Matsuzaki, K. Koga, M.

Shiratani, Y. Setsuhara, M. Sekine, and M. Hori, IEEE TENCON Proc., 2010, p. 2213.

[73] T. Urakawa, T. Nomora, H. Matsuzaki, D. Yamashita, G. Uchida, K. Koga, M. Shiratani, Y. Setsuhara, M. Sekine, and M. Hori, ISPC 20 Proc., 2011, POL02.

[74] K. Koga, T. Urakawa, G. Uchida, K. Kamataki, Y. Seo, N. Itagaki, M. Shiratani, Y. Setsuhara, M. Sekine, and M. Hori, PSE Proc., 2012, p. 136.

[75] T. Urakawa, H. Matsuzaki, D. Yamashita, G. Uchida, K. Koga, M. Shiratani, Y. Setsuhara, M. Sekine, and M. Hori, Surf. Coatings Technol. **228**, S15 (2013).

[76] M. Schlüter, C. Hopf, T. Schwarz-Selinger, and W. Jacob, J. Nucl. Mater. **376**, 33 (2008).

[77] Q. Zhang, S. F. Yoon, A. Rusli, J. Ahn, H. Yang, and D. Bahr, J. Appl. Phys. **84**, 5538 (1998).

[78] N. Mutsukura, S. Inoue, and Y. Machi, J. Appl. Phys. **72**, 43 (1992).

[79] B. B. Wang, K. Ostrikov, Z. L. Tsakadze, and S. Xu, J. Appl. Phys. **106**, 013315 (2009).

[80] X. Jiang, J. W. Zou, K. Reichelt, P. Grunberg, J. Appl. Phys. **66**, 4729 (1989).

[81] G. Adamopoulos, J. Robertson, N. A. Morrison, and C. Godet, J. Appl. Phys. **96**, 6348 (2004).

[82] A. N. Obraztsov, E. A. Obraztsova, A. V. Tyurnina, and A. A. Zolotukhin, Carbon **45**, 2017 (2007).

[83] M. D. Michel, L. V. Muhlen, C. A. Achete, and C. M. Lepienski, Thin Solid Films **496**, 481 (2006).

Chapter 2 Experimental Methods

2.1 a-C:H Film Deposition

Experiments were performed using the H-assisted plasma CVD reactor, in which a capacitively coupled main discharge, an inductively coupled discharge of the H atom source, and a RF discharge of DC self-bias were sustained, as shown in Fig. 2.1 [1-6]. The main discharge, which was sustained between a mesh powered electrode of 85 mm diameter and a plane substrate electrode of 85 mm diameter at a distance of 33 mm, was employed to produce carbon-containing radicals as precursors. The excitation frequency of the main discharge was 28 MHz and the supplied voltage was 150−220 V. The discharge of the H atom source, which was sustained using a radio frequency (RF) induction coil of 100 mm diameter placed 65 mm above the substrate electrode of the main discharge, generated a high flux of H atoms toward the substrate. The excitation frequency of H atom source was 13.56 MHz and the supplied power was 500 W. This reactor provided independent control of the generation rates of carbon-containing radicals and H atoms. The H atom source was separated from the main discharge using a grounded mesh (30 meshes/in.) of 160 mm diameter placed 2−3 mm above the mesh-powered electrode of the main discharge. In addition, RF bias voltage of 400 kHz was applied to the substrate to control the kinetic energy of incident ions and the corresponding substrate bias voltage was from −1.2 (floating) to −80 V.

The precursor gas used in plasma CVD method significantly affects the properties of deposited a-C:H films. The low ionization potential of 8.82 eV of toluene is expected to bring about a high deposition rate, because the deposition rate of a-C:H films tends to increase roughly exponentially with decreasing ionization potential of the precursor gas as shown in Fig. 2.2 [7,8]. The methyl group of toluene is expected to stabilize the a-C:H

films, because the thermal stability of the deposited a-C:H films can be enhanced by the cross-linked structures in films [9]. Moreover, toluene with low hydrogen to carbon ratio is desirable to decrease the H content and improve the hardness of films for mechanical applications.

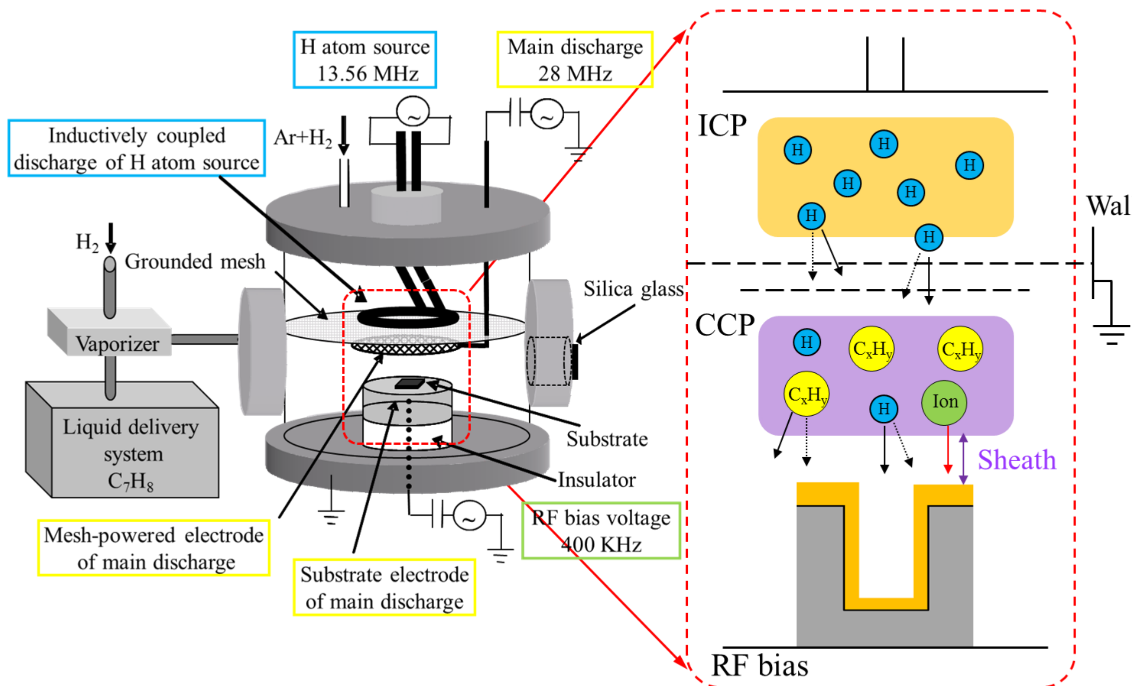

Fig. 2.1. Schematic of H-assisted plasma CVD reactor.

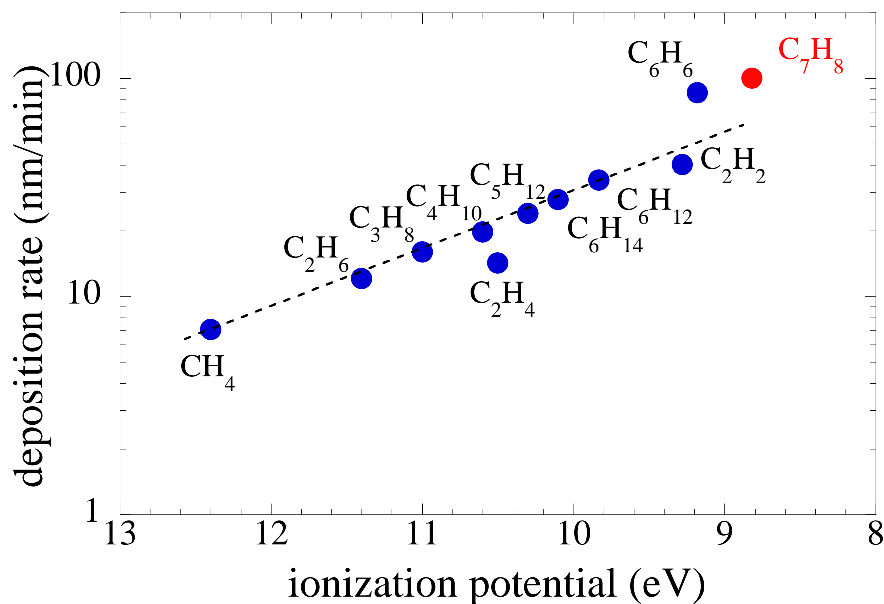

Fig. 2.2. Dependence of deposition rate of a-C:H films by plasma CVD on ionisation potential of the precursor gas [7,8].

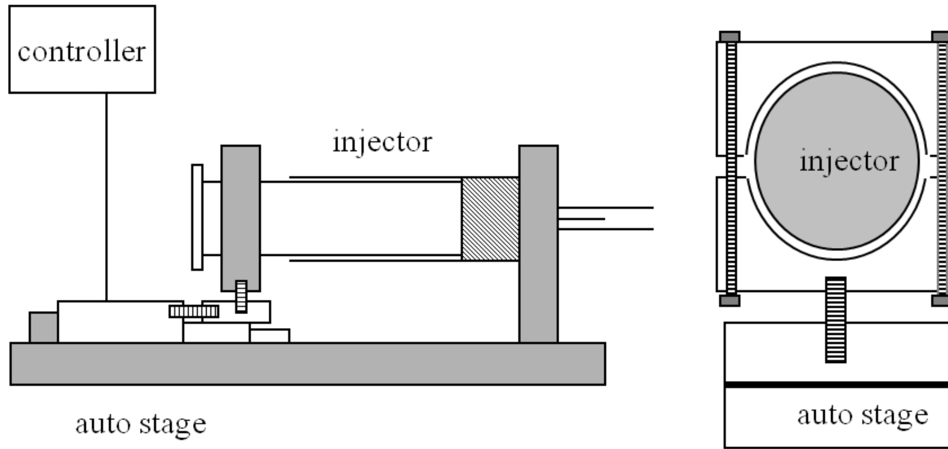

(a) Parts of injector and auto stage

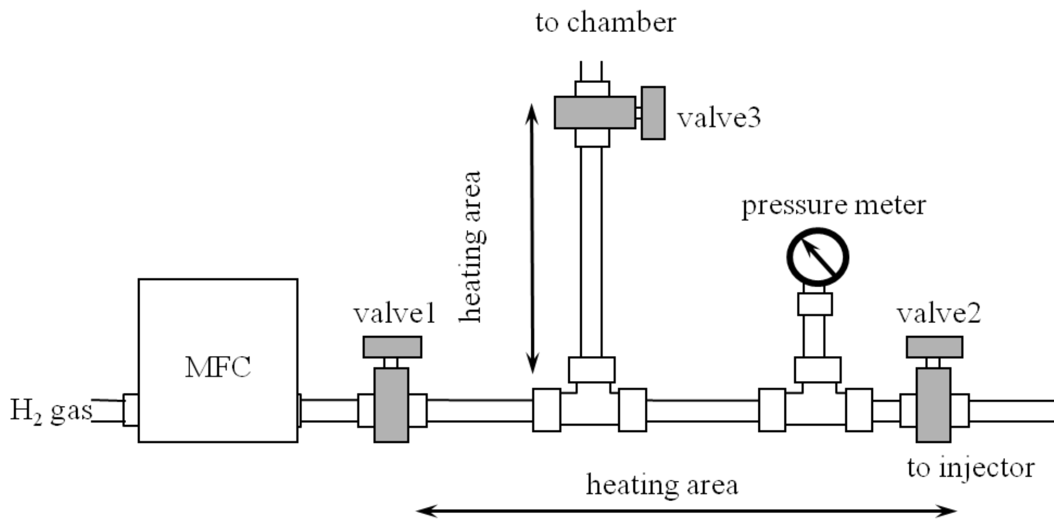

(b) Parts of vaporizer and mass flow controller

Fig. 2.3. Schematic of liquid delivery system.

Figure 2.3 shows the schematic of liquid delivery system. We introduced toluene (C_7H_8) as a precursor material in our H-assisted plasma CVD method instead of common methane. Toluene is liquid at room temperature, so it was filled in an injector supplied to vaporizer at a constant rate by auto stage. Toluene was vaporized at 150℃ and introduced into the reactor with H_2 as a carrier gas. To prevent the vaporized gas from cooling, the temperature of piping and inlet to the chamber were maintained at 220℃ and 90℃,

respectively. The total flow rate of H_2 and Ar was 90 sccm with a gas flow rate ratio $R = [H_2]/([H_2] + [Ar])$. The pressure was set in a range of 0.1–5 Torr. The substrate temperature was 100℃.

To clarify the relation of spatial profiles of plasma to film deposition, a-C:H films were deposited on Si substrates set on a stainless steel stair with four steps (5 mm in height). Contributions of ion bombardment were investigated with stainless steel meshes (aperture ratio of 37.6%) placed 3 mm above each Si substrate in some experiments described in Fig. 2.4. Effects of ion bombardment are eliminated by the meshes, whereas carbon-containing neutral radicals and H atoms can pass though the meshes.

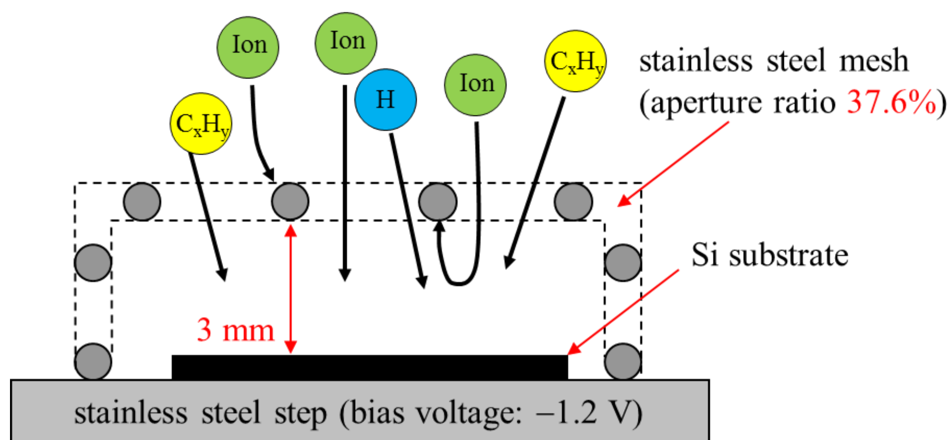

Fig. 2.4. Schematic of elimination of ion bombardment to Si substrate during deposition.

2.2 Plasma and Film Characterization

2.2.1 Optical Emission Spectroscopy

Optical emission spectroscopy (OES) as a fundamental and noninvasive method is increasingly used for plasma diagnostic analysis. Owing to the different electronic structure of each element, a certain photon emitted by that element has a unique wavelength [10]. By recording and analyzing the wavelengths of photons emitted during

the de-excitation of plasma species in OES, we can obtain the information of elemental composition of plasma [11]. Moreover, we can also derive the plasma parameters such as effective electron temperature T_e and electron density n_e.

As shown in Eqs. (2.1) – (2.4), Ar 425.9 nm and 750.4 nm emission intensities have little effect on quenching and radiation trapping, and their upper levels of $3p_1$ (excitation energy of 14.7 eV) and $2p_1$ (excitation energy of 13.5 eV) have small cross sections for electron impact excitation from metastable states [12,13].

$$\mathrm{Ar} + \mathrm{e} \rightarrow \mathrm{Ar}\big(5\mathrm{p}'[1/2]_0 \text{ or } 3\mathrm{p}_1\big) + \mathrm{e} \qquad \big(\varepsilon \geq 14.74\ \mathrm{eV}\big) \tag{2.1}$$

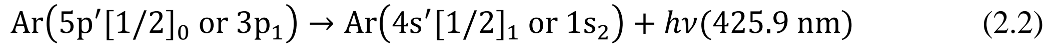

$$\mathrm{Ar}\big(5\mathrm{p}'[1/2]_0 \text{ or } 3\mathrm{p}_1\big) \rightarrow \mathrm{Ar}\big(4\mathrm{s}'[1/2]_1 \text{ or } 1\mathrm{s}_2\big) + h\nu(425.9\ \mathrm{nm}) \tag{2.2}$$

$$\mathrm{Ar} + \mathrm{e} \rightarrow \mathrm{Ar}\big(4\mathrm{p}'[1/2]_0 \text{ or } 2\mathrm{p}_1\big) + \mathrm{e} \qquad \big(\varepsilon \geq 13.48\ \mathrm{eV}\big) \tag{2.3}$$

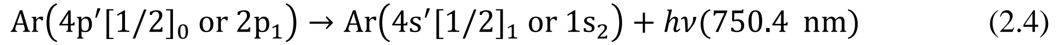

$$\mathrm{Ar}\big(4\mathrm{p}'[1/2]_0 \text{ or } 2\mathrm{p}_1\big) \rightarrow \mathrm{Ar}\big(4\mathrm{s}'[1/2]_1 \text{ or } 1\mathrm{s}_2\big) + h\nu(750.4\ \mathrm{nm}) \tag{2.4}$$

Thus, the emission intensity ratio Ar $I_{425.9}$/Ar $I_{750.4}$ gives information on the effective electron temperature T_e by

$$\frac{I_{425.9}}{I_{750.4}} = C\frac{k_{425.9}n_{Ar}n_{e,h}}{k_{750.4}n_{Ar}n_{e,h}} = C\frac{k_{425.9}}{k_{750.4}} = f(T_e) \tag{2.5}$$

where k is the rate coefficient for excitation from the ground state, n_Ar is the ground state Ar atom density, $n_\mathrm{e,h}$ is the high-energy electron ($\varepsilon \geq 13$ eV) density, C is the proportionality factor of the spectrometer spectral sensitivity for the line wavelengths.

According to Eqs. (2.6) – (2.10), there are two major mechanisms of electron excitation of atomic Ar emission at 811.5 nm under our experimental conditions (low-temperature and low-pressure plasmas) [14,15]. Ar 811.5 nm emission intensity is strongly affected by the $1s_5$ metastable state (excitation energy of 11.5 eV) that can provide an additional channel for Ar atom excitation by low-energy electrons ($1.5 \leq \varepsilon \leq 3$ eV).

(a) direct excitation from ground state

$$\mathrm{Ar} + \mathrm{e} \rightarrow \mathrm{Ar}\big(4\mathrm{p}[5/2]_3 \text{ or } 2\mathrm{p}_9\big) + \mathrm{e} \qquad (\varepsilon \geq 13.08\ \mathrm{eV}) \tag{2.6}$$

$$\mathrm{Ar}\big(4\mathrm{p}[5/2]_3 \text{ or } 2\mathrm{p}_9\big) \rightarrow \mathrm{Ar}^{\mathrm{m}}\big(4\mathrm{s}[3/2]_2 \text{ or } 1\mathrm{s}_5\big) + h\nu(811.5\ \mathrm{nm}) \tag{2.7}$$

(b) two-step excitation via metastable state

$$\mathrm{Ar} + \mathrm{e} \rightarrow \mathrm{Ar}^{\mathrm{m}}\big(4\mathrm{s}[3/2]_2 \text{ or } 1\mathrm{s}_5\big) + \mathrm{e} \quad (\varepsilon \geq 11.55\ \mathrm{eV}) \tag{2.8}$$

$$\mathrm{Ar}^{\mathrm{m}} + \mathrm{e} \rightarrow \mathrm{Ar}\big(4\mathrm{p}[5/2]_3 \text{ or } 2\mathrm{p}_9\big) + \mathrm{e} \quad (\varepsilon \geq 1.53\ \mathrm{eV}) \tag{2.9}$$

$$\mathrm{Ar}\big(4\mathrm{p}[5/2]_3 \text{ or } 2\mathrm{p}_9\big) \rightarrow \mathrm{Ar}^{\mathrm{m}}\big(4\mathrm{s}[3/2]_2 \text{ or } 1\mathrm{s}_5\big) + h\nu(811.5\ \mathrm{nm}) \tag{2.10}$$

Thus, the emission intensity ratio Ar $I_{811.5}$/Ar $I_{750.4}$ gives information on Ar 1s$_5$ metastable density n_{Ar}^{m} and/or low-energy electron density $n_{\mathrm{e,l}}$ by

$$\frac{I_{811.5}}{I_{750.4}} = C\left(\frac{k_{811.5} n_{\mathrm{Ar}} n_{e,h} + k_{811.5}^{\mathrm{m}} n_{\mathrm{Ar}}^{\mathrm{m}} n_{\mathrm{e,l}}}{k_{750.4} n_{\mathrm{Ar}} n_{\mathrm{e,h}}}\right) = C\left(\frac{k_{811.5}}{k_{750.4}} + \frac{k_{811.5}^{\mathrm{m}} n_{\mathrm{Ar}}^{\mathrm{m}} n_{\mathrm{e,l}}}{k_{750.4} n_{\mathrm{Ar}} n_{\mathrm{e,h}}}\right) \tag{2.11}$$

where k^{m} is the rate coefficient for excitation from 1s$_5$ metastable state, n_{Ar}^{m} is the 1s$_5$ metastable state Ar atom density. Figure 2.5 shows the energy levels of Ar atom involved in transitions of Eqs. (2.1) – (2.4) and Eqs. (2.6) – (2.10).

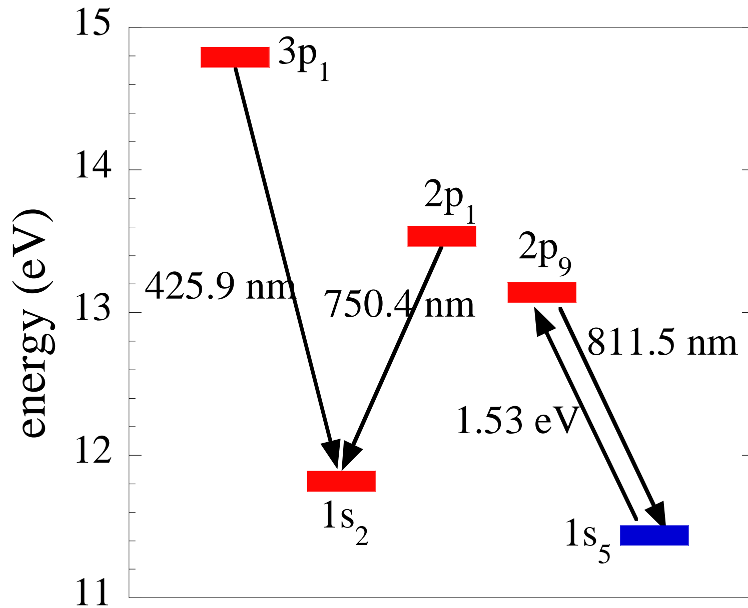

Fig. 2.5. Energy levels of Ar atom involved in transitions observed at 425.9, 750.4, and 811.5 nm.

Moreover, owing to the low $n_{\mathrm{e,l}}$ in E-mode plasma (when the capacitive coupling dominates), $n_{\mathrm{Ar}}^{m}/n_{\mathrm{Ar}}$ is evaluated by [16]

$$\frac{n_{\mathrm{Ar}}^{m}}{n_{\mathrm{Ar}}} \approx \frac{k_{\mathrm{m}} n_{\mathrm{e,h}}}{k_{\mathrm{dif}}} \tag{2.12}$$

where k_{m} is the rate coefficient of $1\mathrm{s}_5$ metastable state for excitation from ground state, k_{dif} is the rate coefficient for diffusive wall loss. The Eq. (2.11) is simplified by substituting Eq. (2.12)

$$\frac{I_{811.5}}{I_{750.4}} = C\left(\frac{k_{811.5}}{k_{750.4}} + \frac{k_{811.5}^{\mathrm{m}} k_{\mathrm{m}} n_{\mathrm{e,l}}}{k_{750.4} \mathrm{k}_{\mathrm{dif}}}\right) = f\left(T_e, n_{\mathrm{e,l}}\right) \tag{2.13}$$

i.e., Ar $I_{811.5}$/Ar $I_{750.4}$ depends on effective electron temperature and low-energy electron density in E-mode plasma.

In H-mode plasma (when the inductive coupling dominates), $n_{\mathrm{e,l}}$ is at least two orders of magnitude higher than in the E-mode, $n_{\mathrm{Ar}}^{m}/n_{\mathrm{Ar}}$ is evaluated by

$$\frac{n_{\mathrm{Ar}}^{m}}{n_{\mathrm{Ar}}} \approx \frac{k_{m} n_{\mathrm{e,h}}}{k_{\mathrm{glo}} n_{\mathrm{e,l}}} \tag{2.14}$$

where k_{glo} is the global rate coefficient of all the processes (excitation, quenching, superelastic collision, ionization, etc) involving electrons. The Eq. (2.11) is simplified by substituting Eq. (2.14)

$$\frac{I_{811.5}}{I_{750.4}} = C\left(\frac{k_{811.5}}{k_{750.4}} + \frac{k_{811.5}^{m} k_{m}}{k_{750.4} k_{\mathrm{glo}}}\right) = f(T_{\mathrm{e}}) \tag{2.15}$$

i.e., Ar $I_{811.5}$/Ar $I_{750.4}$ depends on effective electron temperature in H-mode plasma.

In this work optical spectrometer (Ocean Optics USB2000+) connected to a collimating lens/thin steel pipe (inner diameter of 1 mm) by an optical fiber is used to measure the emission spectra of plasma through a silica glass window of the H-assisted plasma CVD reactor. The collimating lens is used to obtain information of plasma parameters in the bulk region, and the thin steel pipe is used to investigate the spatial profiles of plasma.

2.2.2 Scanning Electron Microscopy

The scanning electron microscope (SEM) is widely used in a number of industries and laboratories for the determination of film thickness, particle size and shape, elemental distribution in a sample, etc. The schematic of an SEM is shown in Fig. 2.6. Electrons, produced at the source by thermionic heating, are accelerated to an energy ranging from 0.2 to 40 keV and condensed by two condenser lenses into a narrow beam which hits the surface of sample [17].

After the beam is focused, scanning coils situated above the objective lens are used to deflect the beam in the X and Y axes, so that they allow the beam to be scanned over a rectangular area of the sample surface. This beam scanning controls the position of electron beam to collect information on a certain area of sample.

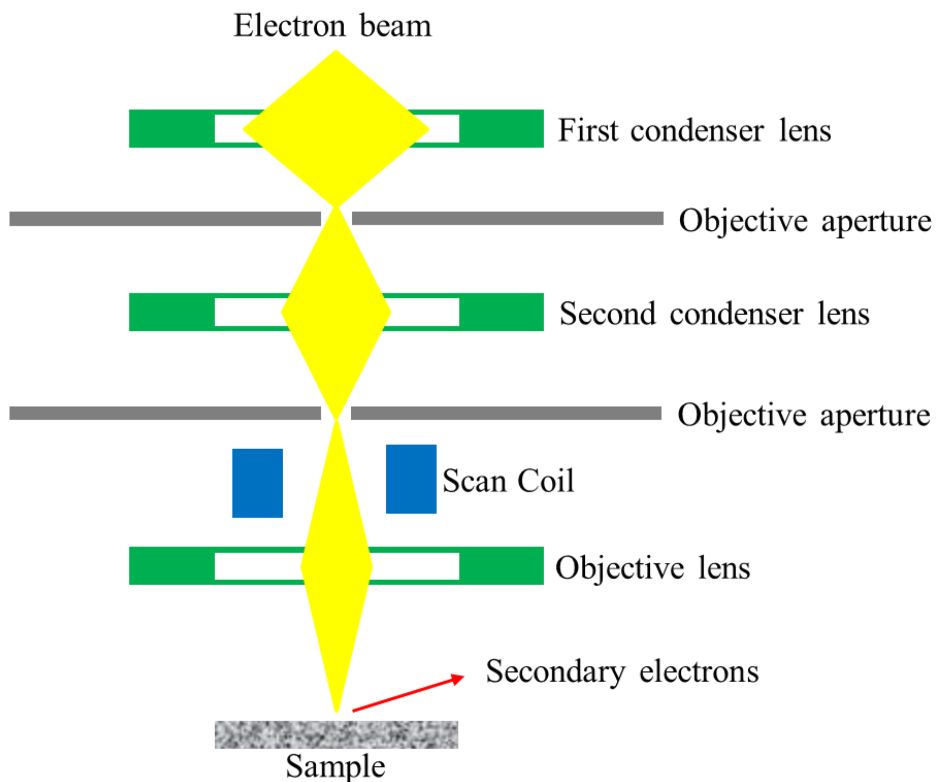

Fig. 2.6. Schematic of a scanning electron microscope.

The most common mode used in SEM is detection of secondary electrons produced by electron-sample interaction [18]. The number of secondary electrons depends on the angle at which beam meets surface of sample. Then an image containing the information of the structure and surface topography is created by scanning the sample and collecting the secondary electrons with a detector. In present work JEOL JIB-4600F SEM was used to take the cross-section images of the deposited films and to measure their thickness.

2.2.3 Fourier Transform Infrared Spectroscopy

Fourier transform infrared spectroscopy (FTIR) is an analytical technique used to characterize hydrogen bonding configuration in a-C:H films. Absorbed infrared radiation usually excites molecules to a higher vibrational state when a sample is irradiated. The wavelength of infrared radiation absorbed by a certain molecule and the absorption intensity are different depending on structure of the sample. Thus, this technique measures the absorption of infrared radiation to identify molecular components and structures. In addition, the absorption spectra can be obtained using the Beer-Lambert law

$$\alpha(\tilde{\nu}) = -\frac{1}{d}\ln\left(\frac{I}{I_0}\right) \tag{2.16}$$

where $\alpha(\tilde{\nu})$ is the absorption coefficient, d is the film thickness, and I_0 and I are the intensities of the incident light and transmitted light, respectively. The absorption spectra are usually presented with wavenumber, which is the reciprocal of the wavelength.

Generally, the C–H vibrational modes of FTIR spectra obtained from a-C:H films are classified into bending and stretching modes [19]. The bending modes are found between 1300 and 1700 cm^{-1} and the stretching modes are found between 2850 and 3300 cm^{-1} [20,21]. In this work, the bending modes were superimposed with a broad phonon band induced by carbon skeleton between 500 and 1800 cm^{-1} [22]. Thus, only the stretching modes found between 2850 and 3300 cm^{-1} are used to quantify the hydrogen content in

a-C:H films owing to a more accurate curve fitting. Table II gives the accepted assignments of vibrational frequencies in a-C:H films, including the corrections [23-25].

To obtain information on hydrogen content and hydrogen bonding configurations in films, infrared absorption spectra of a-C:H films were measured with a JASCO FT-IR/620 spectrometer in this work.

Table II. Assignments of frequency of C−H stretching vibrations in a-C:H films [23-25].

Configuration	Structure	Vibration frequency (cm^{-1})
sp^2CH_2	olefinic	3085±15
sp^2CH	aromatic	3060±40
sp^2CH	olefinic	3010±20
sp^3CH_3	asymmetric	2960±15
sp^3CH_2	asymmetric	2925±15
sp^3CH_3	symmetric	2875±10
sp^3CH_2	symmetric	2855±10

2.2.4 Elastic Recoil Detection Analysis

Elastic recoil detection analysis (ERDA) is an ion beam analysis technique in materials science to obtain information of light elements in thin films [26]. Spectrometry of the forward recoiled atoms provides quantitative depth profiles of the sample. In ERDA the energy of incident ion beam has a wide range from 2 to 200 MeV, which depends on the sample to be analyzed [27]. With the help of a surface barrier detector, the energy of recoiled atoms is recorded.

ERDA is also called hydrogen forward scattering spectrometry (HFS) in the case of measurement of the composition and distribution of hydrogen content in thin films [28]. He^{2+} ion beam was projected to the sample surface at a glancing angle, kicking the hydrogen atoms out of the sample in the forward direction as shown in Fig. 2.7. A tandem

Pelletron accelerator (NEC 3SDH) was used in this work to probe H content in deposited films.

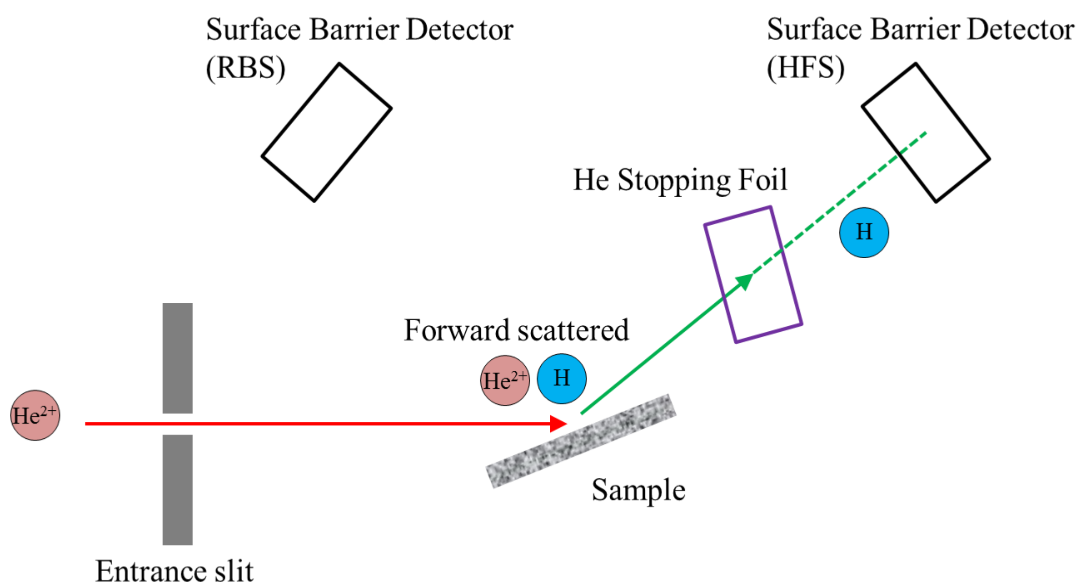

Fig. 2.7. Schematic of a conventional ERD setup.

2.2.5 Raman Spectroscopy

Raman spectroscopy, a molecular spectroscopy which is observed as inelastically scattered light, is widely used to characterize the structural quality of a-C:H films as powerful and nondestructive method [29,30]. The simplest form of Raman spectroscopy can be thought of as a process where a photon of light interacts with a sample to produce scattered radiation of different wavelengths.

The scattering process without a change of frequency is referred to as Rayleigh scattering, and a change in the frequency of the light is referred to as Raman scattering. From the Jablonski diagram shown in Fig. 2.8, we can see that Raman shifted photon is either of lower or higher energy that incident photon of light. The photon scattered at a lower energy is called Stokes scattering, the photon scattered at a higher energy is called Anti-Stokes scattering [31]. Owing to most molecules will be found in the ground state at room temperature, therefore, most Raman measurements are performed

considering only the Stokes scattering.

Raman shift $\Delta\nu$ is typically expressed in wavenumber by

$$\Delta\nu = \left(\frac{1}{\lambda_0} - \frac{1}{\lambda_1}\right) \tag{2.17}$$

where λ_0 is the wavelength of incident photon, λ_1 is the wavelength of Raman scattered photon. In present work, Raman spectra were measured at room temperature with a laser Raman spectrometer (JASCO NRS-3100) using 532 nm excitation from a green laser.

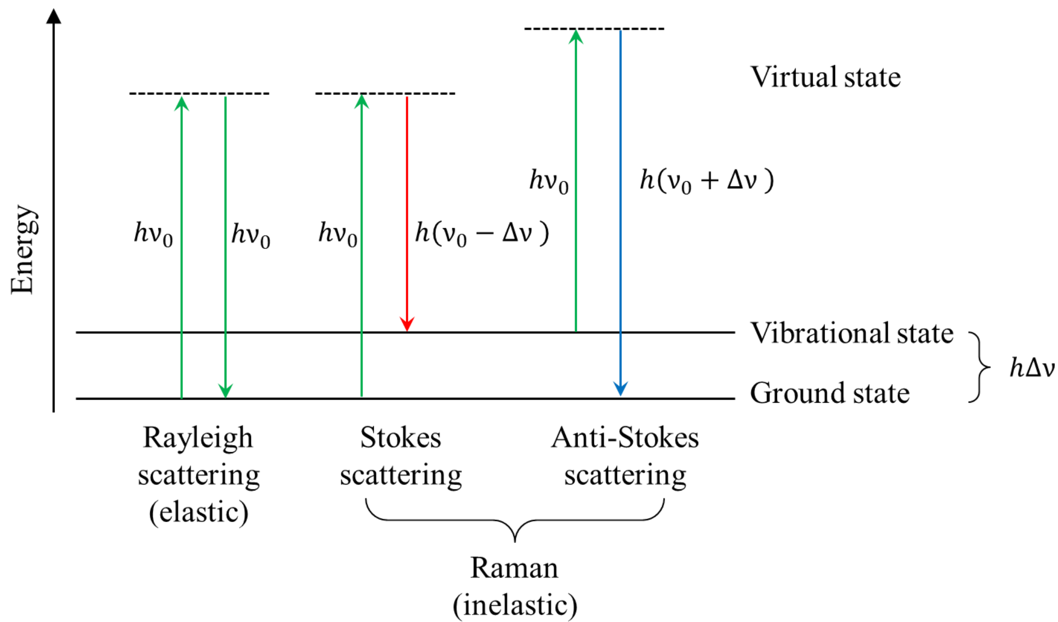

Fig. 2.8. Jablonski energy diagram for Raman scattering.

2.2.6 X-ray Photoelectron Spectroscopy

X-ray photoelectron spectroscopy (XPS), also known as electron spectroscopy for chemical analysis (ESCA), is the most widely used technique to investigate the chemical composition of surfaces. XPS spectra are obtained by irradiating a material surface while simultaneously counting photoelectrons ejected from a particular characteristic energy as shown in Fig. 2.9 [32]. The energies and intensities of the photoelectron peaks enable identification and quantification of all elements except hydrogen. The depth of 1–10 nm from the top surface is analyzed for an XPS measurement.

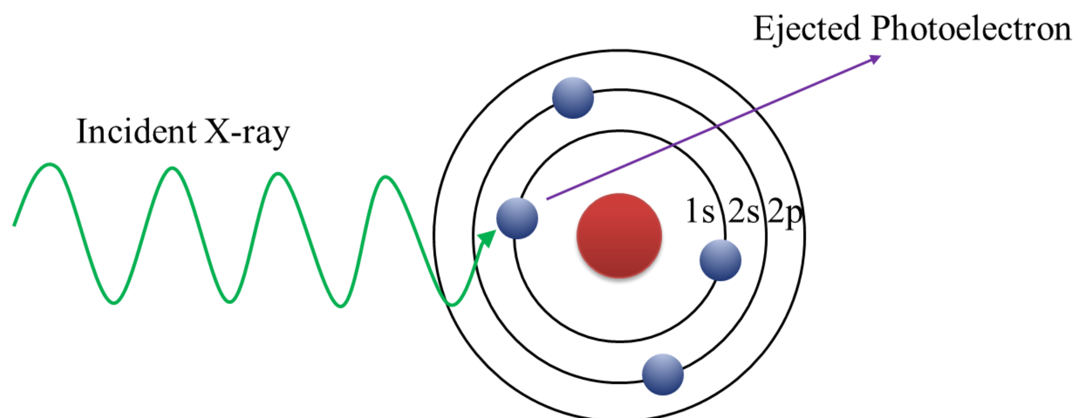

Fig. 2.9. Ejection of photoelectron with an X-ray beam.

The binding energy (BE) of each of the ejected photoelectron can be determined based on the work of Ernest Rutherford by [33]

$$\mathrm{BE} = h\nu - \mathrm{KE} - \Phi_{\mathrm{spec}} \tag{2.18}$$

where $h\nu$ is the energy of incident X-ray, KE is the electron kinetic energy, Φ_{spec} is the spectrometer work function. To obtain information of C 1s peaks in this work, XPS measurements were carried out with a Shimadzu AXIS-165x spectrometer using monochromatized Al Kα (1486.6 eV) X-ray radiation.

2.3 Ion Energy and Plasma Potential

The properties of a-C:H films deposited by plasma CVD are strongly depended on bias voltage and hence on ion energy, indicating ions play a critical role in a-C:H film deposition. The ion energy is derived from the potential difference between the plasma potential and the bias voltage by which ions are accelerated [34,35]. At a higher pressure such as 5 Torr, This ion energy corresponds to the maximum ion energy and it is employed as a measure of the ion energy distribution in this study, although ions can be decelerated by collisions in the sheath in front of the substrates, namely, most ions have lower ion energies than the maximum ion energy.

Since at all instants the plasma must remain neutral, the instantaneous current through

the plane of origin at the anode is equal to that through the plane of origin at the cathode [36]. The plasma potential is defined as anode sheath potential in this work, it is obtained from calculating the net instantaneous currents of ions and electrons through the planes of origin at the cathode and anode. Thus, the average value of plasma potential over one RF cycle $\langle V_{\mathrm{p}} \rangle$ is given approximately by [37,38]

$$\langle V_{\mathrm{p}} \rangle = \frac{1}{T}\int_{t_1}^{t_2} V(t)\,\mathrm{d}t + V_{\mathrm{p}}^{0} \tag{2.19}$$

where T is the period which equals $2\pi/\omega$, $V(t)$ is applied RF voltage with the waveform depicted in Fig 2.10, so it is written by

$$V(t) = V_{\mathrm{RF}} \sin \omega t - V_{\mathrm{DC}} \tag{2.20}$$

where V_{RF} is the half peak-to-peak RF voltage, V_{DC} is the DC self-bias of main discharge, t_1 and t_2 are determined by

$$\omega t_1 = \sin^{-1}(V_{\mathrm{DC}}/V_{\mathrm{RF}}) \tag{2.21}$$

and

$$\omega t_2 = \pi - \omega t_1 \tag{2.22}$$

At last, V_{p}^{0} is the potential of the plasma relative to a floating object and hence given by [39]

$$V_{\mathrm{p}}^{0} = (kT_{\mathrm{e}}/2\mathrm{e}) \ln m_{\mathrm{i}}/2.3m_{\mathrm{e}} \tag{2.23}$$

where m_{i} is the mass of the ions concerned [40].

The values of V_{RF}, V_{DC}, and $\langle V_{\mathrm{p}} \rangle$ at the different pressure are listed in Table III. The V_{DC} decreases with increasing the pressure from 0.1 to 5 Torr. Thus, the $\langle V_{\mathrm{P}} \rangle$ increases from 15.0 to 34.0 V with increasing the pressure.

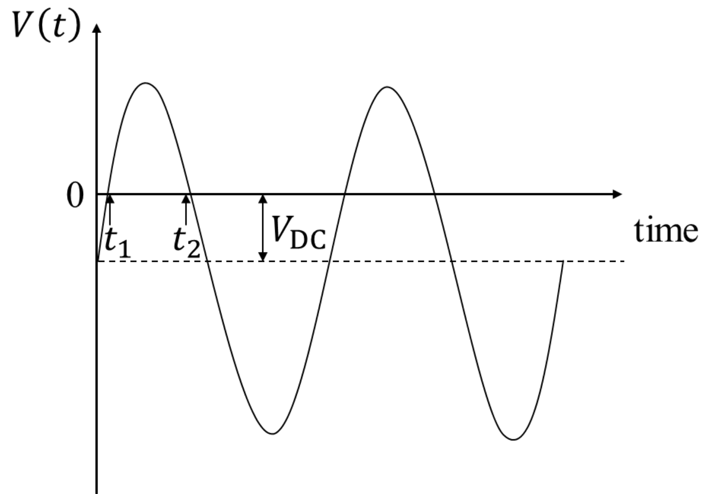

Fig. 2.10. The RF voltage waveform on the powered electrode.

Table III. Values of V_{RF}, V_{DC}, and $\langle V_p \rangle$ in a range of 0.1–5 Torr.

Pressure (Torr)	V_{RF} (V)	V_{DC} (V)	$\langle V_p \rangle$ (V)
0.1	75	-50.3	15.0
0.5	75	-35.4	19.6
1	75	-22.3	24.5
2	75	-11.5	29.1
5	75	-1.2	34.0

References:

[1] M. Shiratani, H. J. Jin, K. Takenaka, K. Koga, T. Kinoshita, and Y. Watanabe, Sci. Technol. Adv. Mater. **2**, 505 (2001).

[2] K. Takenaka, M. Kita, T. Kinoshita, K. Koga, M. Shiratani, and Y. Watanabe, J. Vac. Sci. Technol. A **22**, 1903 (2004).

[3] K. Takenaka, M. Shiratani, M. Takashita, M. Kita, K. Koga, and Y. Watanabe, Pure Appl. Chem. **77**, 391 (2005).

[4] K. Takenaka, K. Koga, M. Shiratani, Y. Watanabe, and T. Shingen, Thin Solid Films **506–507**, 197 (2006).

[5] J. Umetsu, K. Koga, K. Inoue, H. Matsuzaki, K. Takenaka, and M. Shiratani, Surf. Coatings Technol. **202**, 5659 (2008).

[6] J. Umetsu, K. Inoue, T. Nomura, H. Matsuzaki, K. Koga, M. Shiratani, Y. Setsuhara, M. Sekine, and M. Hori, Proc. 30th Dry Process Symp., 2008, p. 35.

[7] P. Koidl, C. Wild, B. Dischler, J. Wagner, and M. Ramsteiner, Mater. Sci. Forum **52–53**, 41 (1991).

[8] J. W. Zou, K. Schmidt, K. Reichelt, and B. Dischler, J. Appl. Phys. **67**, 487 (1990).

[9] J. Joo, Y. C. Quan, and D. Jung, J. Mater. Res. **15**, 228 (2000).

[10] M. V. Malyshev and V. M. Donnelly, J. Vac. Sci. Technol. A **15**, 550 (1997).

[11] J. B. Boffard, C. C. Lin, and C. A. DeJoseph Jr, J. Phys. D **37**, R143 (2004).

[12] S. A. Moshkalyov, J. A. Diniz, J. W. Swart, P. J. Tatsch, and M. Machida, J. Vac. Sci. Technol. B **15**, 2682 (1997).

[13] A. M. Daltrini, S. A. Moshkalev, M. J. R. Monteiro, E. Besseler, A. Kostryukov, and M. Machida, J. Appl. Phys. **101**, 073309 (2007).

[14] W. Williams, Z.-T. Lu, K. Rudinger, C.-Y. Xu, R. Yokochi, and P. Mueller, Phys. Rev. A **83**, 012512 (2011).

[15] S. A. Moshkalyov, P. G. Steen, S. Gomez, and W. G. Graham, Appl. Phys. Lett. **75**,

328 (1999).

[16] T. Czerwiec and D. B. Graves, J. Phys. D **37**, 2827 (2004).

[17] R. F. Willis, B. Fitton, and G. S. Painter, Phys. Rev. B **9**, 1926 (1974).

[18] H. Seiler, J. Appl. Phys. **54**, R1 (1983).

[19] W. Dworschak, R. Kleber, A. Fuchs, B. Scheppat, G. Keller, K. Jung, and H. Ehrhardt, Thin Solid Films **189**, 257 (1990).

[20] T. Heitz, B. Drévillon, C. Godet, and J. E. Bourée, Phys. Rev. B **58**, 13957 (1998).

[21] P. B. Nagabalasubramanian, S. Periandy, S. Mohan, and M. Govindarajan, Spectrochim. Acta, Part A **73**, 277 (2009).

[22] R. Stief, J. Schäfer, J. Ristein, L. Ley, and W. Beyer, J. Non-Cryst. Solids **198-200**, 636 (1996).

[23] C. Thomsen and S. Reich, Phys. Rev. Lett. **85**, 5214 (2000).

[24] B. Dishler, EMRS Symp. Rroc. **17**, 1987, p. 189.

[25] L. J. Bellamy, *Advances in Infrared Group Frequencies* (Methuen, London, 1968).

[26] W. Assmann, H. Huber, Ch. Steinhausen, M. Dobler, H. Glückler, and A. Weidinger, Nucl. Instrum. Methods Phys. Res., Sect. B **89**, 131 (1994).

[27] W. M. Arnold Bik and F. H. P. M. Habraken, Rep. Prog. Phys. **56**, 859 (1993).

[28] J. W. Martin, *The Local Chemical Analysis of Materials* (R.W. CAHN, UK, 2003).

[29] D. S. Knight and W. B. White, J. Mater. Res. **4**, 385 (1989).

[30] R. J. Nemanich and S. A. Solin, Phys. Rev. B **20**, 392 (1979).

[31] A. Jabloński, nature **131**, 839 (1933).

[32] K. Siegbahn and K. Edvarson, Nucl. Phys. **1**, 137 (1956).

[33] E. Rutherford, Philos. Mag. **27**, 488 (1914).

[34] T. Urakawa, H. Matsuzaki, D. Yamashita, G. Uchida, K. Koga, M. Shiratani, Y. Setsuhara, M. Sekine, and M. Hori, Surf. Coatings Technol. **228**, S15 (2012).

[35] P. J. Fallon, V. S. Veerasamy, C. A. Davis, J. Robertson, G. A. J. Amaratunga, W. I.

Milne, and J. Koskinen, Phys. Rev. B **49**, 2287 (1994).

[36] M. J. Kushner, IEEE Trans. Plasma. Sci. **14**, 188 (1986).

[37] Y. P. Song, D. Field, and D. F. Klemperer, J. Phys. D **23**, 673 (1990).

[38] M. A. Lieberman and A. J. Lichtenberg, *Principles of Plasma Discharges and Materials Processing* (Wiley, New Jersey, 2005) 2nd ed.

[39] A.D. Kuyper and H. J. Hopman, J. Appl. Phys. **67**, 1229 (1990).

[40] B. Chapman, *Glow Discharge Processes: Sputtering and Plasma Etching* (Wiley, New York ,1980).

Chapter 3 Emission Spectroscopy of Ar + H_2 + C_7H_8 Plasmas

3.1 Introduction

A Langmuir probe, which are widely used to measure electron density and electron temperature in reactive plasmas, is not always possible [1]. This is because of the high sensitivity of the Langmuir probe to low and medium energy electrons of the electron energy distribution (EED) [2]. When the contribution of energetic electrons on probe is relatively weak, it is different to obtain a precise result.

Optical emission spectroscopy (OES) as a noninvasive diagnostic is increasingly used for quantitative plasma analysis [3]. In particular, by using optical emission from rare gas as argon is expected to improve the accuracy in deriving the information on plasma parameters under the condition of excitation mechanisms are well established [4,5]. Moreover, Ar atoms are easily ionized as compared to H_2 molecules hence the film surface can be modified by resultant heavy Ar ions.

Since emission intensities give information about the generation rates of plasma species and other related parameters, we have carried out measurements of emission intensities by OES in our H-assisted plasma CVD reactor. Here, we report experimental results of toluene flow rate dependence and pressure dependence of Ar emission intensities for Ar + H_2 + C_7H_8 plasmas.

3.2 Experimental Details

Ar and H_α emission intensities were measured using the H-assisted plasma CVD reactor as shown in Fig. 2.1 [6,7]. The excitation frequency of the main discharge was 28 MHz and the supplied voltage was 150 V, and the H atom source and the self-biased RF discharge were not applied in this study. Toluene (C_7H_8), Ar and H_2 were supplied at flow

rates of 0.63–20, 60, and 30 sccm, respectively. C_7H_8 was vaporized at 150℃ and introduced into the reactor with H_2. The total pressure was set in a range of 0.1–5 Torr. The substrate temperature was 100℃.

As shown in Fig. 3.1, optical emission intensities were measured with a miniature fiber optic spectrometer (Ocean Optics USB2000+). The distance between main discharge electrode and substrate electrode is 33 mm. Here, we measured emission intensity with a collimating lens to obtain information of plasma parameters in the bulk (at the range of 0–30 mm above the center of substrate electrode). However, the structures of plasma vary with the gas pressure, and many reactions occur near the electrode in specially [8]. Thus, measurement regarding to the spatial distribution of emission intensities with a thin steel pipe (1 mm inner diameter) was also performed (5, 10, 15, 20, 25, and 30 mm above the center of substrate electrode).

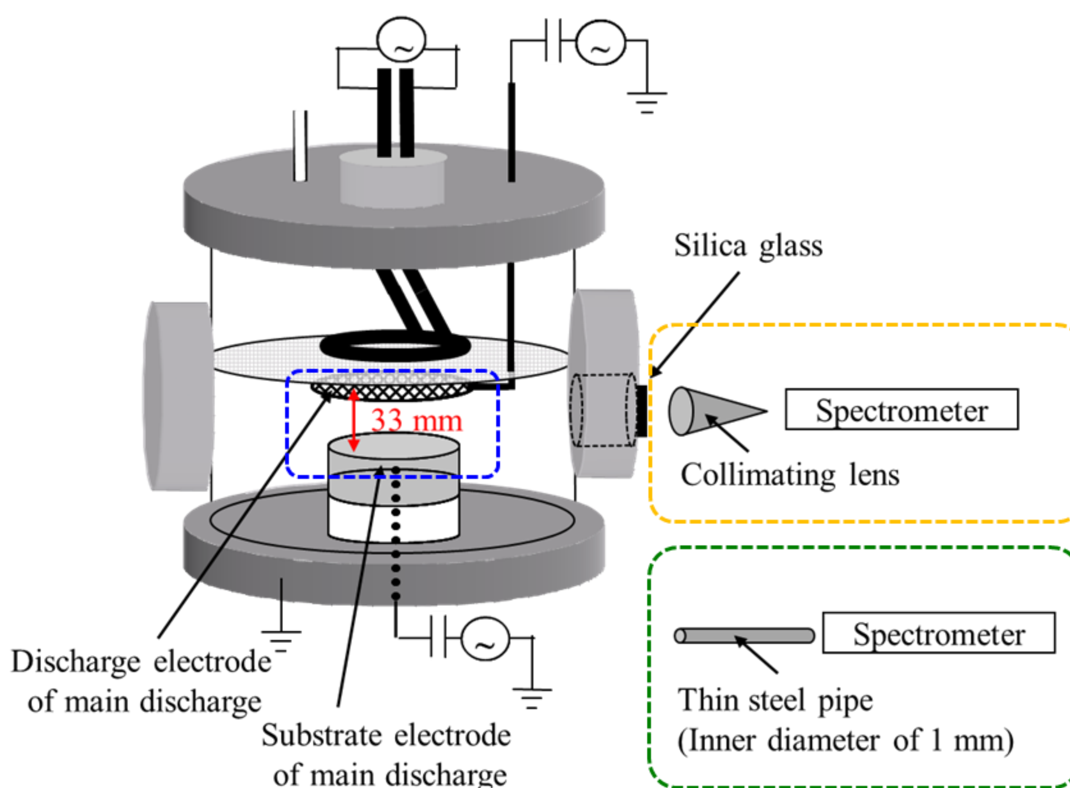

Fig. 3.1. Schematic of measurement of emission intensities with a collimating lens or a thin steel pipe.

3.3 Results and Discussion

Figure 3.2 shows typical emission spectra for plasmas of (a) Ar(100%), (b) Ar + H_2(33%), and (c) Ar + H_2(32.4%) + C_7H_8(0.027%) plasmas at 0.1 Torr. The emission intensities for Ar + H_2(33%) are a half of those for Ar(100%). The emission intensities for Ar + H_2(32.4%) + C_7H_8(0.027%) are a third of those for Ar(100%). Most Ar emission intensities are proportional to Ar partial pressure, electron density, and the rate coefficients for electron impact excitation from the Ar ground state. The emission intensities for Ar + H_2(33%) are weak compared to those for Ar(100%) mainly due to the decrease in the Ar partial pressure. In other words, the electron density and the excitation rate coefficients (effective electron temperature) are nearly the same for Ar(100%) and Ar + H_2(33%) plasmas. These results are consistent with the fact that Ar^+ is the predominant ion in Ar(100%) plasmas, whereas Ar^+ and ArH^+ are the main ions in Ar + H_2(33%) plasmas in the pressure range of 0.1–5 Torr [9,10]. Because the Ar partial pressure of Ar + H_2(33%) and Ar + H_2(32.4%) + C_7H_8(0.027%) are nearly the same, the decrease in the emission intensities by adding C_7H_8 is caused by decreases in the high-energy electron density ($\varepsilon \geq$ 13 eV) and/or the excitation rate coefficients, which depend on electron temperature.

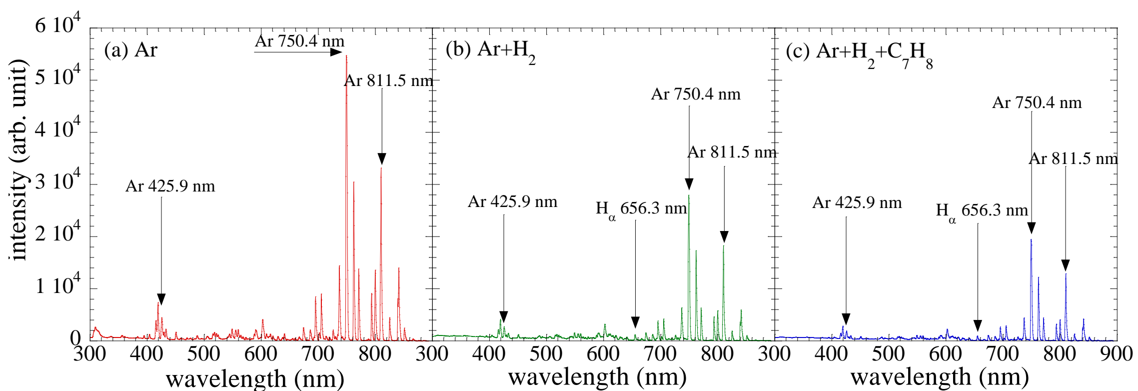

Fig. 3.2. Emission spectra for plasmas of (a) Ar, (b) Ar + H_2(33%), and (c) Ar + H_2(32.4%) + C_7H_8(0.027%). Total pressure is 0.1 Torr.

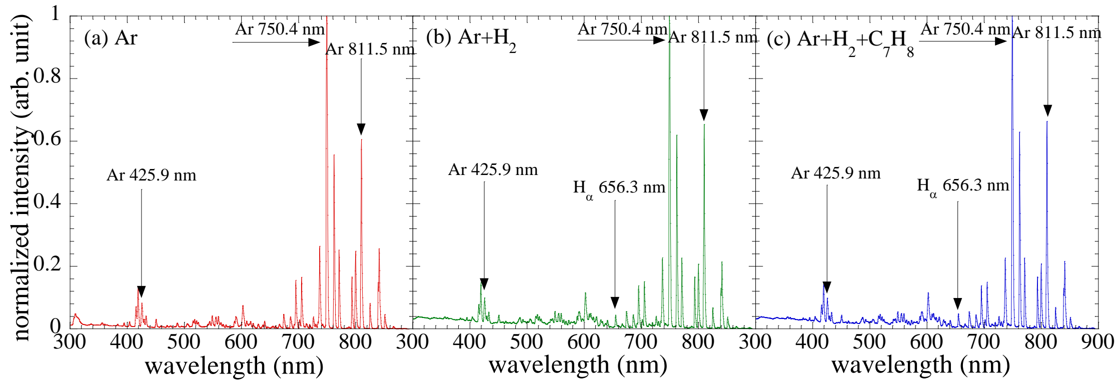

Fig. 3.3. Normalized emission spectra for plasmas of (a) Ar, (b) Ar + H_2(33%), and (c) Ar + H_2(32.4%) + C_7H_8(0.027%). Total pressure is 0.1 Torr.

To obtain insight into the mechanisms of the decrease in the emission intensities by adding C_7H_8, emission spectra were normalized by the intensity at 750.4 nm $I_{750.4}$ in each subgraph of Fig.3.2 as shown in Fig.3.3. The normalized three spectra in Fig.3.3 are similar with each other, indicating that effective electron temperature of these three plasmas is almost the same. Therefore, the decrease in the emission intensities by adding C_7H_8 is caused mainly by the decrease in the high-energy electron density. Moreover, there exists H_α emission for Ar + H_2(33%) and Ar + H_2(32.4%) + C_7H_8(0.027%) in Fig.3.3.

Figure 3.4 shows the toluene flow rate dependence of Ar emission intensities at (a) 750.4 nm, (b) 811.5 nm, and (c) 425.9 nm. It can be seen a sudden drop in the $I_{425.9}$, $I_{811.5}$ and $I_{750.4}$ after introducing C_7H_8, then all of them have a linear decrease with increasing the toluene flow rate from 0.63 to 20 sccm. Ar emissions at 425.9 nm and 750.4 nm have little influence of quenching and radiation trapping, and their upper levels of $2p_1$ (excitation energy of 13.5 eV) and $3p_1$ (excitation energy of 14.7 eV) have small cross section for electron impact excitation from metastable states [11, 12]. Therefore, the ratio of emission intensity of Ar at 425.9 nm to that at 750.4 nm, Ar $I_{425.9}$/Ar $I_{750.4}$ is used to evaluate the effective electron temperature. The Ar emission at 811.5 nm is strongly influenced by the $1s_5$ metastable state (excitation energy of 11.5 eV) that can provide an additional channel for Ar atom excitation by low-energy electrons ($1.5 \leq \varepsilon \leq 3$ eV). So the emission intensity

ratio, Ar $I_{811.5}$/Ar $I_{750.4}$ is used to obtain information on the Ar 1s_5 metastable density and/or the low-energy electron density [13, 14].

The Ar emission intensity ratios are shown in Fig.3.5. Both the ratios are nearly constant irrespective of the toluene flow rate, showing that the effective electron temperature, Ar 1s_5 metastable density and/or low-energy electron density remain almost the same. These results indicate that the high-energy electron density decreases with increasing the toluene flow rate from 0 to 20 sccm. The total flow rate increases from 90 sccm to 110 sccm with increasing toluene flow rate from 0 to 20 sccm. The change of the total flow rate is small. In addition, the discharge voltage was kept constant in this study. Therefore the total flow rate and the discharge voltage have little influence on plasma parameters in this study.

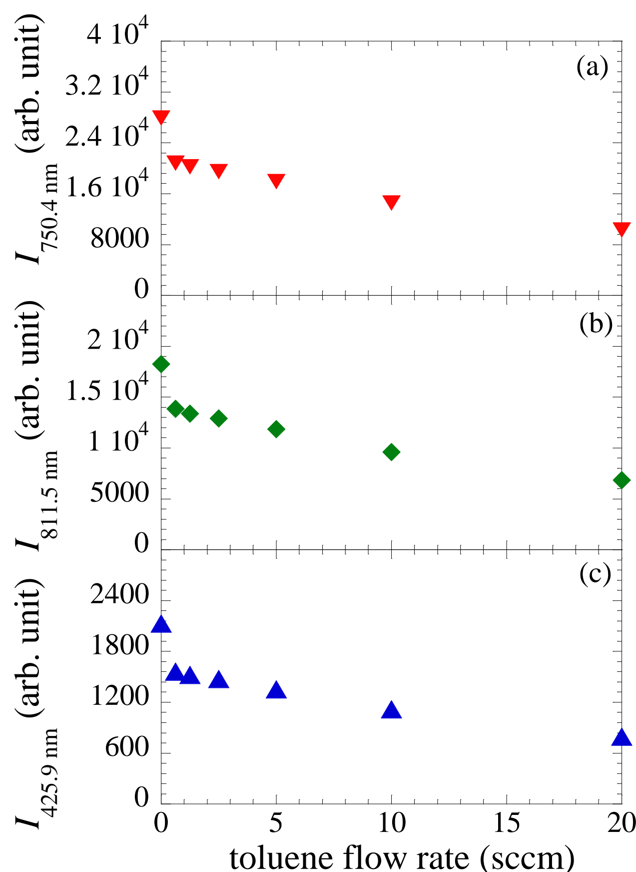

Fig. 3.4. Toluene flow rate dependence of Ar emission intensities at (a) 750.4nm, (b) 811.5 nm, and (c) 425.9 nm. Total pressure is 0.1 Torr.

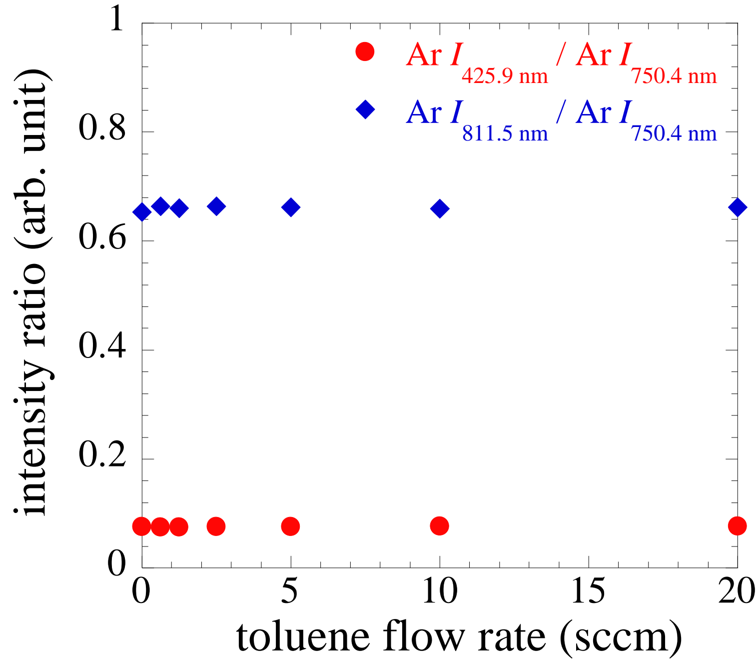

Fig. 3.5. Toluene flow rate dependence of Ar emission intensity ratios. Total pressure is 0.1 Torr.

Figure 3.6 shows the total pressure dependence of Ar emission intensities at 425.9 nm, 750.4 nm, and 811.5 nm, normalized by each intensity for 0.1 Torr. To obtain information of plasma parameters in the bulk region, we have measured the emission intensities at the range of 0–30 mm above the center of substrate. Though $I_{750.4}$ has a slight increase in the pressure range of 0.5–1.5 Torr, $I_{425.9}$ and $I_{811.5}$ decrease significantly with increasing the total pressure from 0.1 to 5 Torr.

The corresponding normalized Ar emission intensity ratios of Fig.3.6 are shown in Fig.3.7. Ar $I_{425.9}$/Ar $I_{750.4}$ and Ar $I_{811.5}$/Ar $I_{750.4}$ decrease by 84.3% and 55.6% with increasing the pressure from 0.1 to 3 Torr, and then they decrease by 24.6% and 4.8% with further increasing the pressure from 3 to 5 Torr. These results indicate that the effective electron temperature, Ar $1s_5$ metastable density and/or low-energy electron density decrease significantly with increasing the total pressure from 0.1 to 3 Torr, and then they decrease slightly with further increasing the total pressure from 3 to 5 Torr.

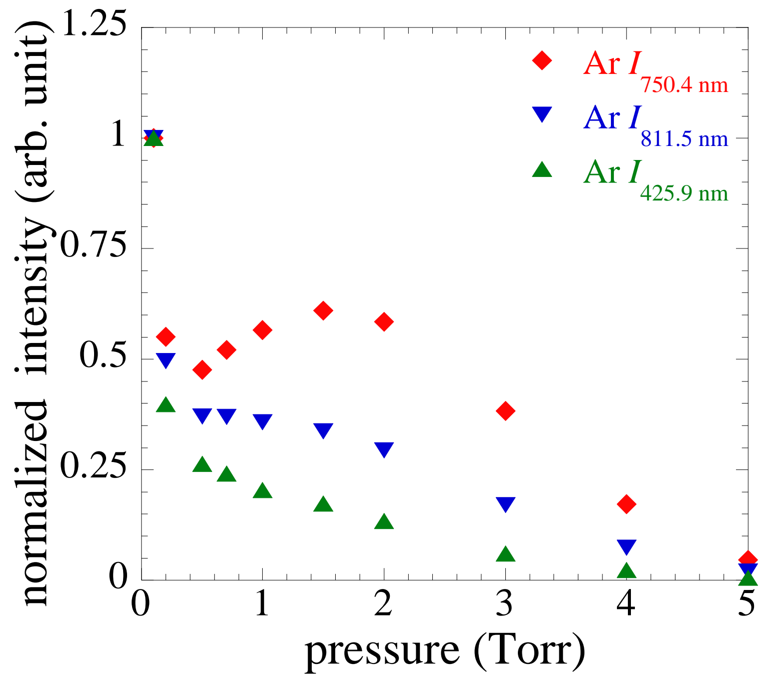

Fig. 3.6. Pressure dependence of normalized Ar emission intensities.

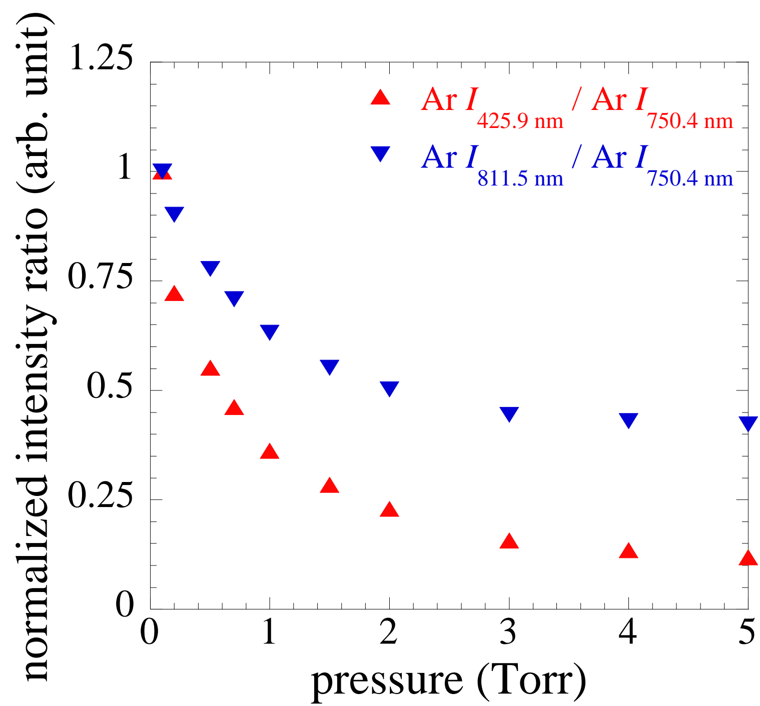

Fig. 3.7. Pressure dependence of normalized Ar emission intensity ratios.

3.4 Summary

We studied the toluene flow rate and pressure dependence of emission intensities in Ar + H_2 + C_7H_8 plasmas. The following conclusions are obtained in this study.

(1) Electron density and the electron impact excitation rate coefficients (effective electron temperature) are nearly the same for Ar(100%) and Ar + H_2(33%) plasmas.

(2) Toluene addition leads to a decrease in the high-energy electron density, whereas the effective electron temperature and low-energy electron density remain almost the same.

(3) The effective electron temperature, Ar $1s_5$ metastable density and/or low-energy electron density decrease significantly with increasing the total pressure from 0.1 to 5 Torr.

References:

[1] R. H. Huddlestone and S. L. Leonard, in *Plasma Diagnostic Techniques* (Academic Press, New York, 1965).

[2] I. D. Sudit and F. F. Chen, Plasma Sources Sci. Technol. **3**, 162 (1994).

[3] T. Czerwiec and D. B. Graves, J. Phys. D **37**, 2827 (2004).

[4] M.V. Malyshev and V. M. Donnelly, J. Vac. Sci. Technol. A **15**, 550 (1997).

[5] S. A. Moshkalyov, J .A. Diniz, J. W. Swart, P. J. Tatsch, and M. Machida, J. Vac. Sci. Technol. B **15**, 2682 (1997).

[6] K. Takenaka, M. Kita, T. Kinoshita, K. Koga, M. Shiratani, and Y. Watanabe, J. Vac. Sci. Technol. A **22**, 1903 (2004).

[7] J. Umetsu, K. Koga, K. Inoue, H. Matsuzaki, K. Takenaka, and M. Shiratani, Surf. Coat.Technol. **202**, 5659 (2008).

[8] Y. P. Raizer, *gas discharge physics* (Allen, Oxford, 1991).

[9] M. Sode, T. Schwarz-Selinger, and W. Jacob, J. Appl. Phys. **113**, 093304 (2013).

[10] E. Neyts, M. Yan, A. Bogaerts, and R. Gijbels, Nucl. Instrum. Methods Phys. Res., Sect. B **202**, 300 (2003).

[11] G. A. Piech, J. B. Boffard, M. F. Gehrke, L. W. Anderson, and C .C. Lin, Phys. Rev. Lett. **81**, 309 (1998).

[12] J. B. Boffard, C. C. Lin, and C. A. DeJoseph Jr., J. Phys. D **37**, R143 (2004).

[13] N. Sadeghi, D. W. Setser, A. Francis, U. Czarnetzki, and H. F. Döbele, J. Chem. Phys. **115**, 3144 (2001).

[14] S. A. Moshkalyov, P. G. Steen, S. Gomez, and W. G. Graham, Appl. Phys. Lett. **75**, 328 (1999).

Chapter 4 Effects of Gas Pressure, Discharge Voltage, and Gas Flow Rate Ratio on the formation of a-C:H Films

4.1 Introduction

Hydrogenated amorphous carbon (a-C:H) films, due to their mechanical hardness, chemical stability, and optical transparency, have received a considerable amount of attention recently [1]. As one of the most important materials for nanotechnology, the a-C:H films have been used in a wide variety of nanosystems including micro-electromechanical systems (MEMS) and nano-electromechanical systems (NEMS) [2]. This is because of the ability of a-C:H that contains two essentially different bonding configurations, namely sp^3 (diamond-like) and sp^2 (graphite-like) configurations [3]. Meanwhile, the properties of a-C:H films are strongly dependent on hydrogen content, which is closely related to the carbon-hydrogen bonds [4].

Thus far, we have succeeded in controlling deposition profiles of a-C:H films on trench substrates using a H-assisted plasma CVD method, and realized conformal, subconformal and anisotropic deposition profiles, for which carbon is deposited in trenches with only top deposition and in trenches without sidewall deposition (with top and bottom deposition) [5,6]. Among the processes in the fabrication of MEMS devices, plasma CVD is usually employed to deposit thin films for manufacturing multi-layer structures [7]. Our deposition profile control method of depositing a-C:H films on patterned substrate is useful for the fabrication of MEMS devices.

Improvement of deposition rate is one of the concerns to meet the mass production in MEMS devices, while the maximum deposition rate in our previous study was 3.7 nm/min [8]. Deposition rate of a-C:H films in plasma CVD is closely related to synergetic effects of plasma species, which included carbon-containing neutral radicals, ions, and H atoms

[9,10]. The balance between deposition rate of carbon-containing neutral radicals and etch rate by H atoms determines net deposition rate. Bombardment of ions hardens films, and decreases the etch rate [11]. The generation rate of plasma species strongly depend on deposition conditions such as gas pressure, discharge voltage, and gas flow rate ratio [12]. The other concern of a-C:H films is the hardness which is closely related to the ratio of sp^3 to sp^2 configurations and the total hydrogen content in them.

Here, we investigated effects of gas pressure, discharge voltage, and gas flow rate ratio on deposition rate of a-C:H films. We derived the plasma parameters in the bulk and related to spatial profiles by optical emission spectroscopy (OES). Fourier transform infrared spectroscopy (FTIR) was used to investigate the hydrogen bonding configurations and hydrogen content in a-C:H films. We report the results of gas pressure, discharge voltage, and gas flow rate ratio dependence of the characteristics of a-C:H films.

4.2 Effects of Gas Pressure for Film Deposition

4.2.1 Experimental Details

Experiments relating to pressure dependence were performed using the H-assisted plasma CVD reactor as shown in Fig. 2.1 [13,14]. The excitation frequency of the main discharge was 28 MHz and the supplied voltage was 150 V, the H atom source and the self-biased RF discharge were not applied. Toluene (C_7H_8), Ar and H_2 were supplied at flow rates of 5, 60, and 30 sccm, respectively. C_7H_8 was vaporized at 150℃ and introduced into the reactor with H_2. The total pressure was set in a range of 0.1–5 Torr. The substrate temperature was 100℃.

The non-trench Si substrate on which films deposited was set on a stainless steel stair with four steps (5 mm in height). Thickness of deposited a-C:H films was obtained with a

scanning electron microscope (SEM: JEOL, JIB-4600F). Spatial distribution of emission intensities were measured at 5, 10, 15, 20, 25, and 30 mm above the center of substrate electrode with a miniature fiber optic spectrometer (Ocean Optics USB2000+) and a thin steel pipe (1 mm inner diameter).

4.2.2 Results and Discussion

Figure 4.1 shows the discharge statuses of main discharge electrode. The luminous intensity distribution at low pressure such as 0.1 Torr is substantially uniform. As the pressure increases the central portion becomes dark, only the portion near the two electrodes is luminous.

Figure 4.2 shows the Ar emission intensity ratios of Ar $I_{425.9}$/Ar $I_{750.4}$ and Ar $I_{811.5}$/Ar $I_{750.4}$. They decrease significantly with increasing the pressure from 0.1 to 5 Torr, which is consistent with the results measured in the bulk in Fig. 3.7. On the other hand, both the ratios nearly remain constant at each pressure irrespective of the spatial distance. These results indicate that the effective electron temperature, Ar $1s_5$ metastable density and/or low-energy electron density decrease significantly with increasing the pressure from 0.1 to 5 Torr, whereas they are almost constant irrespective of the spatial distance.

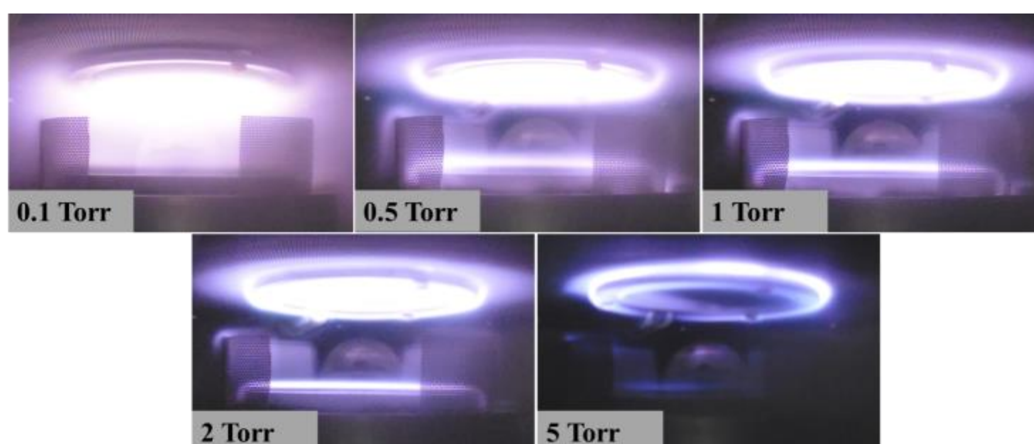

Fig. 4.1. Discharge statuses of main discharge electrode under the different pressure.

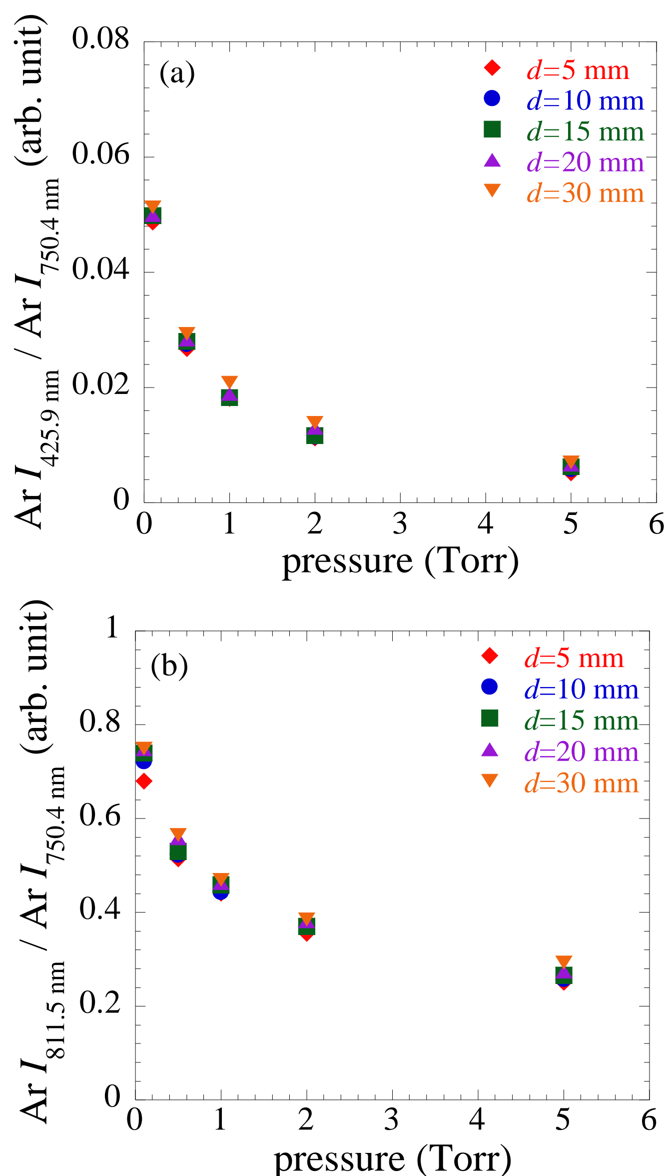

Fig. 4.2. Dependence of normalized Ar emission intensity ratio of (a) Ar $I_{425.9}$/Ar $I_{750.4}$ and (b) Ar $I_{811.5}$/Ar $I_{750.4}$ as a parameter of spatial distance from the substrate electrode.

The deposition rate dependence on spatial distance from the substrate electrode is shown in Fig. 4.3. The deposition rate of a-C:H films increases from 3.7 to 9 nm/min with increasing the supply of toluene from 0.63 to 5 sccm. Then it increases to 22.3 nm/min with increasing distance from the substrate electrode to 20 mm. Finally, it increases to 40.5 nm/min with increasing the gas pressure from 0.1 to 5 Torr. Figure 4.4 shows the film mass density dependence on spatial distance from the substrate electrode. Mean free path is

704.7 μm at 0.1 Torr, sheath thickness that equals several Debye length(106.6 μm) is less than the mean free path. Therefore, ion energy was derived from the potential difference between the plasma potential and the bias voltage owing to the collisionless sheath. Whereas mean free path is 14.1 μm at 5 Torr, which leads sheath thickness is more greater than it. Ions can be decelerated by collisions in the sheath in front of the substrates, namely, most ions have lower ion energies than the maximum ion energy. The film mass density at 5 torr is lower than that at 0.1 Torr owing to the collisional sheath.

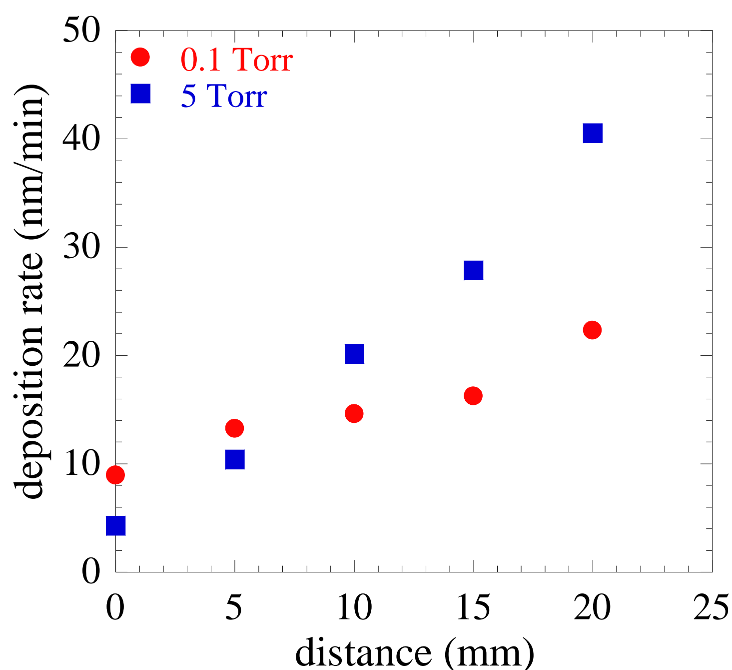

Fig. 4.3. Dependence of deposition rate and of a-C:H films on spatial distance from the substrate electrode as a parameter of pressure.

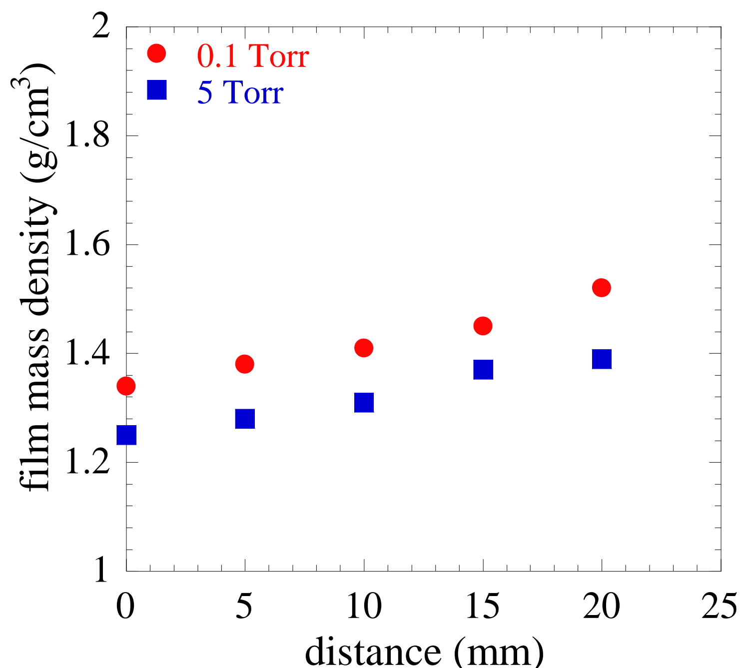

Fig. 4.4. Dependence of mass density of a-C:H films on spatial distance from the substrate electrode as a parameter of pressure.

4.2.3 Summary

We studied the pressure and spatial distance dependence of a-C:H film deposition and analyzed variations of plasma parameters based on OES. The effective electron temperature, Ar $1s_5$ metastable density and/or low-energy electron density decrease significantly with increasing the total pressure from 0.1 to 5 Torr, whereas they are almost constant irrespective of the spatial distance. The highest deposition rate of 40.5 nm/min is obtained in the spatial distance of 20 mm at the pressure of 5 Torr.

4.3 Effects of Discharge Voltage for Film Deposition

4.3.1 Experimental Details

Experiments relating to discharge voltage dependence were performed using the

H-assisted plasma CVD reactor as shown in Fig. 2.1. The main discharge was sustained between a mesh powered electrode of 85 mm in diameter and a plane substrate electrode of 85 mm in diameter at a distance of 32 mm. The excitation frequency of the main discharge was 28 MHz and the supplied voltage (V_{pp}) was 150−180 V. The H atom source was separated from the main discharge using a grounded mesh (30 meshes/inch) of 160 mm in diameter placed at 3 mm above the mesh powered electrode of main discharge. In this study, the H atom source and the self-biased RF discharge were not applied.

To obtain higher deposition rate, the Si substrate on which films deposited was set on a stainless steel step of 20 mm in height [15]. The substrate temperature was 100℃. Toluene (C_7H_8), Ar and H_2 were supplied at flow rates of 5, 80, and 10 sccm, respectively. C_7H_8 was vaporized at 150℃ and introduced into the reactor with H_2. The total pressure was 5 Torr.

Infrared absorption spectra were measured with a Fourier transform infrared spectrophotometer (JASCO FT-IR/620). Thickness of deposited a-C:H films was obtained with a scanning electron microscope (SEM: JEOL, JIB-4600F). Optical emission intensities were measured at 30 mm above the center of substrate electrode with an optical spectrometer (Ocean Optics USB2000+) and a thin steel pipe (1 mm inner diameter).

4.3.2 Results and Discussion

4.3.2.1 Hydrogen bonding configuration

The vibrational modes of the FTIR spectrum obtained from a-C:H films are classified into bending and stretching modes [16]. The bending modes are found between 1300 and 1700 cm^{-1} and those of stretching modes are found between 2850 and 3300 cm^{-1} [17]. In this study, bending modes possess higher deviations due to a less accurate curve fitting, so

only the stretching modes are used to quantify hydrogen content in a-C:H films.

Figure 4.5 shows the C–H stretching modes around 2900 cm^{-1} of a-C:H films. The intensity of absorption bands increases with increasing the discharge voltage from 150 to 160 V, whereas it decreases with increasing further the discharge voltage from 160 to 180 V. The obvious absorption bands at 2855, 2870, 2920 and 2960 cm^{-1} are due to the hydrogen in CH_2 (symmetric), CH_3 (symmetric), CH_2 (asymmetric) and CH_3 (asymmetric) stretching modes respectively. For these modes, H atoms are bonded to sp^3-type carbon [18]. Other C–H absorption bands are associated with CH (olefinic), CH (aromatic) and CH_2 (olefinic) stretching modes at 3020, 3060 and 3080 cm^{-1} respectively. For these modes, H atoms are bonded to sp^2-type carbon [19].

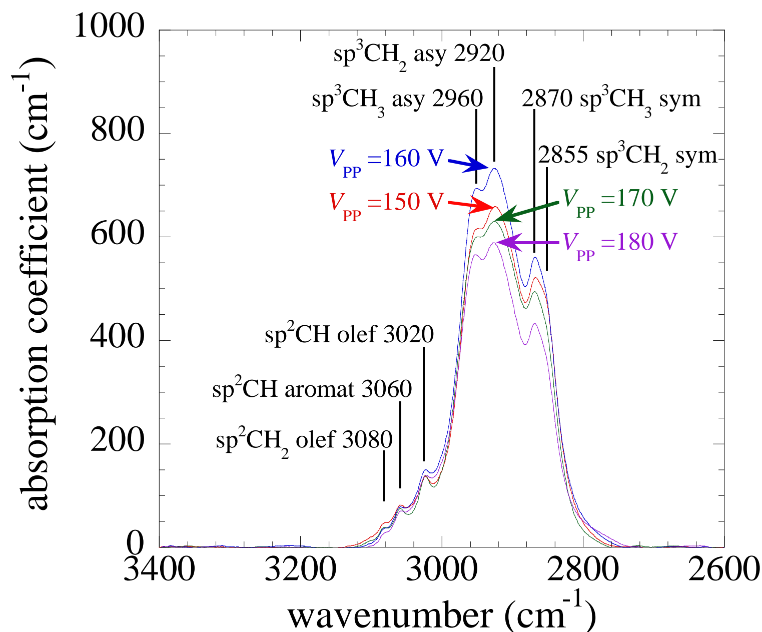

Fig. 4.5. Infrared absorption spectra of a-C:H films associated with the C–H stretching modes as a function of discharge voltage.

Figure 4.6 shows the curve fittings of stretching mode absorption bands. The errors include the uncertainty in the film thickness (as listed in Table IV), baseline correction, and curve fitting. The sp^3CH stretching mode is negligible during fitting procedure, because it is completely masked by the sp^3CH_2 asymmetric stretching mode in all our infrared absorption spectrum. As demonstrated in Fig. 4.7, the satisfactory fits with some minor

errors are obtained.

Table IV. Dependence of film thickness of a-C:H films on discharge voltage.

discharge voltage (V)	film thickness (nm)
150	8542.6±162.7
160	9457.6±78.9
170	11344.4±119.6
180	7913.3±93.0

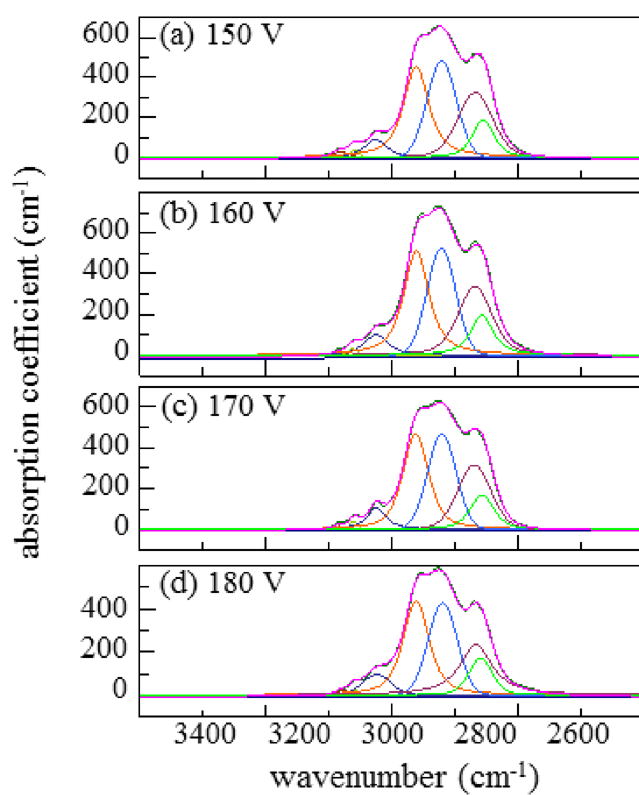

Fig. 4.6. Curve fittings of stretching mode absorption bands for a-C:H films deposited at the discharge voltage of (a) 150 V, (b) 160 V, (c) 170 V, and (d) 180 V.

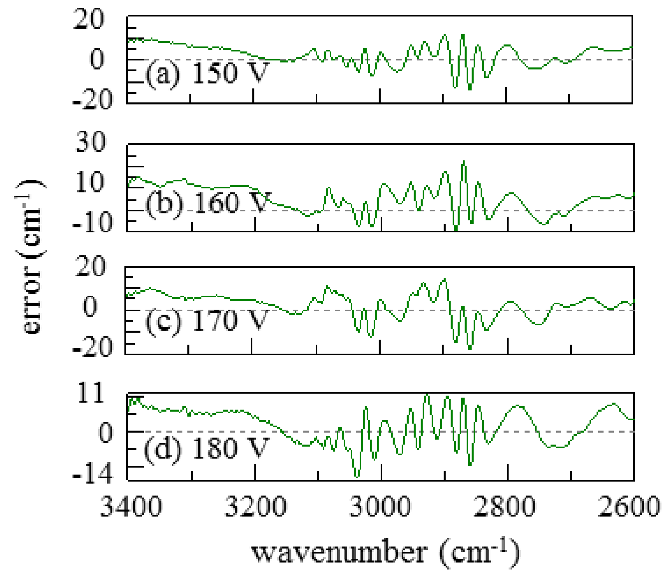

Fig. 4.7. Errors in curve fittings of stretching mode absorption bands for a-C:H films deposited at the discharge voltage of (a) 150 V, (b) 160 V, (c) 170 V, and (d) 180 V.

Hereafter we employ discharge voltage squared dependence, because V_{pp}^2 is proportional to power, and power is proportional to electron density n_{e}. The relative absorption intensity is evaluated by the each absorption line area of the fits. Figure 4.8 shows the relative absorption intensity of each configuration. All of the intensities remain nearly constant irrespective of the discharge voltage squared. The results from Fig. 4.5–4.8 indicate that our a-C:H films contain a large number of sp^3 configurations (93%) and a few sp^2 configurations (7%).

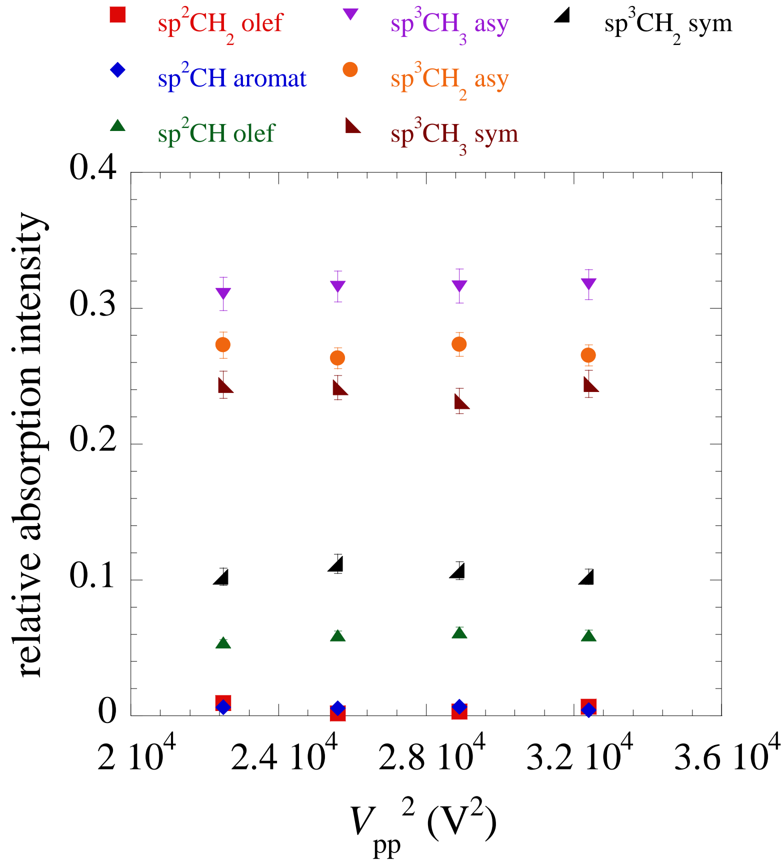

Fig. 4.8. Dependence of relative absorption intensity to C–H stretching modes on discharge voltage squared.

4.3.2.2 Hydrogen content in films

The curve fittings of the absorption spectra listed in Fig.4.6 assign a partial absorption coefficient to each stretching mode. The basis for a quantitative analysis of the bonded hydrogen is that the integrated partial absorption coefficients are proportional to the densities of the sp^xCH_y configuration to that mode [20]. Symmetric and asymmetric modes of the same configuration are summed up for clarity. The hydrogen content in a-C:H films is calculated by [21-23]

$$N_i = \frac{\int \alpha_i(\tilde{\nu}) d\tilde{\nu}}{\sigma_i \langle \tilde{\nu} \rangle_i} \tag{4.1}$$

where N_i is the number density of H atoms in respective configuration, $\alpha_i(\tilde{\nu})$ is the partial absorption coefficient, σ_i is the average absorption cross section of C–H vibrations

deduced from HFS, and $\langle\tilde{\nu}\rangle_i$ is the average wave number of the absorption band i. The method of deducing σ_i is described in the section 5.3.6.

The result of the quantitative analysis of bonded hydrogen in the method described above is show in Fig. 4.9. Most of the hydrogen is bonded in methyl groups (sp^3CH_3) which is consistent with the characteristic of PLCH [20]. The formation of PLCH films is mainly ascribed to the low ion energy (~30 V) and the low substrate temperature (100℃).

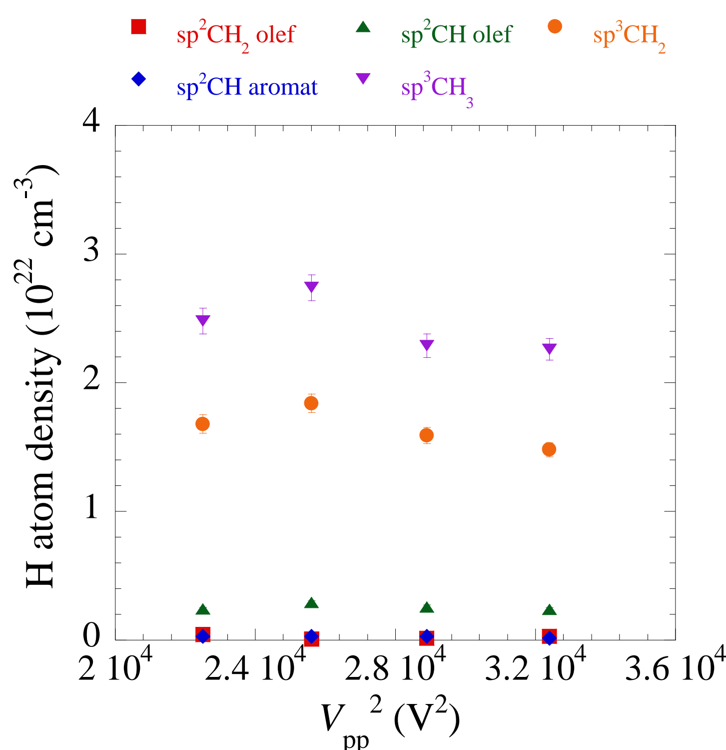

Fig. 4.9. Dependence of hydrogen atom density in respective configuration on discharge voltage squared.

The total hydrogen atom density which is the sum of that in respective configuration is shown in Fig. 4.10(a). The variation of hydrogen atom density with increasing the discharge voltage corresponds to that of absorption band intensity in Fig. 4.5. Figure 4.10(b) shows the discharge voltage squared dependence of deposition rate. The deposition rate increases with increasing the discharge voltage from 150 to 170 V, whereas it decreases significantly with further increasing the discharge voltage from 170 to 180 V. The highest deposition rate of 94.5 nm/min is obtained at 170 V. Figure 4.10(c) shows the

discharge voltage squared dependence of mass density. The variation of mass density with increasing the discharge voltage squared is exactly opposite to that of hydrogen atom density in Fig. 4.10(a).

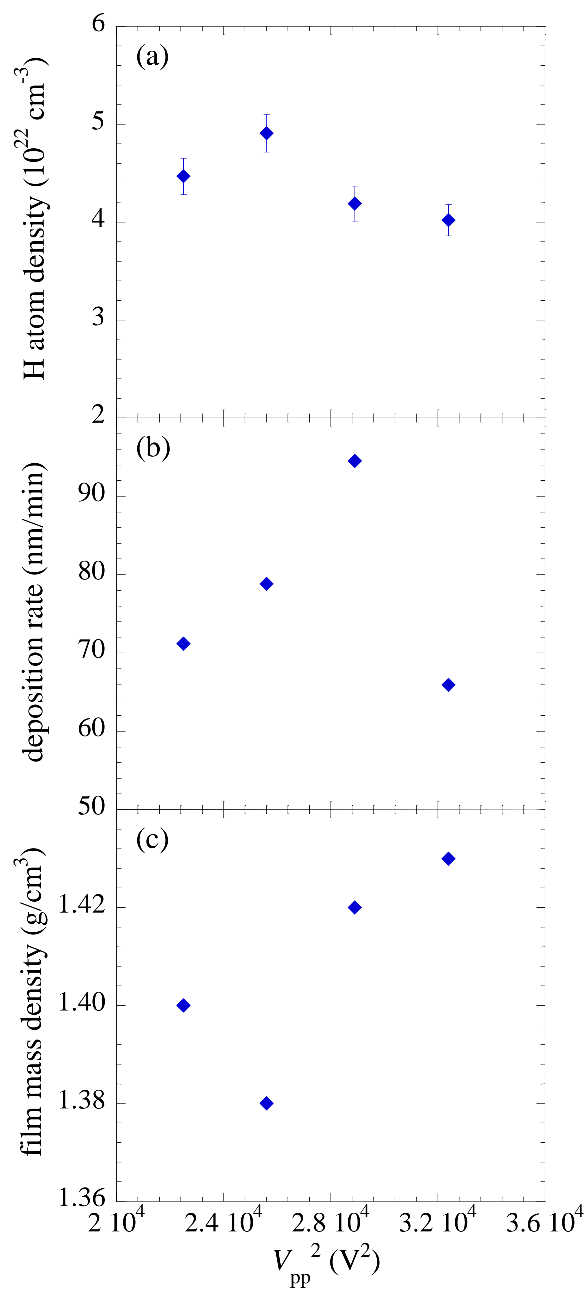

Fig. 4.10. Dependence of (a) hydrogen atom density, (b) deposition rate and (c) mass density of a-C:H films on discharge voltage squared.

Under the assumption that the transform from a-C to a-C:H is equal to the replacement of carbon atoms by hydrogen atoms in a-C films, the mass density dependence of hydrogen atom density obtained from C–H stretching modes is given by

$$m_{\mathrm{C}} N_{\mathrm{C}} \left(1 - \frac{N_{\mathrm{H}}}{x N_{\mathrm{C}}}\right) + m_{\mathrm{H}} N_{\mathrm{H}} = \rho \tag{4.2}$$

where m_{C} and m_{H} are the atomic mass of carbon and hydrogen, N_{C} and N_{H} are the number density of atoms in carbon and hydrogen, ρ is the density of a-C:H films, x means one carbon atom is replaced by x $(1 \ll x \ll 3)$ hydrogen atoms.

With the density of a-C films of 1.9 g/cm^3 [24,25], the mass density dependence of hydrogen atom density calculated according to Eq. (4.2) is shown in Fig. 4.11. The dashed line ($x = 1.6$) is well coincidence with the results obtained from C–H stretching modes. So the mass density has nearly linear decreases with increasing the hydrogen atom density, meaning that control of hydrogen content is crucial to obtain a-C:H films of high mass density. In addition, the hydrogen content in Fig. 4.11 (37.0–43.0 at.%) is less than that in PLCH as would have been expected (40–60 at.%) [26-28]. This discrepancy may be related with the presence of internal voids in PLCH [29].

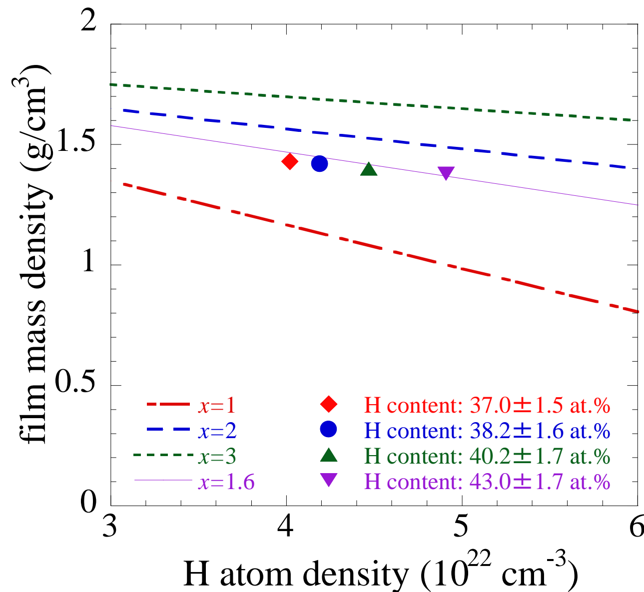

Fig. 4.11. The theoretical and experimental comparison of hydrogen atom density dependence of mass density of a-C:H films.

4.3.2.3 Plasma parameters

Optical emission spectroscopy has been carried out to obtain information on plasma parameters. Figure 4.12 shows the discharge voltage squared dependence of Ar emission intensity ratios. The Ar $I_{425.9}$/Ar $I_{750.4}$ is nearly constant irrespective of discharge voltage, the Ar $I_{811.5}$/Ar $I_{750.4}$ increases by 20.2% with increasing the discharge voltage from 150 to 180 V. These results show that effective electron temperature remains nearly the same, and Ar $1s_5$ metastable density and/or low-energy electron density increase with increasing the discharge voltage from 150 to 180 V. The discharge voltage squared dependence of normalized emission intensities is shown in Fig. 4.13. The increase rates of Ar $I_{750.4}$ and H_α $I_{656.3}$ are almost constant with increasing the discharge voltage from 150 to 170 V, whereas they increase by 7.4% and 84.1% respectively with increasing the discharge voltage from 170 to 180 V.

The results from Fig. 4.12 and Fig. 4.13 indicate that the decrease in deposition rate at 180 V is mainly attributed to a slight increase in radical generation rate and significant increases in H atom generation rate. In addition, a possible effect of chemical sputtering due to combined exposure to argon ions and hydrogen atoms should also be considered [30]. The increases in the emission intensities are mainly caused by increases in the high-energy electron ($\varepsilon \geq 13$ eV) density.

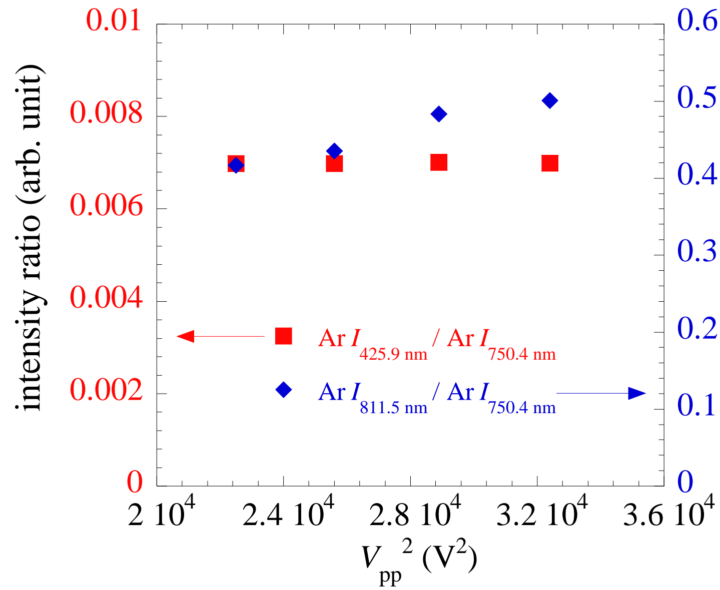

Fig. 4.12. Dependence of Ar emission intensity ratios on discharge voltage squared.

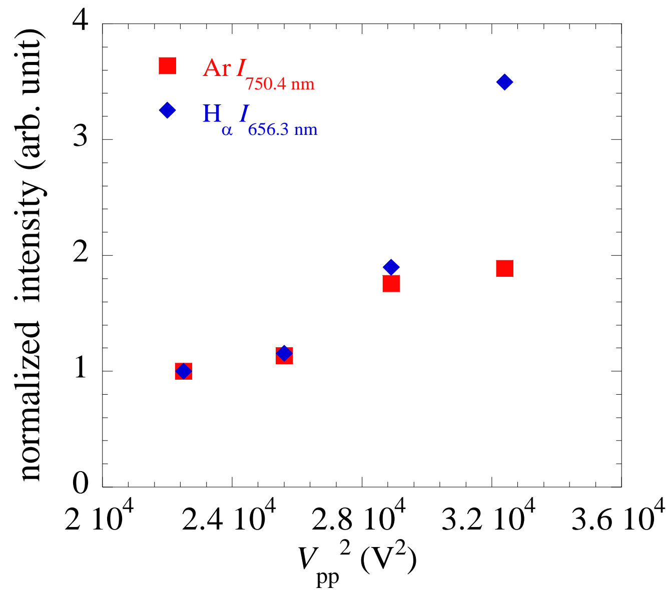

Fig. 4.13. Dependence of normalized emission intensities of Ar $I_{750.4}$ and H_α $I_{656.3}$ on discharge voltage squared.

4.3.3 Summary

We investigated the hydrogen bonding configurations and hydrogen content in a-C:H films prepared by the H-assisted plasma CVD method, and derived the plasma parameters related to deposition rate under various discharge voltage. The following conclusions are

obtained in this study.

(1) The deposited a-C:H films contain a large number of sp^3 configurations (93%) and a few sp^2 configurations (7%). Most of the hydrogen is bonded in methyl groups which shows the structure of deposited a-C:H films is PLCH.

(2) The mass density has nearly linear decreases with increasing the hydrogen atom density, meaning that control of hydrogen content is crucial to obtain a-C:H films of high mass density.

(3) The deposition rate increases with increasing the discharge voltage from 150 to 170 V, whereas it decreases significantly with further increasing the discharge voltage from 170 to 180 V. The decrease in deposition rate at 180 V is mainly attributed to a slight increase in radical generation rate and significant increases in etch rate by H atoms.

4.4 Effects of Gas Flow Rate Ratio for Film Deposition

4.4.1 Experimental Details

Experiments relating to gas flow rate ratio ($R = [\mathrm{H_2}]/([\mathrm{H_2}] + [\mathrm{Ar}])$) dependence were performed using the H-assisted plasma CVD reactor as shown in Fig. 2.1. The main discharge, which was sustained between a mesh-powered electrode of 85 mm diameter and a plane substrate electrode of 85 mm diameter at a distance of 33 mm, was employed to produce carbon-containing radicals as precursors. The excitation frequency of the main discharge was 28 MHz and the supplied voltage was 150 V. The H atom source was separated from the main discharge using a grounded mesh (30 meshes/in.) of 160 mm diameter placed 2 mm above the mesh-powered electrode of the main discharge. The H atom source and the self-biased RF discharge were not employed during deposition.

Toluene was supplied at flow rate of 5 sccm, and the total flow rate of H_2 and Ar was 90 sccm. Toluene was vaporized at 150℃ and introduced into the reactor with H_2. The total

pressure was 5 Torr and the substrate temperature was 100℃. To clarify the relation of spatial profiles (structure change) of plasma to film deposition, a-C:H films were deposited on Si substrates set on a stainless steel stair with four steps (5 mm in height).

Optical emission intensities were measured at the range of 0–30 mm above the center of the substrate electrode to obtain information on plasma parameters in the bulk with an optical spectrometer (Ocean Optics USB2000+) and a collimating lens. Film thickness was obtained with a scanning electron microscope (SEM, JEOL JIB-4600F). Infrared absorption measurements were performed with a Fourier transform infrared spectrophotometer (JASCO FT-IR/620).

4.4.2 Results and Discussion

4.4.2.1 Optical emission intensity

Spatial distributions of Ar emission intensities are reported in section 5.3.1, it demonstrated that generation rates of plasma species are higher near the mesh powered electrode of the main discharge. Here, Optical emission spectroscopy was carried out to measure dependence of generation rates on gas flow rate ratio. The variation of emission intensity ratio Ar $I_{425.9}$/Ar $I_{750.4}$ reflects change in effective electron temperature [31], and the variation of emission intensity ratio Ar $I_{811.5}$/Ar $I_{750.4}$ reflects change in Ar $1s_5$ metastable density and/or low-energy electron density ($1.5 \leq \varepsilon \leq 3$ eV) [32].

Figure 4.14 shows the gas flow rate ratio dependence of normalized Ar/[Ar] emission intensities. $I_{425.9}$, $I_{750.4}$, and $I_{811.5}$ decrease significantly with increasing the gas flow rate ratio, especially from 11 to 22%, indicating that the generation rates of carbon-containing neutral radicals and ions are higher at the lower gas flow rate ratio. Ar emission intensity ratios of Ar $I_{425.9}$/Ar $I_{750.4}$ and Ar $I_{811.5}$/Ar $I_{750.4}$ are shown in Fig. 4.15. The ratio of Ar

$I_{425.9}$/Ar $I_{750.4}$ is constant regardless of the gas flow rate ratio, whereas the ratio of Ar $I_{811.5}$/Ar $I_{750.4}$ decreases with increasing the gas flow rate ratio. These results indicate that the effective electron temperature is constant, Ar 1s$_5$ metastable density and/or low-energy electron density decrease with increasing the gas flow rate ratio from 11 to 55%.

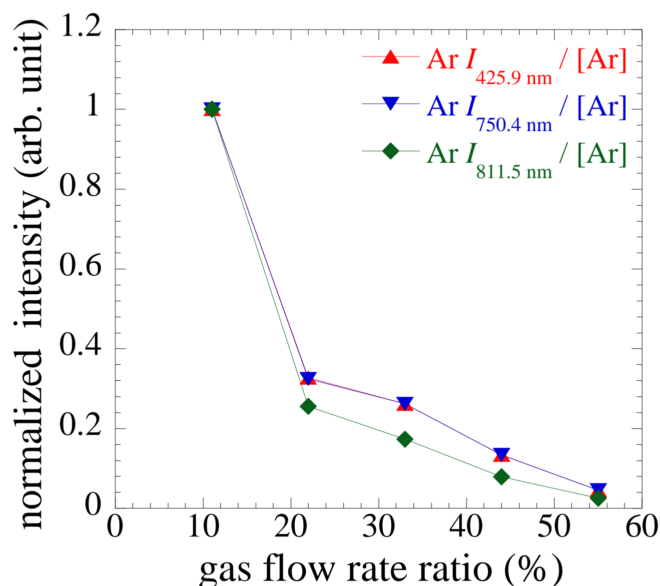

Fig. 4.14. Dependence of normalized Ar/[Ar] emission intensities at 425.9, 750.4, and 811.5 nm on gas flow rate ratio.

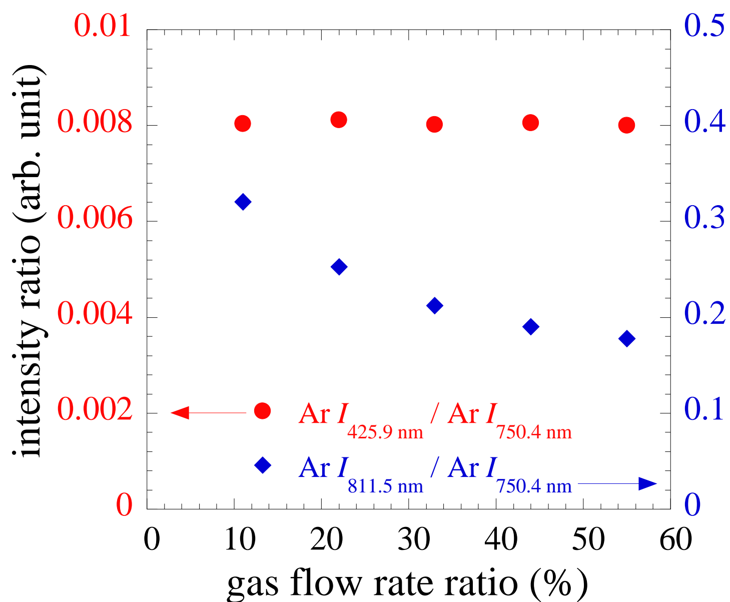

Fig. 4.15. Dependence of Ar/[Ar] emission intensity ratios on gas flow rate ratio.

4.4.2.2 Film deposition

Firstly, we studied the effects of carbon-containing neutral radicals flux and ion flux on deposition rate and mass density of a-C:H films. Owing to the increasing generation rates of plasma species, the carbon-containing neutral radical flux and ion flux increase with decreasing the gas flow rate ratio and with increasing the distance from the substrate electrode. Figure 4.16 shows the gas flow rate ratio dependence of the deposition rate as a parameter of the distance from the substrate electrode. Owing to the increase in carbon-containing neutral radical flux, the deposition rate increases with decreasing the gas flow rate ratio. Moreover, it increases with increasing the distance from the substrate electrode.

The gas flow rate ratio dependence of the film mass density is shown in Fig. 4.17. Likewise, the film mass density increases with decreasing the gas flow rate ratio and with increasing the distance from the substrate electrode. The highest deposition rate of 66.5 nm/min and mass density of 1.50 g/cm^3 are simultaneously obtained at the distance of 20 mm for the gas flow rate ratio of 11%. All these films are PLCH because of their low mass density ($\leq$ 1.50 g/cm^3). These results indicate that by adjusting carbon-containing neutral radical flux and ion flux, we have succeeded in depositing high mass density a-C:H films with a high deposition rate.

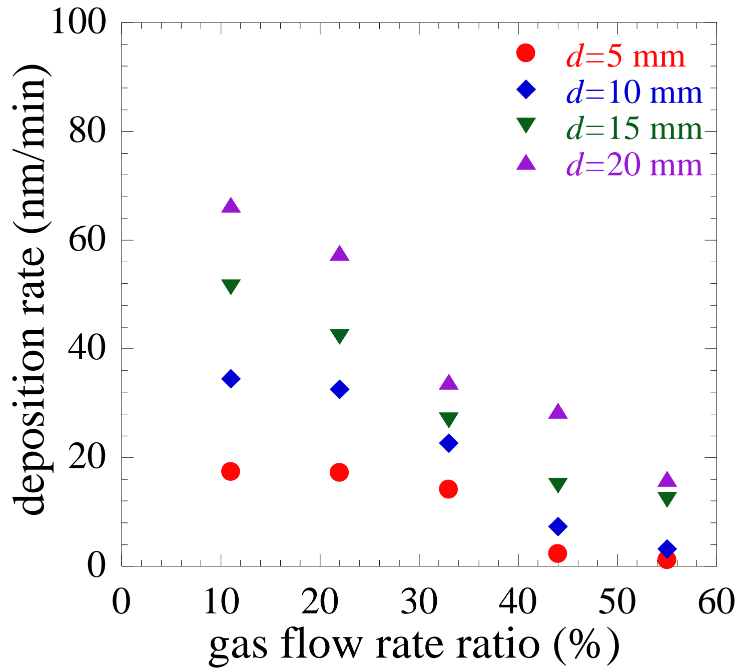

Fig. 4.16. Dependence of deposition rate of a-C:H films on gas flow rate ratio as a parameter of spatial distance from the substrate electrode.

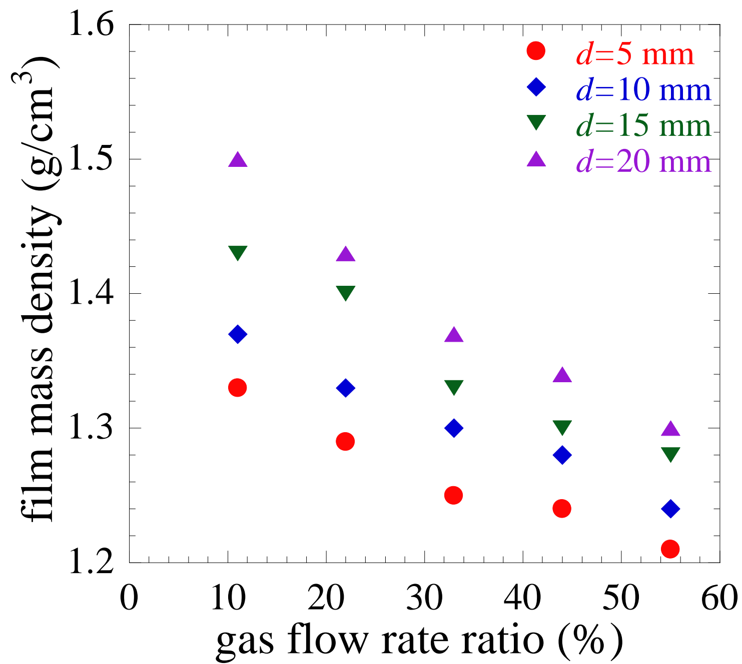

Fig. 4.17. Dependence of mass density of a-C:H films on gas flow rate ratio as a parameter of spatial distance from the substrate electrode.

4.4.2.3 Infrared absorption spectra of films

The infrared absorption spectra of a-C:H films obtained using Eq. (2.16) are shown in Fig. 4.18. The intensity of absorption bands decreases with increasing the gas flow rate ratio. This is the result of dehydrogenation due to breaking of the C–H bonds caused by the increase in ion flux [33,34].

Figure 4.19 shows the relative absorption intensity evaluated for each absorption line area by Gaussian curve fits, symmetric and asymmetric modes of the same configuration are summed up for clarity. Some error bars are smaller than the plot symbol sizes and are therefore omitted. The relative absorption intensity of each configuration nearly remains same irrespective of the gas flow rate ratio, and the films contain a large number of C–H sp^3 configurations (95%) and few C–H sp^2 configurations (5%).

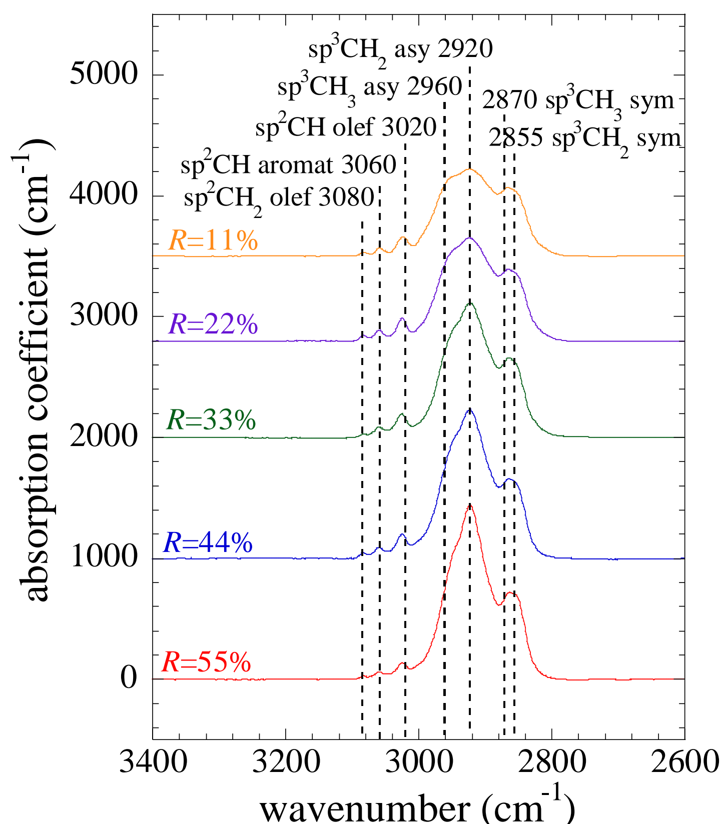

Fig. 4.18. Infrared absorption spectra of a-C:H films associated with the C–H stretching modes as a function of gas flow rate ratio at the distance of 20 mm.

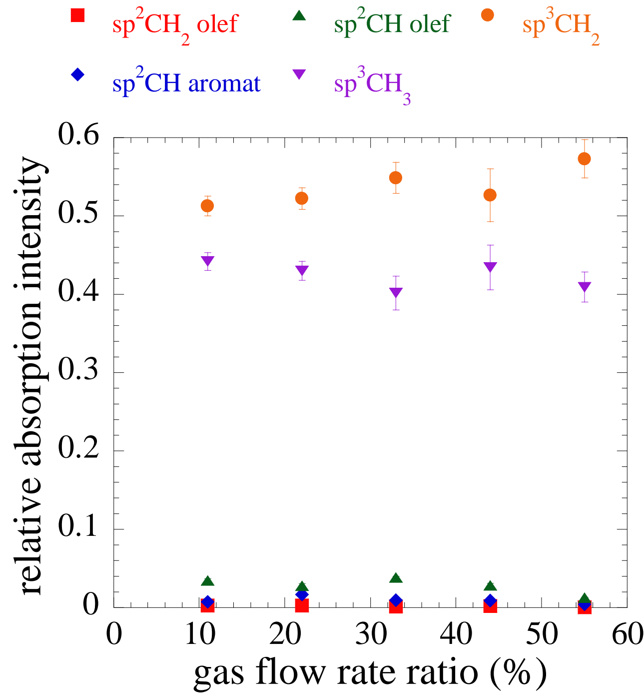

Fig. 4.19. Dependence of relative absorption intensity to C–H stretching modes on gas flow rate ratio at the distance of 20 mm.

4.4.2.4 Hydrogen content in films

The curve fittings of the absorption spectra assign a partial absorption coefficient to each stretching mode. The hydrogen content is calculated on the basis of integrated partial absorption coefficients are proportional to the densities of sp^xCH_y configuration to that mode using Eq. (4.1). Figure 4.20 shows gas flow rate ratio dependence of the H atom density in each configuration. The H atom density in sp^3 configuration has an obvious increase as the gas flow rate ratio increases. According to Eq. (4.2), the results of film mass density dependence of H atom density are shown in Fig. 4.21 [25]. The decrease in film mass density with increasing the total H atom density in all configurations is well coincidence with the solid line ($x = 1.8$). It means that the mass density of PLCH films depends on hydrogen content in the films.

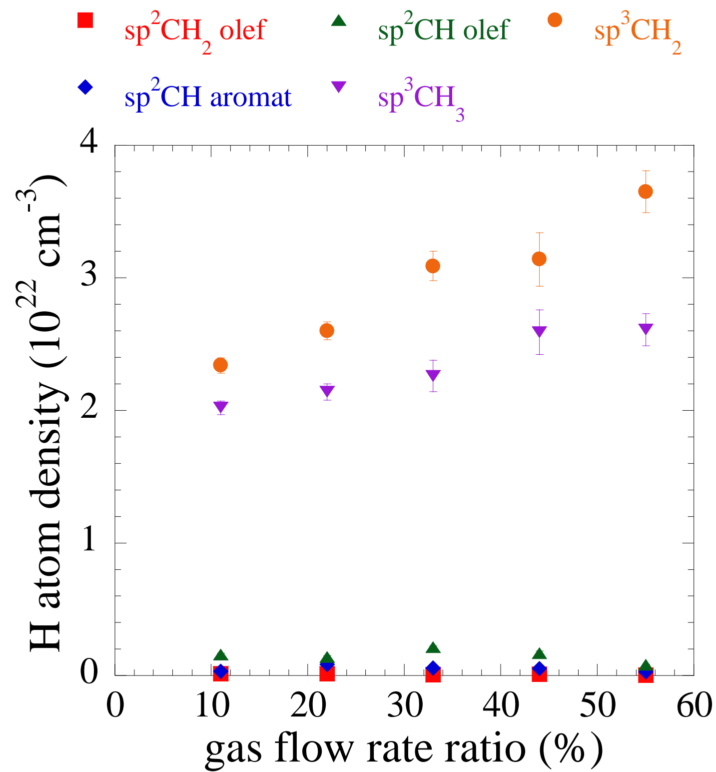

Fig. 4.20. Dependence of H atom density in respective configuration on gas flow rate ratio at the distance of 20 mm.

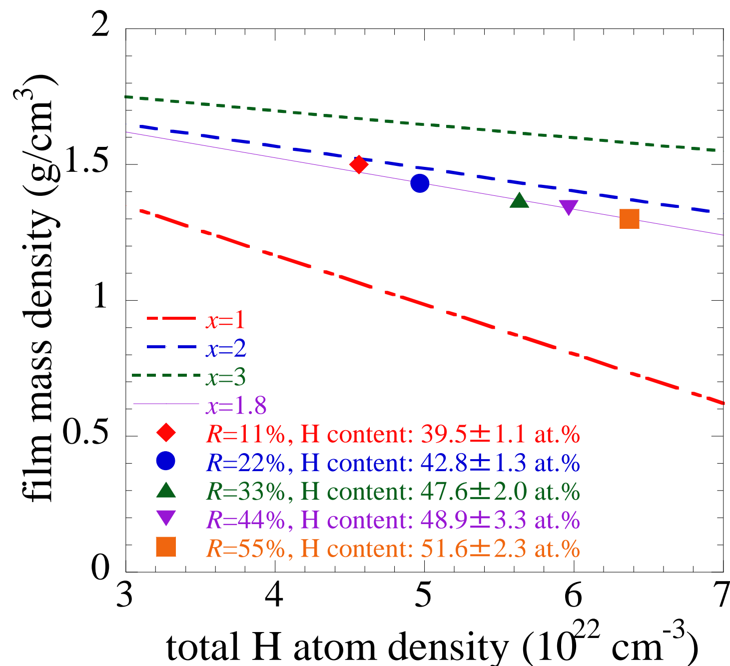

Fig. 4.21. The theoretical and experimental comparison of H atom density dependence of mass density of a-C:H films.

4.4.3 Summary

To discuss the deposition mechanism of a-C:H films, we investigated effects of gas flow rate ratio, and characterized the deposited films by FTIR. By control of gas flow rate ratio and distance from the substrate electrode, the highest deposition rate and highest mass density are obtained simultaneously at 20 mm for the gas flow rate ratio of 11%. The mass density of PLCH films depends on hydrogen content in the films.

References:

[1] J.-I. Suzuki and S. Okada, Jpn. J. Appl. Phys. **34**, L1219 (1995).

[2] S. A. Smallwood, K. C. Eapen, S. T. Patton, and J. S. Zabinski, Wear **260**, 1179 (2006).

[3] A. Zeng, V. F. Neto, J. J. Gracio, Q. H. Fan, Diamond Relat. Mater. **43**, 12 (2014).

[4] R. Kleber, K. Jung, H. Ehrhardt, I. Muhling, K. Breuer, H. Metz, and F. Engelke, Thin Solid Films **205**, 274 (1991).

[5] T. Urakawa, T. Nomora, H. Matsuzaki, D. Yamashita, G. Uchida, K. Koga, M. Shiratani, Y. Setsuhara, M. Sekine, and M. Hori, ISPC 20 Proc., 2011, POL02.

[6] K. Koga, T. Urakawa, G. Uchida, K. Kamataki, Y. Seo, N. Itagaki, M. Shiratani, Y. Setsuhara, M. Sekine, and M. Hori, PSE Proc., 2012, p. 136.

[7] J. Robertson, Jpn. J. Appl. Phys. **50** (2011) 01AF01.

[8] T. Urakawa, H. Matsuzaki, D. Yamashita, G. Uchida, K. Koga, M. Shiratani, Y. Setsuhara, M. Sekine, and M. Hori, Surf. Coatings Technol. **228**, S15 (2012).

[9] Q. Zhang, S. F. Yoon, A. Rusli, J. Ahn, H. Yang, and D. Bahr, J. Appl. Phys. **84**, 5538 (1998).

[10] B. B. Wang, K. Ostrikov, Z. L. Tsakadze, and S. Xu, J. Appl. Phys. **106**, 013315 (2009).

[11] T. Urakawa, R. Torigoe, H. Matsuzaki, D. Yamashita, G. Uchida, K. Koga, M. Shiratani, Y. Setsuhara, K. Takeda, M. Sekine, and M. Hori, Jpn. J. Appl. Phys. **52**, 01AB01 (2013).

[12] N. Mutsukura, S. Inoue, and Y. Machi, J. Appl. Phys. **72**, 43 (1992).

[13] M. Shiratani, H. J. Jin, K. Takenaka, K. Koga, T. Kinoshita, and Y. Watanabe, Sci. Technol. Adv. Mater. **2**, 505 (2001).

[14] K. Takenaka, M. Shiratani, M. Takashita, M. Kita, K. Koga, and Y. Watanabe, Pure Appl. Chem. **77**, 391 (2005).

[15] K. Koga, X. Dong, S. Iwashita, U. Czarnetzki, and M. Shiratani, J. Phys.: Conf. Ser. **518**, 012020 (2014).

[16] T. Heitz, B. Drévillon, C. Godet, and J. E. Bourée, Phys. Rev. B **58**, 13957 (1998).

[17] P. B. Nagabalasubramanian, S. Periandy, S. Mohan, and M. Govindarajan, Spectrochim. Acta, Part A **73**, 277 (2009).

[18] X. B. Yan, T. Xu, S. R. Yang, H. W. Liu, and Q. J. Xue, J. Phys. D **37**, 2416 (2004).

[19] X. M. He, K. C. Walter, M. Nastasi, S.-T. Lee, and X. S. Sun, Thin Solid Films **355–356**, 167 (1999).

[20] J. Ristein, R. T. Stief, L. Ley, and W. Beyer, J. Appl. Phys. **84**, 3836 (1998).

[21] J. H. Jaffe and S. Kimel, J. Chem. Phys. **25**, 374 (1956).

[22] O. Stenzel, R. Petrich, and M. Vogel, Opt. Mater. **2**, 125 (1993).

[23] J. Ristein, J. Schäfer, and L. Ley, Diamond Relat. Mater. **4**, 508 (1995).

[24] T. Nakayama, A. Miyake, H. Takase, S. Terashima, T. Sudo, Y. Watanabe, and Y Fukuda, SPIE Proc. **7271**, 72713 (2009).

[25] A. Dolgov, D. Lopaev, T. Rachimova, A. Kovalev, A Vasil'eva, C. J. Lee, V. M. Krivtsun, O. Yakushev, and F. Bijkerk, J. Phys. D **47**, 065205 (2014).

[26] C. Casiraghi, A. C. Ferrari, and J. Robertson, Phys. Rev. B **72**, 085401 (2005).

[27] A. C. Ferrari, A. Libassi, B. K. Tanner, V. Stolojan, J. Yuan, L. M. Brown, S. E. Rodil, B. Kleinsorge, and J. Robertson, Phys. Rev. B **62**, 11089 (2000).

[28] J. G. Buijnsters, R. Gago, I. Jiménez, M. Camero, F. A.-Rueda, and C. G.-Aleixandre, J. Appl. Phys. **105**, 093510 (2009).

[29] S. P. Louh, I. C. Leu, and M.H. Hon, Diamond Relat. Mater. **14**, 1005 (2005).

[30] M. Schlüter, C. Hopf, T. Schwarz-Selinger, and W. Jacob, J. Nucl. Mater. **376**, 33 (2008).

[31] S. A. Moshkalyov, J. A. Diniz, J. W. Swart, P. J. Tatsch, and M. Machida, J. Vac. Sci. Technol. B **15**, 2682 (1997).

[32] T. Czerwiec and D. B. Graves, J. Phys. D **37**, 2827 (2004).

[33] J. Robertson, Mater. Sci. Eng. R **37**,129 (2002).

[34] S. F. Yoon, H. Yang, A. Rusli, J. Ahn, Q. Zhang, and J. Electron. Mater. **27**, 46 (1998).

Chapter 5 Effects of Ion Flux and Ion Energy on Characteristics of a-C:H Films

5.1 Introduction

Hydrogenated amorphous carbon (a-C:H) are of special interest in various applications due to they with a wide range of electronic, optical, and mechanical properties [1,2]. The a-C:H forms a great variety of crystalline and disordered structures because it is a mixture of sp^3 (diamond-like), sp^2 (graphite-like), and even sp^1 configurations, with the presence of hydrogen. According to this, a-C:H is mainly classified into soft polymer-like a-C:H (PLCH) with a high hydrogen content (40–60 at.%) and hard diamond-like a-C:H (DLCH) with an intermediate hydrogen content (20–40 at.%) [3,4].

It has been found that the properties of a-C:H films are strongly influenced by deposition methods and deposition conditions [5]. The deposition methods mainly include ion beam deposition, sputter deposition, pulsed laser deposition, and plasma CVD [6,7]. Among these deposition methods, plasma CVD is the most common one used for the deposition of a-C:H films. For deposition conditions, the bombardment of ions impinging on the growing surface of a-C:H films plays an important role in controlling the sp^3 to sp^2 ratio and H content in films. The interpretation to the effects of ion bombardment is based on the physics process of subplantation and chemical process of dehydrogenation for a-C:H films [8,9].

In contrast with numerous investigations of a-C:H film deposition introduced CH_4, C_2H_2, C_2H_4, C_2H_6, C_3H_8, C_4H_{10}, and C_6H_6 as source gases [10,11], only a few reports of toluene (C_7H_8) could be found. The C_7H_8, with low ionization potential, thermal stability, and low hydrogen to carbon ratio, was employed in our H-assisted plasma CVD method, and succeeded in realizing conformal, subconformal, and anisotropic deposition profiles of

a-C:H films on fine trench substrates. For anisotropic deposition profiles, carbon is succeeded in depositing in trenches with only top deposition and in trenches without sidewall deposition (with top and bottom deposition) [12].

To obtain more anisotropic deposition profiles, we need investigate the deposition mechanisms of soft and hard films. That is, the effects of ion bombardment, combining with the deposition of carbon-containing neutral radicals, etching of H atoms, and sputtering of argon ions and H atoms [13].

Here, we derived the plasma parameters related to spatial distribution by optical emission spectroscopy (OES). Then, chemical bond configurations in films were determined by X-ray photoelectron spectroscopy (XPS) and Fourier transform infrared spectroscopy (FTIR). We also compared the hydrogen contents in films obtained by FTIR and hydrogen forward scattering spectrometry (HFS). Finally, we characterized the prepared films by Raman spectroscopy.

5.2 Experimental Details

Figure 2.1 shows the he H-assisted plasma CVD reactor in which we performed experiments [14]. This reactor provided independent control of the generation rates of carbon-containing radicals and H atoms. The excitation frequency of the main discharge was 28 MHz and the supplied voltage was 150 V. The H atom source was separated from the main discharge using a grounded mesh (30 meshes/in.) of 160 mm diameter placed 2 mm above the mesh-powered electrode of the main discharge. In addition, an RF bias voltage of 400 kHz was applied to the substrate to control the kinetic energy of incident ions and the corresponding substrate bias voltage was from −1.2 (floating) to −80 V. In this study, the H atom source was not employed during deposition.

Toluene, Ar, and H_2 were supplied at flow rates of 5, 60, and 30 sccm, respectively. Toluene has a low ionization potential of 8.82 eV and a methyl group, which is expected to

bring about a high deposition rate and an enhanced thermal stability of deposited a-C:H films respectively [15,16]. Toluene was vaporized at 150℃ and introduced into the reactor with H_2. The total pressure was 5 Torr. To clarify the relation of the properties of films to the deposition rate, namely, the deposition radical flux, a-C:H films were deposited on Si substrates set on a stainless steel stair with four steps (5 mm in height). The substrate temperature was 100℃. To study the contributions of ion bombardment, stainless steel meshes (aperture ratio of 37.6%) were placed 3 mm above each Si substrate in some experiments. Ion bombardment effects are suppressed by the meshes, whereas carbon-containing neutral radicals and H atoms can pass though the mesh.

In addition, ion energy was derived from the potential difference between the plasma potential and the bias voltage. In this study, ions can be decelerated by collisions in the sheath in front of the substrates, namely, most ions have lower ion energies than the maximum ion energy. Therefore, it was employed as a measure of the ion energy distribution. The average value of plasma potential over one RF cycle was 34 V derived from the peak-to-peak RF voltage and DC self-bias of main discharge [17].

To obtain information on generation rates of plasma species, optical emission intensities were measured at 5, 10, 15, 20, 25, and 30 mm above the center of the substrate electrode with an optical spectrometer (Ocean Optics USB2000+) and a thin steel pipe (1 mm inner diameter). Film thickness was obtained with a scanning electron microscope (SEM, JEOL JIB-4600F). Infrared absorption measurements were performed with a Fourier transform infrared spectrophotometer (JASCO FT-IR/620). Hydrogen content was measured by HFS with a tandem Pelletron accelerator (NEC 3SDH). Raman spectra were measured at room temperature with a laser Raman spectrometer (JASCO NRS-3100) using 532 nm excitation. XPS measurements were carried out with a Shimadzu AXIS-165x spectrometer using monochromatized Al Kα (1486.6 eV) X-ray radiation.

5.3 Results and Discussion

5.3.1 Spatial Profiles of Plasma Emission Intensities

Optical emission spectroscopy was carried out to obtain information on generation rates of plasma species. The variation of emission intensity ratio Ar $I_{425.9}$/Ar $I_{750.4}$ reflects change in effective electron temperature [18], and the variation of emission intensity ratio Ar $I_{811.5}$/Ar $I_{750.4}$ reflects change in Ar $1s_5$ metastable density and/or low-energy electron density ($1.5 \leq \varepsilon \leq 3$ eV) [19].

Figure 5.1 shows the spatial distribution of normalized Ar emission intensities. $I_{425.9}$, $I_{750.4}$, and $I_{811.5}$ increase significantly in superlinear ways with increasing distance from the substrate electrode, indicating that the generation rates of plasma species are higher near the mesh powered electrode of the main discharge [13]. The spatial profiles of Ar emission intensity ratios of Ar $I_{425.9}$/Ar $I_{750.4}$ and Ar $I_{811.5}$/Ar $I_{750.4}$ are shown in Fig. 5.2. The ratios increase very slightly with increasing distance from the substrate electrode. These results indicate that the effective electron temperature, Ar $1s_5$ metastable density, and/or low-energy electron density increase very slightly with increasing distance from the substrate electrode to 30 mm. Therefore, the increases in emission intensity in Fig. 5.1 are mainly caused by the increases in high-energy electron ($\varepsilon \geq 13$ eV) density.

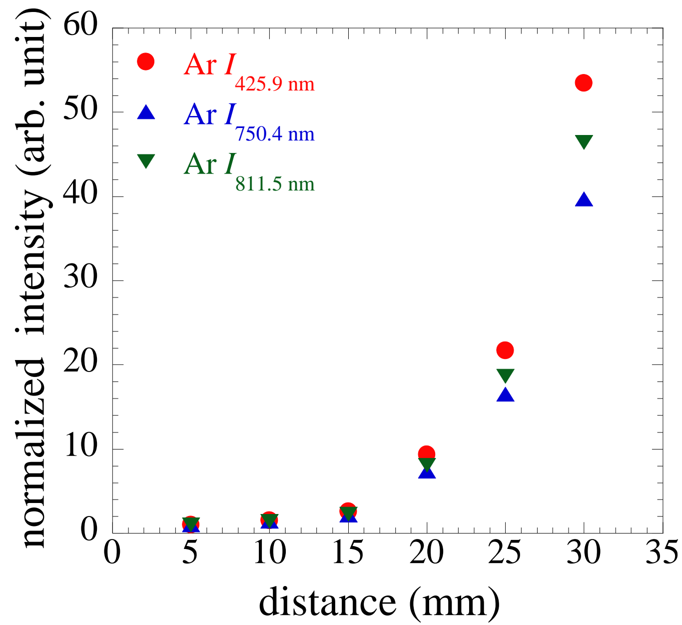

Fig. 5.1. Dependence of normalized Ar emission intensities at 425.9, 750.4, and 811.5 nm on spatial distance from the substrate electrode.

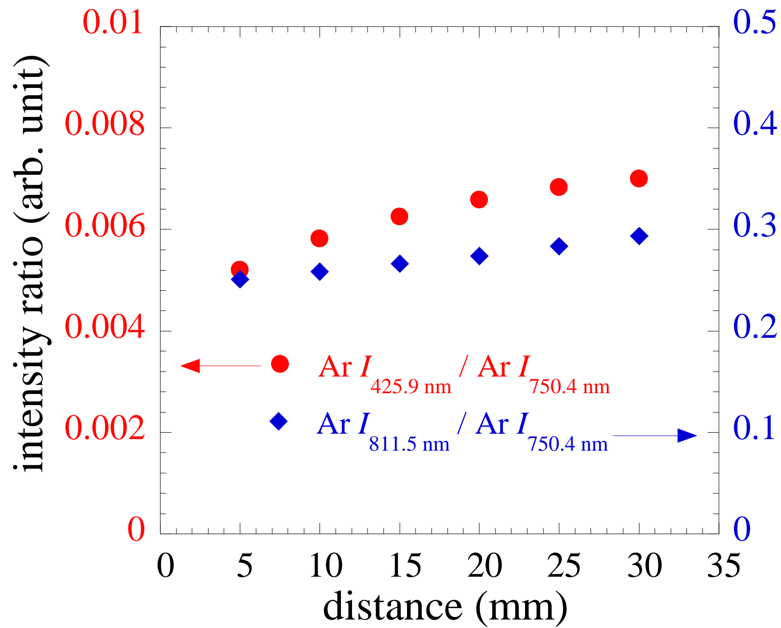

Fig. 5.2. Dependence of Ar emission intensity ratios on spatial distance from the substrate electrode.

5.3.2 Film Deposition

First, we studied the ion energy dependence of the deposition rate. Figure 5.3 shows the ion energy dependence of the deposition rate as a parameter of the distance from the substrate electrode. When the stainless steel meshes are placed above the substrate, that is, without ion bombardment, the deposition rate is significantly lower than that with ion bombardment. This is because soft a-C:H films are obtained without ion bombardment and such soft films are partly etched by H atoms. In addition, the deposition rate increases with increasing distance from the substrate electrode to 20 mm, since radical generation rates increase with the distance, as discussed in the previous section.

The ion energy dependence of the film mass density is shown in Fig. 5.4. The mass density without ion bombardment is lower than that with ion bombardment. Then, the mass density increases with increasing ion energy to 109 eV, whereas it decreases with increasing ion energy to 114 eV in a linear way. Likewise, the mass density increases with increasing distance from the substrate electrode to 20 mm. The highest mass density of 1.92 g/cm^3 with the high deposition rate of 43.4 nm/min is obtained at 20 mm for the ion energy of 109 eV.

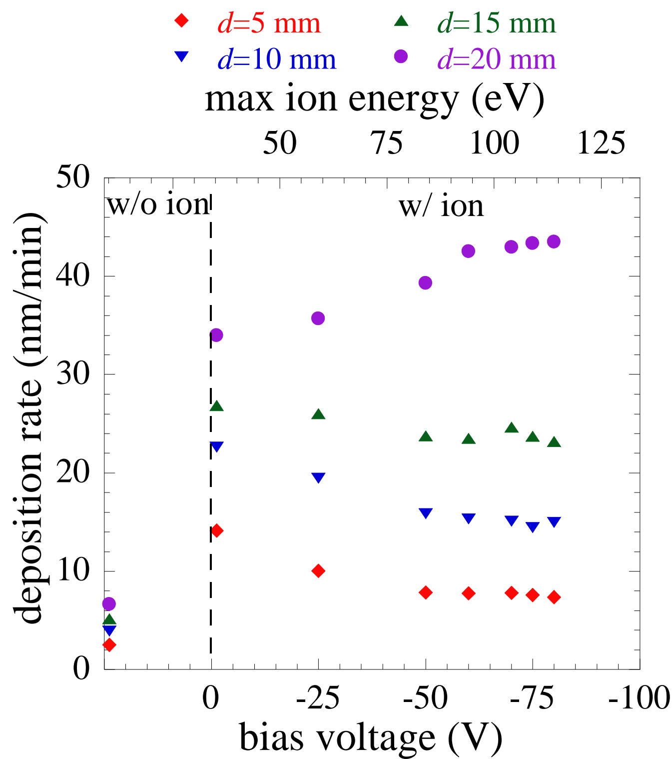

Fig. 5.3. Dependence of deposition rate of a-C:H films on bias voltage/max ion energy as a parameter of spatial distance from the substrate electrode.

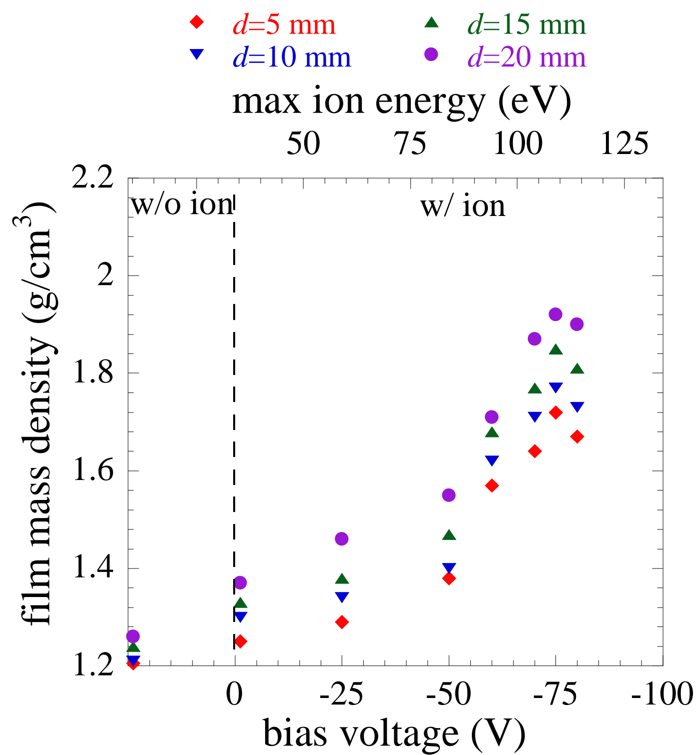

Fig. 5.4. Dependence of mass density of a-C:H films on bias voltage/max ion energy as a parameter of spatial distance from the substrate electrode.

5.3.3 Infrared Absorption Spectra

Owing to the bending modes between 1300 and 1700 cm^{-1} are superimposed with a broad phonon band induced by carbon skeleton between 500 and 1800 cm^{-1} [20]. Thus, only the stretching modes between 2850 and 3300 cm^{-1} are used to quantify the hydrogen content in a-C:H films in this study. Figure 5.5 shows the C–H stretching modes at approximately 2900 cm^{-1} of a-C:H films deposited at an ion energy of 35.2 eV. The intensity of absorption bands decreases with increasing distance from the substrate electrode, whereas the shape of absorption bands is nearly the same irrespective of the distance. The C–H absorption bands associated with CH_2 (symmetric), CH_3 (symmetric), CH_2 (asymmetric), and CH_3 (asymmetric) stretching modes at 2855, 2870, 2920, and 2960 cm^{-1} are all bonded in sp^3 configurations [21]. Other C–H absorption bands associated with CH (olefinic), CH (aromatic), and CH_2 (olefinic) stretching modes at 3020, 3060, and 3080 cm^{-1} are all bonded in sp^2 configurations [22].

Figure 5.6 shows an overview of the infrared absorption spectra obtained from a-C:H films deposited under various ion bombardment conditions. The intensity of absorption bands decreases from without ion bombardment to the ion energy of 84 eV, and it slightly changes with further increase in ion energy to 114 eV. Combining these results with the results of mass density in Fig. 5.4, above the ion energy of 84 eV, the drastic changes in the shape of absorption bands indicate the structural transition from PLCH to DLCH. Thus, the a-C:H films deposited from without ion bombardment to the ion energy of 84 eV are soft PLCH films, and the a-C:H films deposited in the ion energy range of 84–114 eV are hard DLCH films. The reduction in absorption intensity shows dehydrogenation due to breaking of the carbon-hydrogen bonds caused by the increase in ion energy [23]. H atoms are dissociated from carbon-hydrogen bonds by ion bombardment, then they recombine to form H_2 molecules, and eventually such H_2 molecules desorb from a-C:H films.

The curve fittings with errors of stretching mode absorption bands are shown in Fig. 5.7. The sp^3CH stretching mode is disregarded during the fitting procedure, because it is completely masked by the sp^3CH_2 asymmetric stretching mode in all our infrared absorption spectra. As demonstrated in Fig. 5.7, the satisfactory fits with minor errors are obtained for typical PLCH and DLCH.

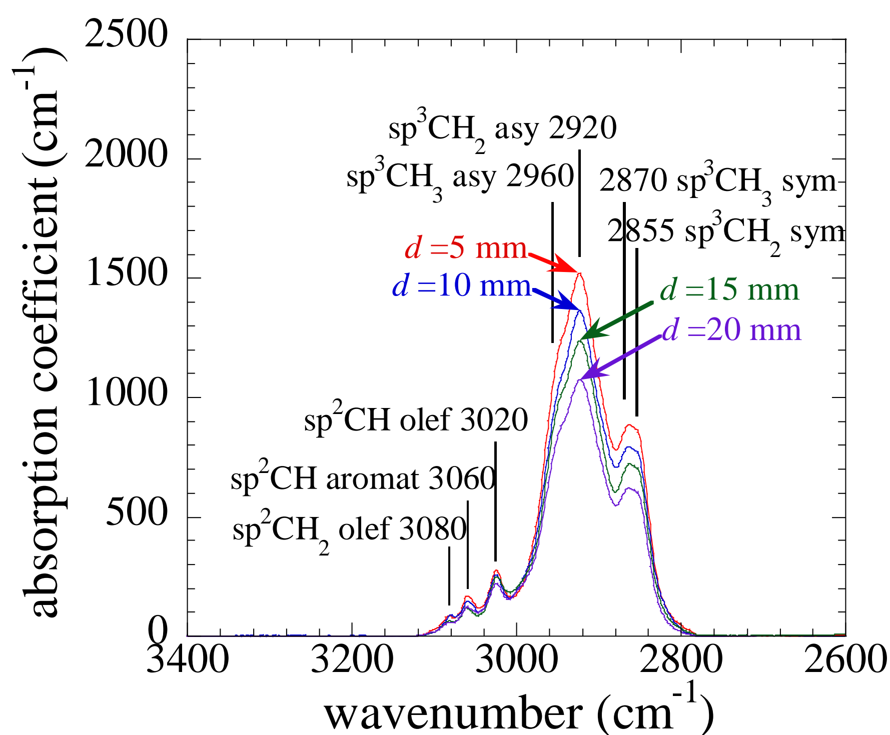

Fig. 5.5. Infrared absorption spectra of a-C:H films associated with the C–H stretching modes as a function of spatial distance from the substrate electrode at the bias voltage of -1.2 V.

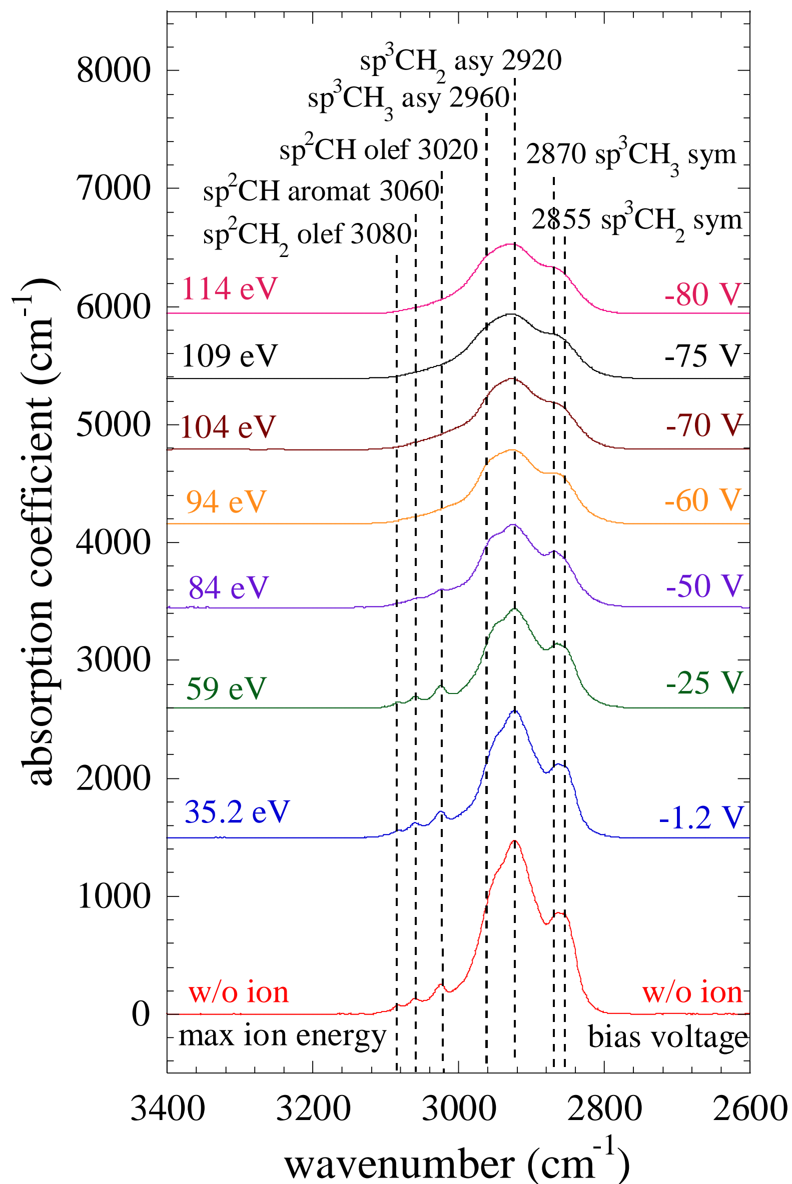

Fig. 5.6. Overview of infrared absorption spectra of a-C:H films associated with the C–H stretching modes as a function of bias voltage/max ion energy at the spatial distance of 20 mm.

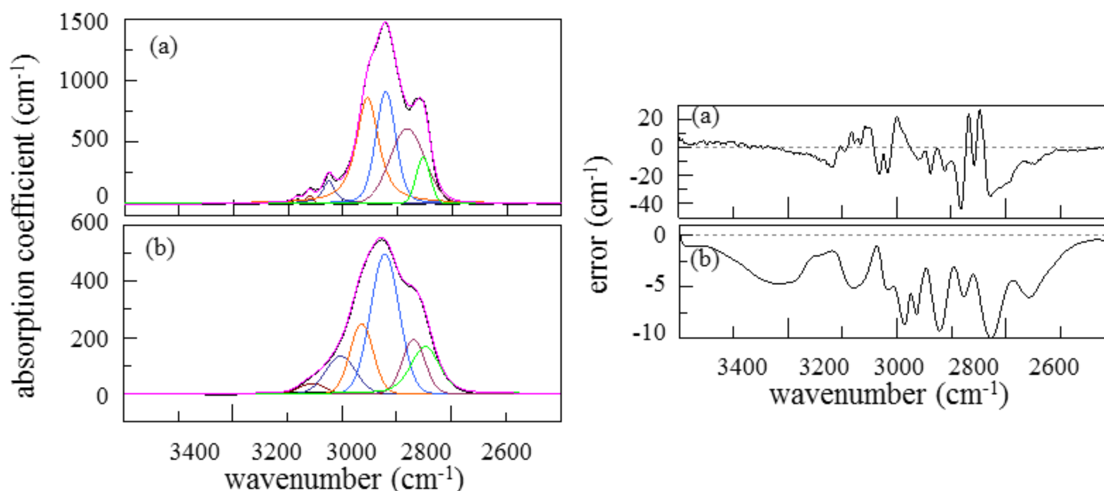

Fig. 5.7. Curve fittings with errors of stretching mode absorption bands for (a) PLCH films (without ion bombardment) and (b) DLCH films (bias voltage of -75 V) deposited at the spatial distance of 20 mm.

5.3.4 XPS C1s Spectra

Figure 5.8 shows the XPS C 1s peaks of a-C:H films deposited as a parameter of the ion energy. The spectral line shape suggests that it is composed of two components, with the component of higher binding energy become more and more significant from without ion bombardment to the ion energy of 114 eV. The fitting of the XPS C 1s peaks was performed by 100% Gaussian function [24,25], fits for a-C:H films deposited at the lowest and the highest ion energy are shown in Fig.5.9. The first component at 284.4 $\pm$ 0.1 eV corresponds to the C=C sp^2 configuration, while the second component at 285.2 $\pm$ 0.1 eV corresponds to the C–C sp^3 configuration. These binding energy values of the C=C sp^2 and C–C sp^3 configurations are consistent with the binding energies for C 1s peaks of graphite and diamond, respectively [26].

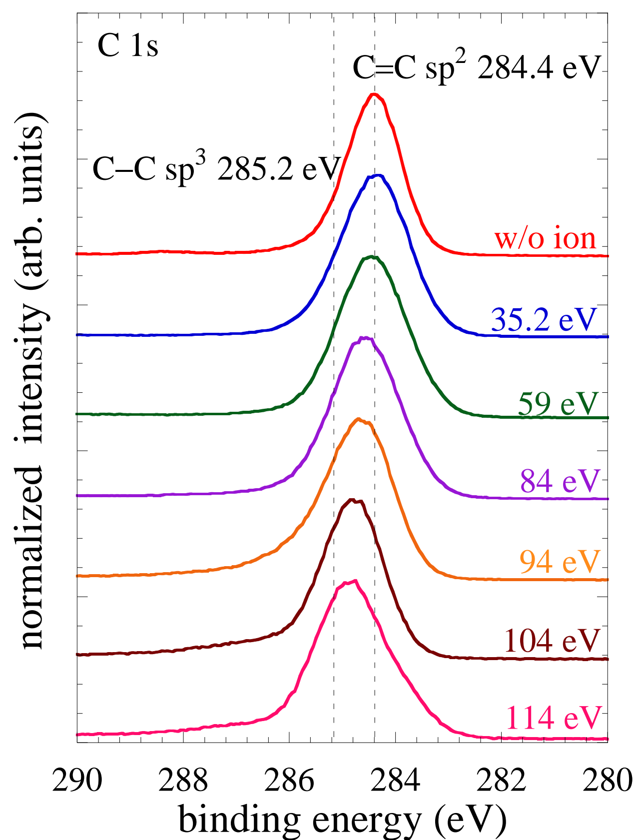

Fig. 5.8. XPS C 1s peaks of a-C:H films as a function of max ion energy.

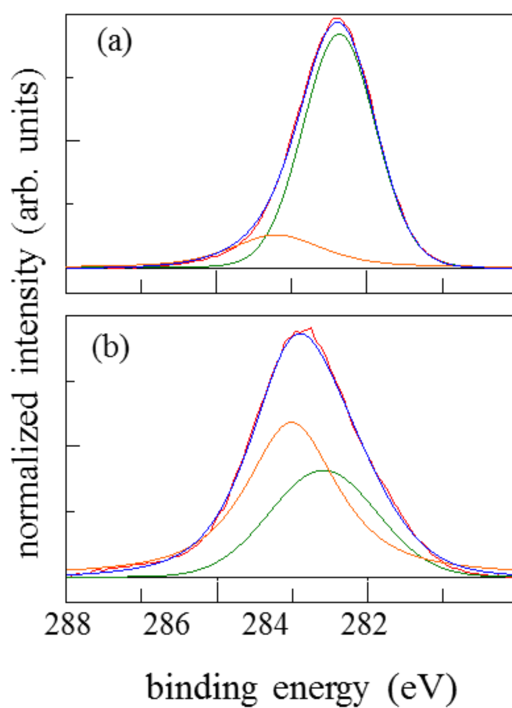

Fig. 5.9. Fits of the XPS C 1s peaks of the a-C:H films deposited (a) without ion bombardment and (b) at the ion energy of 114 eV.

5.3.5 Bonding Configurations in Films

Bonding configurations in a-C:H films are divided into carbon-carbon bonding configurations (mainly including C=C sp^2 and C–C sp^3) and carbon-hydrogen bonding configurations (mainly including C–H sp^2 and C–H sp^3) [6,27]. The C=C sp^2 and C–C sp^3 configurations were measured from C 1s peaks by XPS, and the C–H sp^2 and C–H sp^3 configurations were measured from C–H stretching modes by FTIR.

Figure 5.10 shows the relative absorption intensities without/with ion bombardment. All the intensities are nearly of the same level irrespective of the distance from the substrate electrode, which is consistent with the variation of absorption bands in Fig. 5.5. These results indicate that hydrogen bonding configurations in a-C:H films are independent of the ion flux and deposition rate, which are varied by the substrate position.

The relative absorption intensity of each configuration as a function of the ion energy is shown in Fig. 5.11. The transition from PLCH to DLCH is mainly accompanied by depletion in sp^3CH_3 asy and sp^3CH_3 sym configurations (from 35 to 16% and from 27 to 12%, respectively), and increases in sp^3CH_2 asy and sp^3CH_2 sym configurations (from 26 to 40% and from 7 to 16%, respectively). Similarly, the total intensity of sp^3 configurations decreases from 94 to 85%, whereas the total intensity of sp^2 configurations increases from 6 to 15% during the structural transition from PLCH to DLCH. These results clearly indicate that hydrogen bonding configurations in a-C:H films are determined by ion energy.

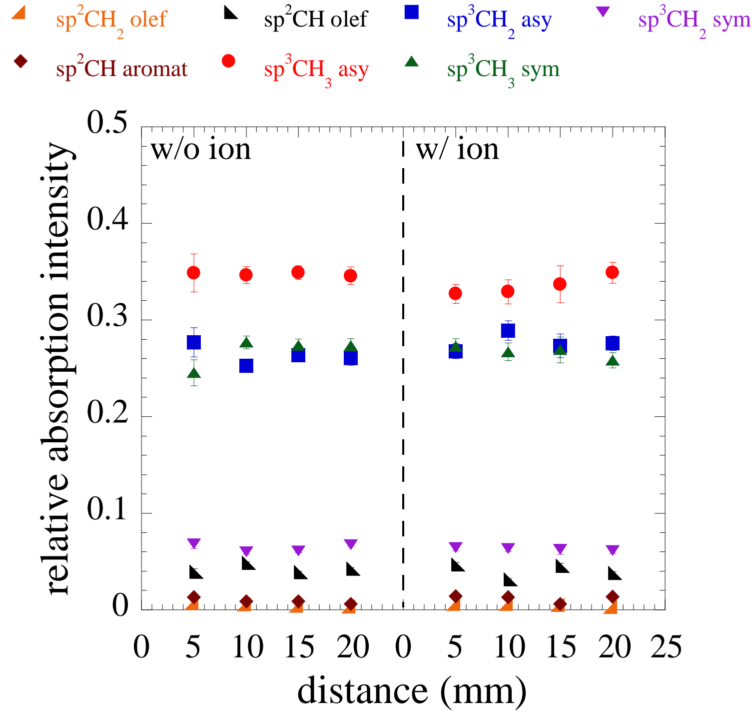

Fig. 5.10. Dependence of relative absorption intensity to C–H stretching modes on spatial distance from the substrate electrode without/with ion bombardment.

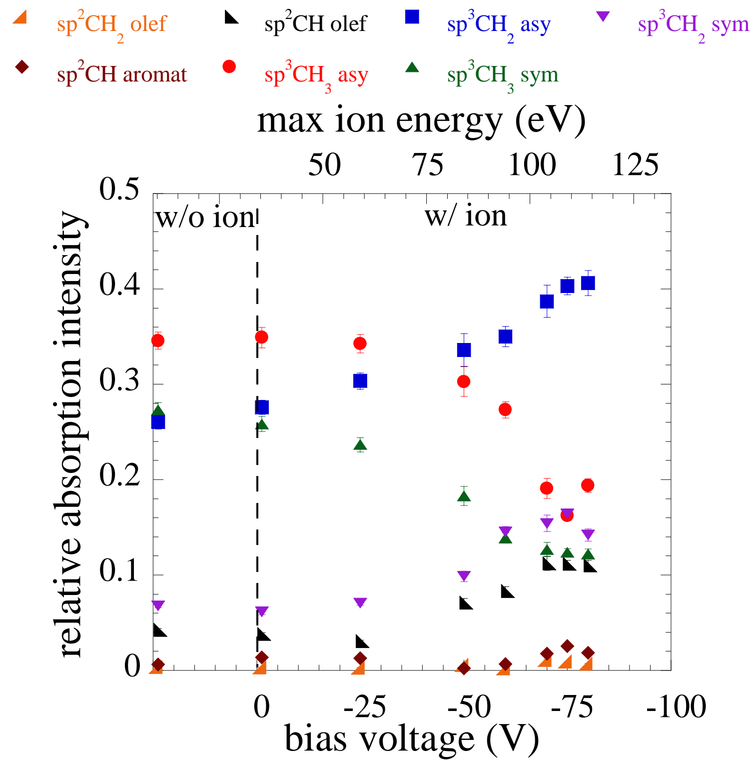

Fig. 5.11. Dependence of relative absorption intensity to C–H stretching modes on bias voltage/max ion energy at the spatial distance of 20 mm.

In Fig. 5.12(a), we can see that the C–C sp^3 to C=C sp^2 ratio remains constant with increasing the ion energy to 59 eV, whereas it increases in a linear way with further increasing the ion energy. The similar result with increasing the film mass density is shown in Fig. 5.12(b). These indicate the structure of a-C:H films begins to transform from PLCH to DLCH above the threshold ion energy of ~60 eV. Combining with film mass density and infrared absorption spectra, we consider that the films deposited from without ion bombardment to the ion energy of 84 eV are soft PLCH films, and the a-C:H films deposited in the ion energy range of 84 to 114 eV are hard DLCH films. Moreover, the mass density of PLCH films is independent on the ratio of C–C sp^3 to C=C sp^2 configurations.

Figures 5.13(a) and 5.13(b) show the variation of C–H sp^3 to C–H sp^2 ratio with increasing the ion energy/film mass density is opposite to that of C–C sp^3 to C=C sp^2 ratio. The high C–H sp^3 to C–H sp^2 ratio and low C–C sp^3 to C=C sp^2 ratio for PLCH films indicate that the majority of sp^3 configurations in such films are hydrogen-bonded. In addition, the mass density increases with decreasing C–H sp^3 to C–H sp^2 ratio regardless of PLCH or DLCH films. From Figs. 5.12 and 5.13 we can see that the mass density of PLCH films deposited at low ion energy only depends on C–H sp^3 to C–H sp^2 ratio, while the mass density of DLCH films deposited at moderate ion energy simultaneously depends on C–H sp^3 to C–H sp^2 ratio and C–C sp^3 to C=C sp^2 ratio.

Figure 5.14 shows a summary of relative area intensity of bonding configurations in a-C:H films. The harder DLCH films are obtained from the higher concentration of the C–C sp^3 configuration and the lower concentration of the C–H sp^3 configuration, which are realized by bombardment of ions above 84 eV using Ar + H_2 + C_7H_8 plasma CVD method.

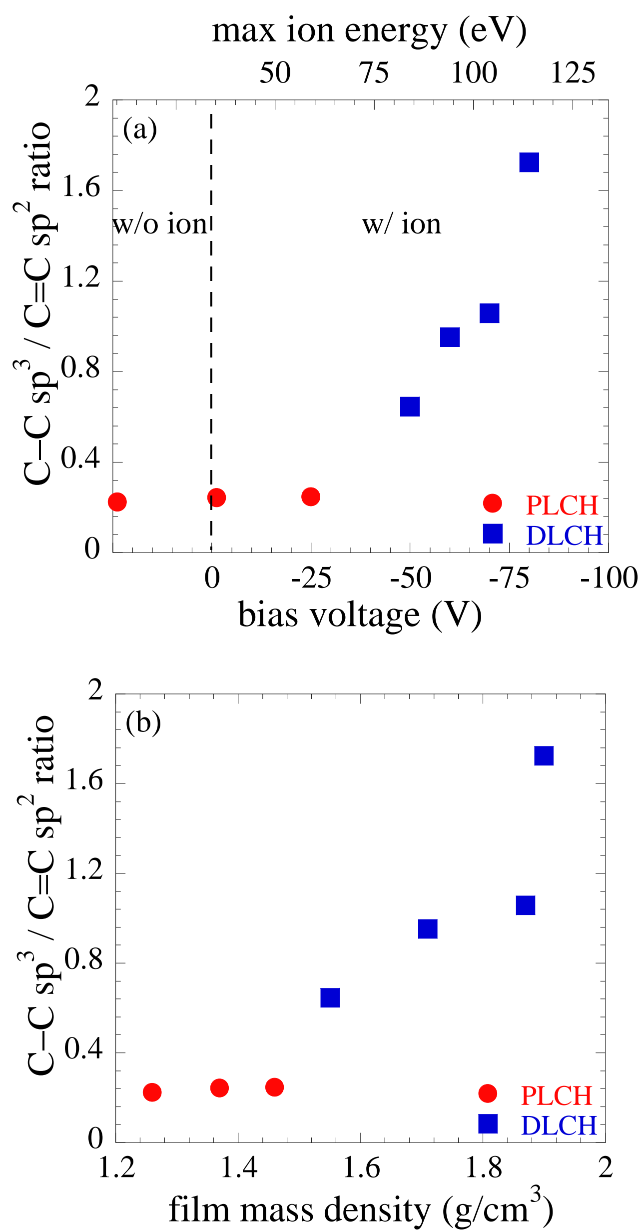

Fig. 5.12. Dependence of C–C sp^3 to C=C sp^2 ratio on (a) bias voltage/max ion energy and (b) mass density of a-C:H films.

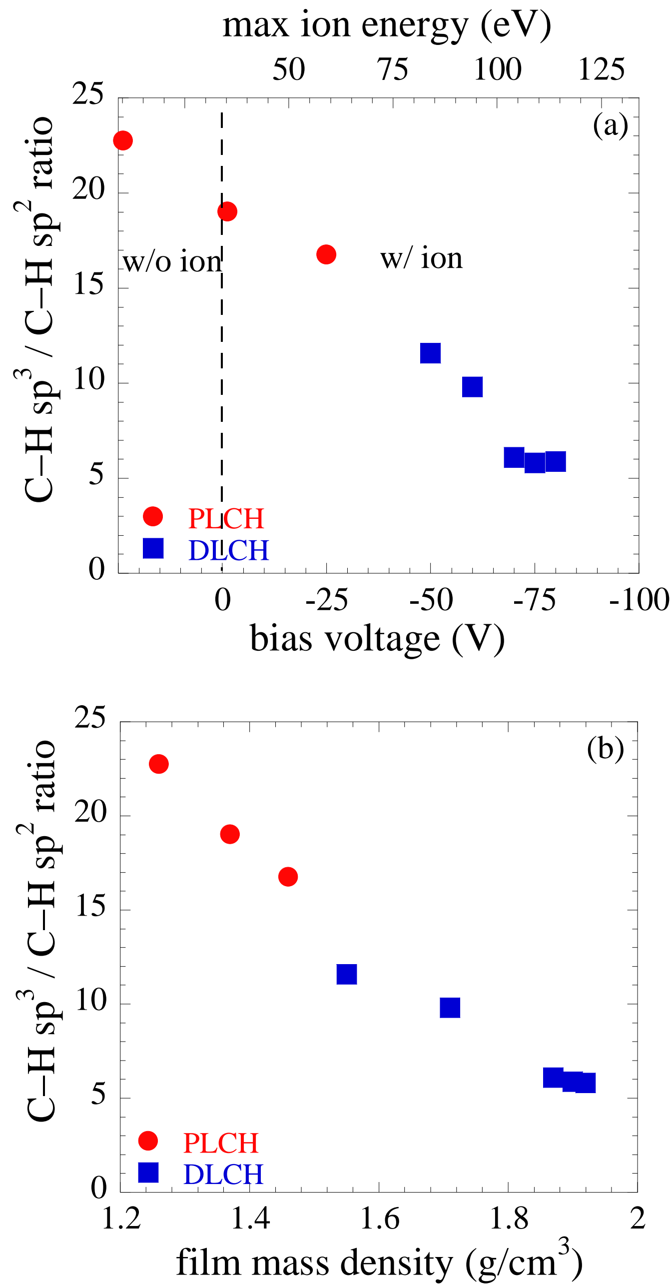

Fig. 5.13. Dependence of C–H sp^3 to C–H sp^2 ratio on (a) bias voltage/max ion energy and (b) mass density of a-C:H films.

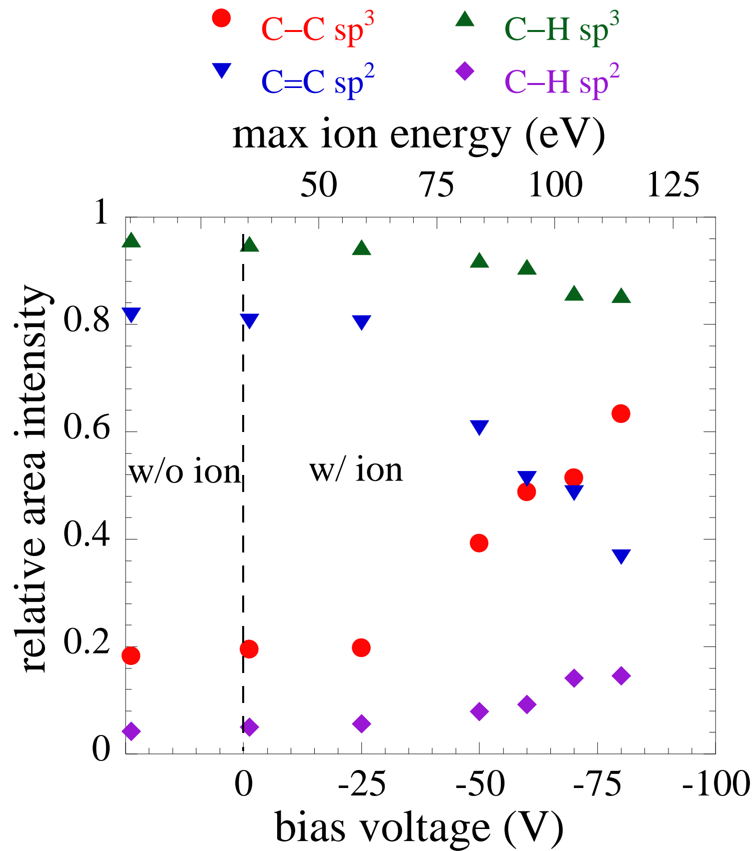

Fig. 5.14. Dependence of relative area intensity on bias voltage/max ion energy for bonding configurations in a-C:H films.

5.3.6 Hydrogen Content in Films

The hydrogen content in a-C:H films is calculated using Eq. (4.1). Here σ_i is the absorption cross section of C–H vibrations calculated from the calibration factors [28,29]. The total hydrogen content obtained by FTIR and HFS is shown in Fig. 5.15. Good agreement between the hydrogen contents obtained by FTIR and HFS is found in the PLCH region, whereas FTIR yields less hydrogen than HFS in the DLCH region. These results indicate that the absorption cross sections calculated from calibration factors can be used in the PLCH structure. For the DLCH structure, the absorption cross section becomes small owing to the solid-state effects by local field correction [30,31]. From the hydrogen content obtained by HFS, we deduced the average absorption cross sections using Eq. (4.1).

The average absorption cross section for PLCH films is 1.58×10^{-21} cm^2, which is consistent with the result of Ristein *et al* [27]. The average absorption cross section for DLCH films is 1.26×10^{-21} cm^2. To validate the average absorption cross sections, a comparison between the hydrogen content obtained by FTIR using average absorption cross sections and that obtained by HFS is shown in Fig. 5.16. The very good agreement between the hydrogen content obtained by FTIR and that obtained by HFS proves the validity of our average absorption cross sections. Hereafter, we employed the average absorption cross sections for the FTIR analysis.

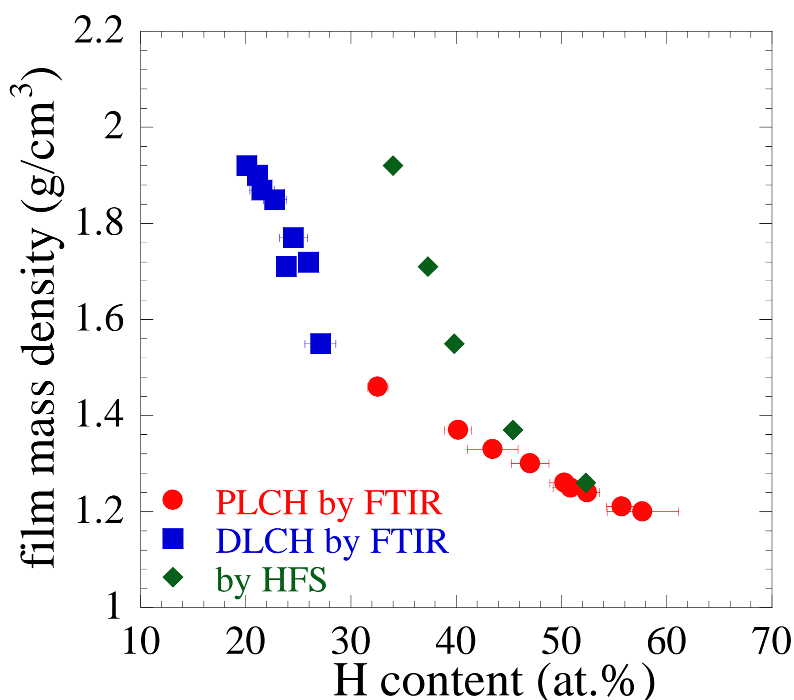

Fig. 5.15. Comparison between the hydrogen content obtained by FTIR using the absorption cross sections calculated from calibration factors and that obtained by HFS.

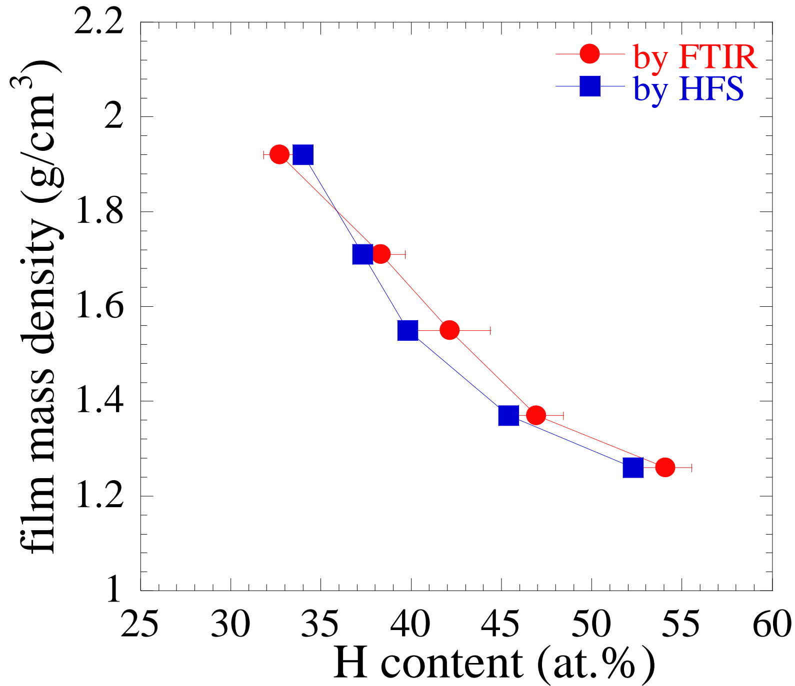

Fig. 5.16. Comparison between the hydrogen content obtained by FTIR using our average absorption cross sections and that obtained by HFS.

Figure 5.17 shows the bonded hydrogen atom density without/with ion bombardment. The hydrogen atom density decreases with increasing distance from the substrate electrode. Moreover, the hydrogen atom density without ion bombardment is higher than that with ion bombardment. From these results, it can be concluded that the hydrogen atom density depends on the ion flux and deposition rate, which are varied by the substrate position.

The ion energy dependence of the hydrogen atom density in each configuration is shown in Fig. 5.18. The hydrogen atom density in the sp^3CH_3 configuration decreases significantly with increasing ion energy, which is consistent with the variation of hydrogen bond configurations in Fig. 5.11. The hydrogen atom density in other configurations decreases in the PLCH region, whereas it increases in the DLCH region with increasing ion energy. The decrease in hydrogen atom density in the PLCH region is mainly attributed to the decrease in the intensity of absorption bands, whereas the increase in hydrogen atom density in the DLCH region is attributed to the variation of hydrogen bond configurations.

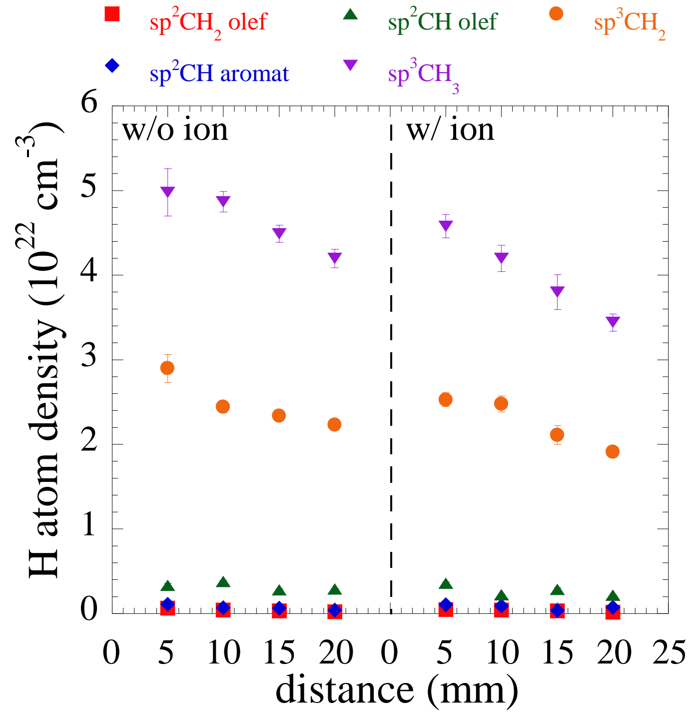

Fig. 5.17. Dependence of hydrogen atom density in respective configuration on spatial distance from the substrate electrode without/with ion bombardment.

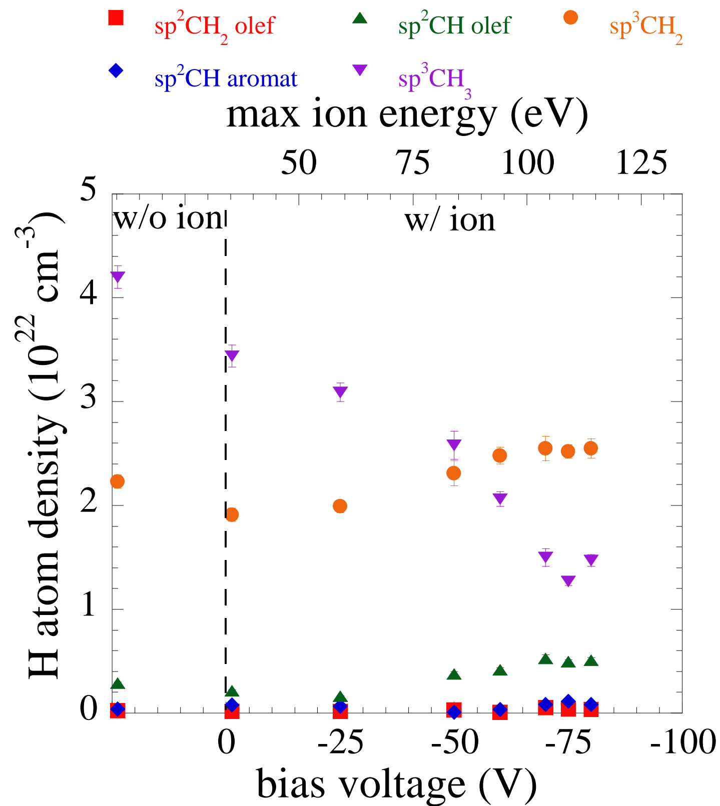

Fig. 5.18. Dependence of hydrogen atom density in respective configuration on bias voltage/max ion energy at the spatial distance of 20 mm.

Figures 5.19(a) and 5.19(b) show the total hydrogen content and H atom density in PLCH and DLCH obtained by FTIR, respectively. The mass density increases gradually with decreasing hydrogen content in the PLCH region, and it increases sharply in the DLCH region. The different tendencies for PLCH and DLCH are explained by the structural difference, namely, the concentration of the C–C sp^3 configuration. It is indicated that the mass density of PLCH films is only influenced by H content in films, while the mass density of DLCH films is simultaneously influenced by H content and the concentration of the C–C sp^3 configuration.

From these results, we conclude that the harder a-C:H films are obtained from the higher concentration of the C–C sp^3 configuration and the lower total hydrogen content, which are realized by irradiation of ions above 84 eV during plasma CVD using toluene.

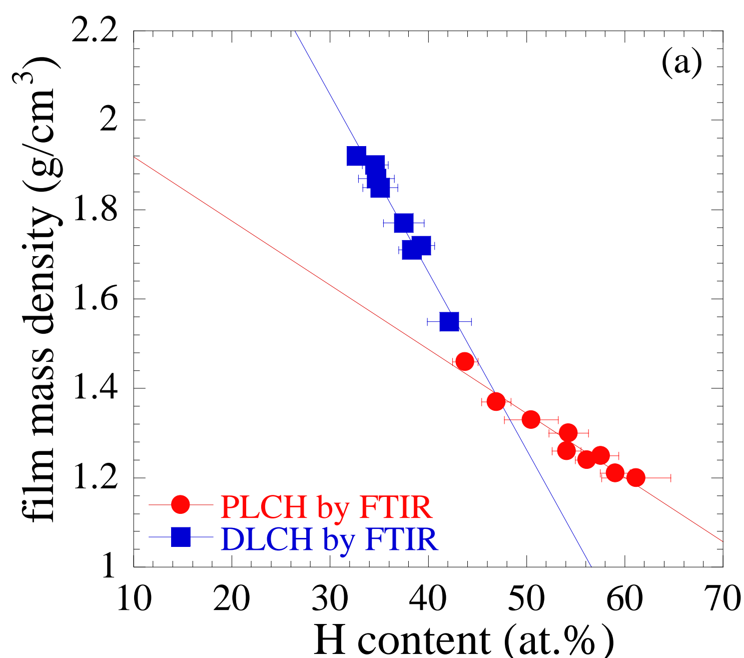

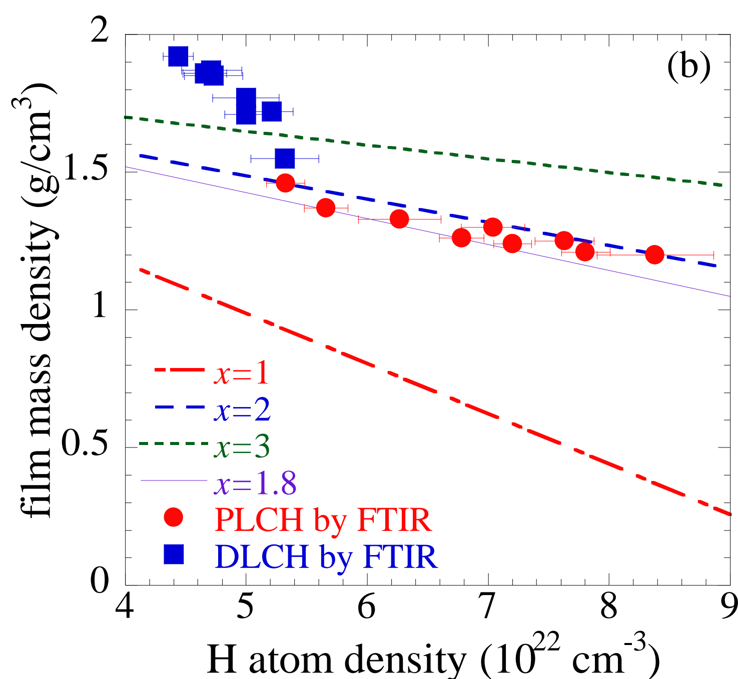

Fig. 5.19. Dependence of film mass density on (a) hydrogen content and (b) H atom density in PLCH and DLCH obtained by FTIR using our average absorption cross sections.

5.3.7 Raman Spectroscopy of Films

As a powerful and nondestructive method, Raman spectroscopy is widely used to characterize the structural quality of a-C:H films [32]. Figure 5.20 shows Raman spectra of a-C:H films deposited as a parameter of ion energy, the peak maximum at 1560 cm^{-1} is identified as a characteristic of DLCH [33]. Owing to the sp^2 cluster size is small and disordered vibration modes cannot be set up, no Raman signal is exhibited for a-C:H films deposited without ion bombardment. Raman spectrum of a-C:H films deposited at 35.2 eV is masked by strong photoluminescence (PL) background (defined as the ratio between the slope m of the spectra calculated between 1050 and 1800 cm^{-1}, and the intensity of the G-peak measured in microns, m/I_G), suggesting the formation of a polymerized structure with high hydrogen content (≧45 at.%) [34,35]. Thus, only the results of films deposited greater than 35.2 eV were employed hereafter. Figure 5.21 shows a typical Raman

spectrum with PL background of a-C:H films. The D-peak and G-peak positions were determined by Gaussian curve fits in the region from 1000 to 1950 cm^{-1} to the Raman spectrum. The D-peak (centered approximately 1350 cm^{-1}) is due to the breathing modes of sp^2 atoms in rings, the G-peak (centered approximately 1550 cm^{-1}) is due to the bond stretching of all pairs of sp^2 atoms in both rings and chains [36]. Thus, the intensity (i.e., the height) ratio of the D-peak and G-peak, I_D/I_G, is a measure of the amount of ring-like sp^2 clusters in a-C:H films as shown in Fig. 5.22. The ratio increases with increasing the ion energy, which means increases in ring-like sp^2 clusters.

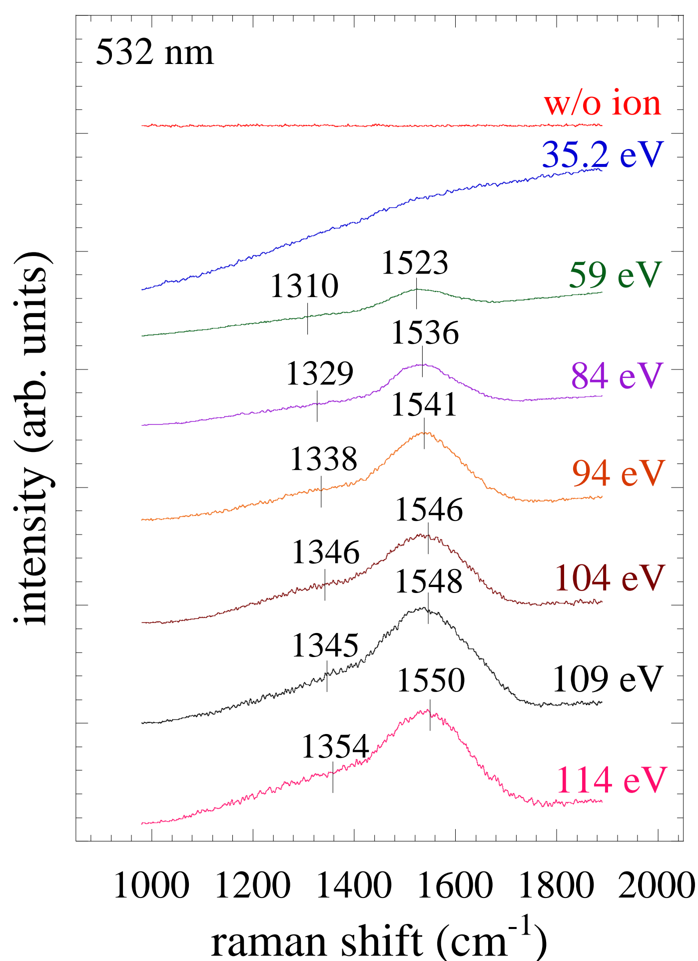

Fig. 5.20. Raman spectra of a-C:H films as a function of max ion energy.

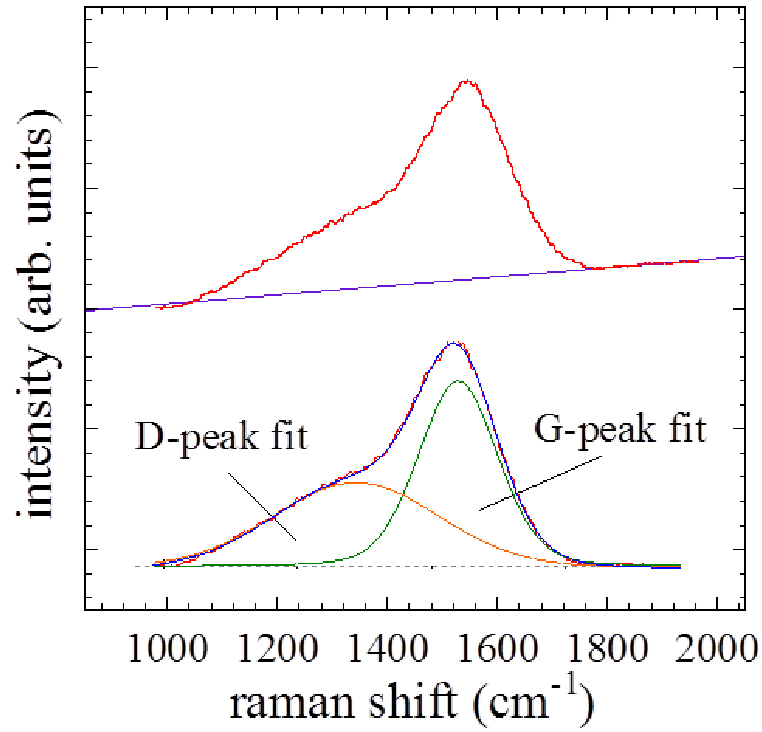

Fig. 5.21. Raman spectrum of a-C:H films deposited at the ion energy of 114 eV with PL background. The G-peak and D-peak are determined by Gaussian curve fits.

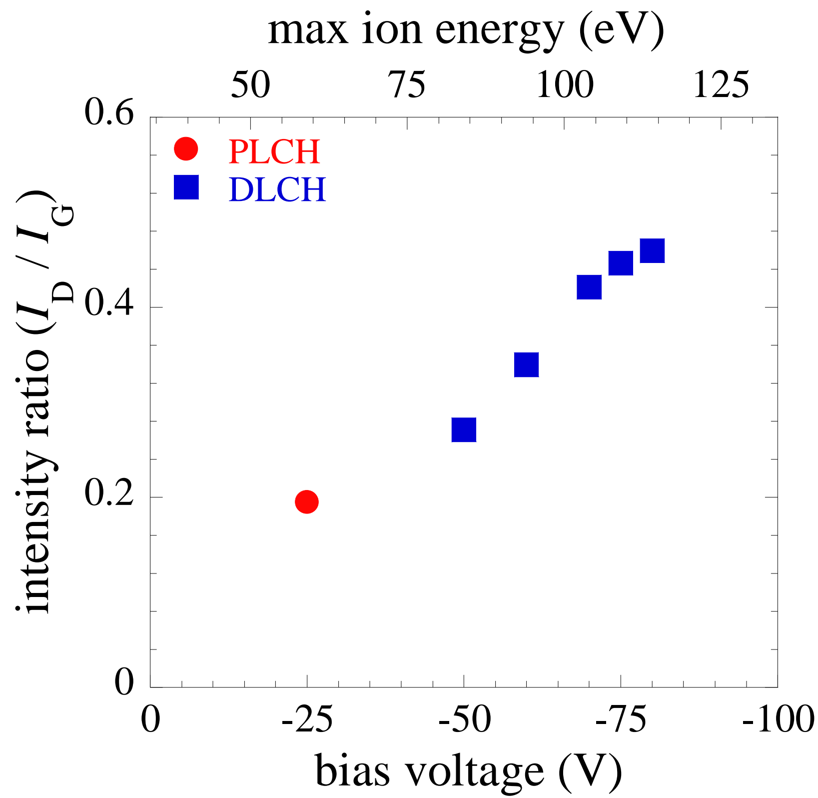

Fig. 5.22. Dependence of I_D/I_G ratio on bias voltage/max ion energy.

Owing to the hydrogen saturation of nonradiative recombination centers, the PL background increases for higher H content, which as a typical feature of hydrogenated samples in visible Raman spectra. Thus, we can use the PL background, m/I_G, to qualitatively assess the H content in films according to [35,37]

$$\text{H [at.\%]} = 21.7 + 16.6\log\left\{\frac{m}{I_G}[\mu m]\right\} \quad (5.1)$$

Figure 5.23 shows the ion energy dependence of H content obtained from PL background. To validate the results, H content was also measured by FTIR and HFS. H content obtained by each method decreases in a linear way with increasing the ion energy. There are certain errors between Raman spectroscopy and other methods, especially for sample deposited at high ion energy. In view of the complexity of FTIR and HFS and the acceptable errors (≦ 5%), Raman spectroscopy is considered to be a fast and an effective way to obtained H content in a-C:H films deposited with an ion energy greater than 35.2 eV.

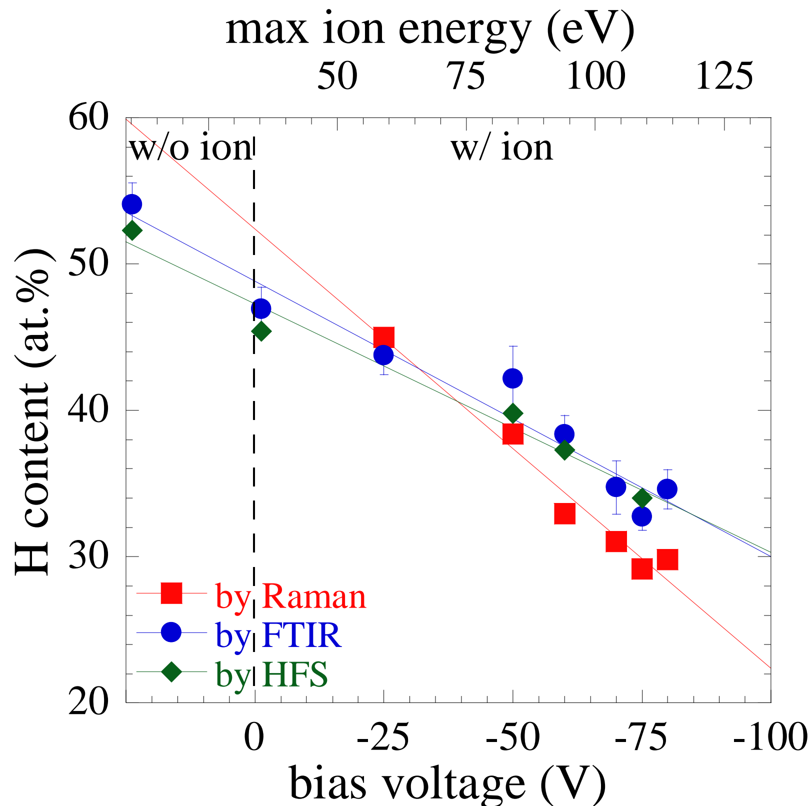

Fig. 5.23 Dependence of H content on bias voltage/max ion energy obtained by Raman spectroscopy, FTIR and HFS.

The full width at half maximum of the G peak, $FWHM_G$, is mainly influenced by structural disorder (bond angle and bond length distortions) [38]. $FWHM_G$ increases with increasing the C–C sp^3 content as shown in Fig. 5.24(a). This is because $FWHM_G$ increases as disorder increases, the increase of disorder is linked to higher C–C sp^3 content. On the other hand, $FWHM_G$ decreases with increasing the H content in a-C:H films as shown in Fig. 5.24(b). These features allow us to identify $FWHM_G$ as a measure of film mass density which depends mainly on hydrogen content and the concentration of the C–C sp^3 configuration. Figure 5.25 shows the variation of $FWHM_G$ is well coincidence with that of film mass density and described by

$$\rho = -0.115 + 0.011\overline{W_G} \tag{5.2}$$

where ρ is the film mass density, $\overline{W_G}$ is the $FWHM_G$. Therefore, the measure of mass density using $FWHM_G$ is reliable for our a-C:H films.

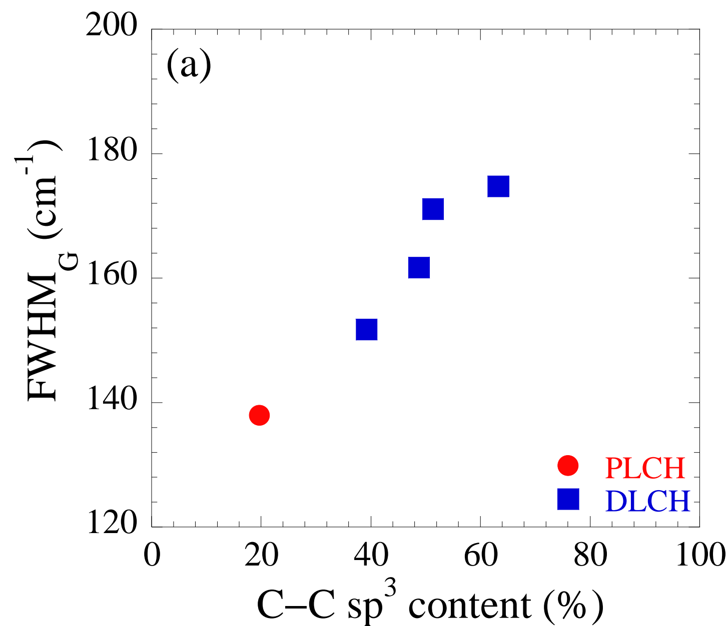

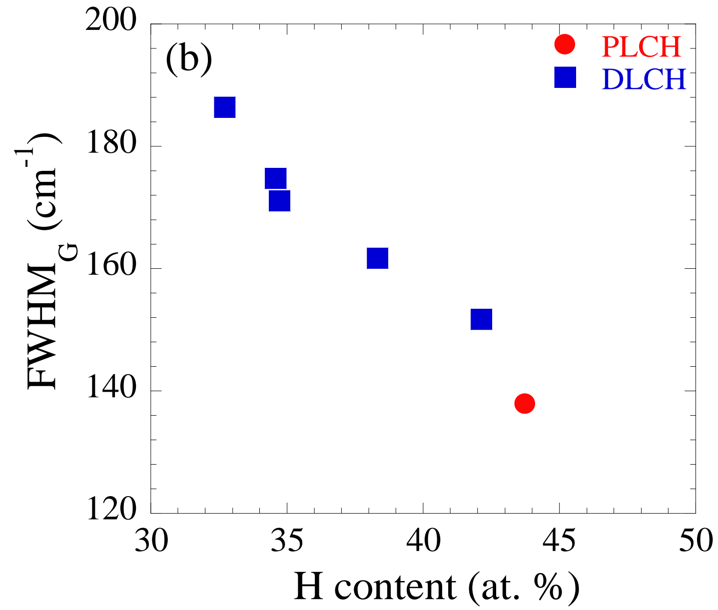

Fig. 5.24 Dependence of $FWHM_G$ on (a) C–C sp^3 content and (b) H content in a-C:H films. H content is measured by FTIR.

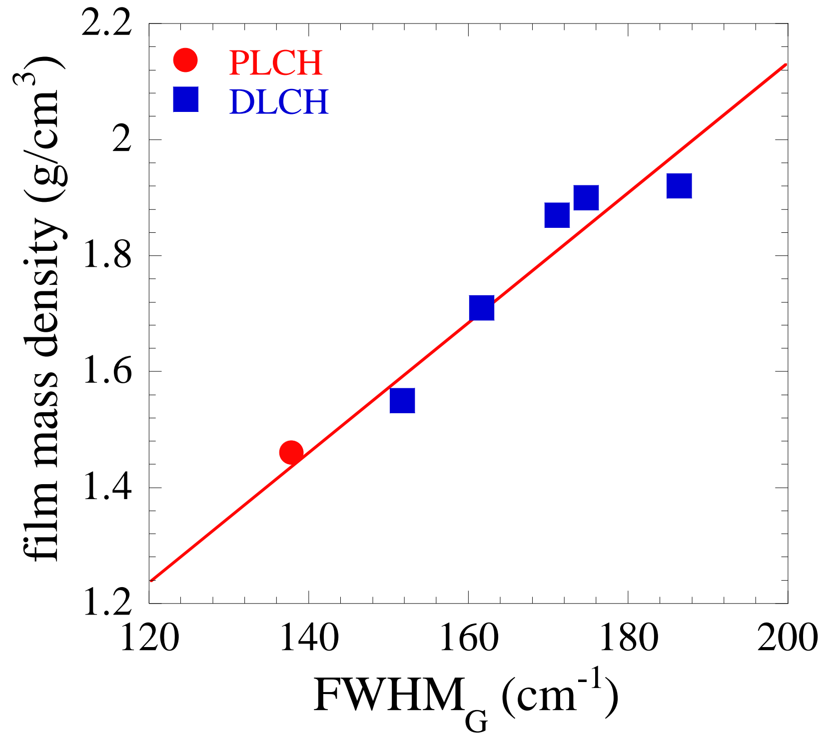

Fig. 5.25 Dependence of mass density on $FWHM_G$ for a-C:H films. The solid line is a regression fit to the data.

Raman spectroscopy is used for characterization of a-C:H films in distinguish the structure of films, qualitative assessment of the H content in films, and identify the mass density of films. By Raman spectroscopy, we can greatly simplify the analysis procedures for deposited a-C:H films.

5.4 Summary

We investigated deposition mechanism of a-C:H films by carrying out experiments on effects of ion flux and ion energy, and characterized the deposited films by FTIR, HFS, XPS, and Raman spectroscopy. The following conclusions are obtained in this study.

(1) The deposition rate and mass density increase with increasing distance from the substrate electrode to 20 mm. The highest mass density of 1.92 g/cm^3 with the deposition rate of 43.4 nm/min is obtained at 20 mm for the ion energy of 109 eV.

(2) The hydrogen bonding configurations in a-C:H films are closely related to the ion energy, whereas they are less dependent on ion flux and deposition rate.

(3) The mass density of PLCH films deposited from without ion bombardment to the ion energy of 84 eV only depends on C–H sp^3 to C–H sp^2 ratio (H content) in films.

(4) The mass density of DLCH films deposited in the ion energy range of 84 to 114 eV simultaneously depends on C–H sp^3 to C–H sp^2 ratio (H content) and C–C sp^3 to C=C sp^2 ratio in films.

(5) The mass density increases gradually with decreasing hydrogen content in the PLCH region, and it increases sharply with decreasing hydrogen content in the DLCH region. This difference is due to the different C–C sp^3 concentrations in PLCH and DLCH films.

(6) The characterization in film structure, H content, and mass density of our deposited a-C:H films can be greatly simplified using Raman spectroscopy.

References:

[1] J. Robertson, Phys. Status Solidi A **205**, 2233 (2008).

[2] Y. Y. Cheng, W. L. Cheung, and T. W. Chow, J. Prosthetic Dent. **103**, 309 (2010).

[3] T. Y. Leung, W. F. Man, P. K. Lim, W. C. Chan, F. Gaspari, and S. Zukotynski, J. Non-Cryst. Solids **254**, 156 (1999).

[4] N. M. J. Conway, A. C. Ferrari, A. J. Flewitt, J. Robertson, W. I. Milne, A. Tagliaferro, and W. Beyer, Diamond Rel. Mater. **9**, 765 (2000).

[5] Q. Zhang, S. F. Yoon, A. Rusli, J. Ahn, H. Yang, and D. Bahr, J. Appl. Phys. **84**, 5538 (1998).

[6] J. Robertson, Mater. Sci. Eng. R **37**,129 (2002).

[7] V. I. Merkulov, D. H. Lowndes, G. E. Jellison, A. A. Puretzky, D. B. Geohegan, Appl. Phys. Lett. **73**, 2591 (1998).

[8] Y. Lifshitz, S. R. Kasi, J. W. Rabalais, and W. Eckstein, Phys. Rev. B **41**, 10468 (1990).

[9] Y. Lifshitz, Diamond Rel. Mater. **8**, 1659 (1999).

[10] G. Adamopoulos, J. Robertson, N. A. Morrison, and C. Godet, J. Appl. Phys. **96**, 6348 (2004).

[11] A. N. Obraztsov, E. A. Obraztsova, A. V. Tyurnina, and A. A. Zolotukhin, Carbon **45**, 2017 (2007).

[12] T. Nomura, K. Koga, M. Shiratani, Y. Setsuhara, M. Sekine, and M. Hori, MRS Proc. **1222**, 203 (2009).

[13] N. Mutsukura, S. Inoue, and Y. Machi, J. Appl. Phys. **72**, 43 (1992).

[14] K. Takenaka, K. Koga, M. Shiratani, Y. Watanabe, and T. Shingen, Thin Solid Films **506–507**, 197 (2006).

[15] J. W. Zou, K. Schmidt, K. Reichelt, and B. Dischler, J. Appl. Phys. **67**, 487 (1990).

[16] J. Joo, Y. C. Quan, and D. Jung, J. Mater. Res. **15**, 228 (2000).

[17] Y. P. Song, D. Field, and D. F. Klemperer, J. Phys. D **23**, 673 (1990).

[18] A. M. Daltrini, S. A. Moshkalev, M. J. R. Monteiro, E. Besseler, A. Kostryukov, and M. Machida, J. Appl. Phys. **101**, 073309 (2007).

[19] A. Devdariani, E. Chesnokov, A. Zagrebin, M. G. Lednev, I. D. Petsalakis, G. Theodorakopoulos, H. -P. Liebermann, and R. J. Buenker, Chem. Phys. **330**, 101 (2006).

[20] P. B. Nagabalasubramanian, S. Periandy, S. Mohan, and M. Govindarajan, Spectrochim. Acta, Part A **73**, 77 (2009).

[21] X. B. Yan, T. Xu, S. R. Yang, H. W. Liu, and Q. J. Xue, J. Phys. D **37**, 2416 (2004).

[22] X. M. He, K. C. Walter, M. Nastasi, S.-T. Lee, and X. S. Sun, Thin Solid Films **355-356**, 167 (1999).

[23] S. F. Yoon, H. Yang, A. Rusli, J. Ahn, and Q. Zhang, J. Electron. Mater. **27**, 46 (1998).

[24] J. Filik, P. W. May, S. R. J. Pearce, R. K. Wild, and K. R. Hallam, Diamond Rel. Mater. **12**, 974 (2003).

[25] F. C. Tai, S. C. Lee, C. H. Wei, and S. L. Tyan, Mater. Trans. **47**, 1847 (2006).

[26] P. Mérel, M. Tabbal, M. Chaker, S. Moisa, and J. Margot, Appl. Surf. Sci. **136**, 105 (1998).

[27] J. Ristein, R. T. Stief, L. Ley, and W. Beyer, J. Appl. Phys. **84**, 3836 (1998).

[28] A. S. Wexler, Spectrochim. Acta **21**, 1725 (1965).

[29] A. S. Wexler, Appl. Spectrosc. Rev. **1**, 29 (1967).

[30] A. Rahmani, P. C. Chaumet, and G. W. Bryant, Astrophys. J. **607**, 873 (2004).

[31] D. E. McCumber, Phys. Rev. **136**, A954 (1964).

[32] S. M. Huang, Z. Sun, Y. F. Lu, and M. H. Hong, Surf. Coatings Technol. **151-152**, 263 (2002).

[33] M. Yoshikawa, Mater. Sci. Forum **52-53**, 365 (1991).

[34] B. Marchon, J. Gui, K. Grannen, and G. C. Rauch, IEEE Trans. Magn. **33**, 3148

(1997).

[35] C. Casiraghi, F. Piazza, A. C. Ferrari, D. Grambole, and J. Robertson, Diamond Rel. Mater. **14**, 1098 (2005).

[36] M. Yoshikawa, G. Katagiri, H. Ishida, A. Ishitani, and T. Akamatsu, J. Appl. Phys. **64**, 6464 (1988).

[37] C. Casiraghi, A. C. Ferrari, and J. Robertson, Phys. Rev. B **72**, 085401 (2005).

[38] M. A. Tamor and W. C. Vassell, J. Appl. Phys. **76**, 3823 (1994).

Chapter 6 Deposition of a-C:H Films on PMMA

6.1 Introduction

Multigate devices, which incorporate more than one gate, have received increasing attention in COMS-based semiconductor industry to create ever-smaller microprocessors and memory cells [1,2]. The primary roadblock in implementation of multigate devices is manufacturability using extreme ultraviolet (EUV) lithography, especially with respect to sub-14 nm patterning [3,4].

Owing to the stringent requirement to simultaneously achieve multiple and often opposed characteristics such as high sensitivity, high resolution, and low line edge roughness in photoresists, EUV lithography process has been limited in 14 nm line and space [5]. Moreover, the shallow DOF of EUV lithography requires thin photoresist films, which leads to worse plasma etch resistance of them. Deposition of a-C:H flims on the surface of nano-patterned photoresists as protective coatings is expected to overcome this limitation and improve the etch resistance.

Thus far, we have succeeded in controlling deposition profiles of copper films on trench substrates [6,7]. Then the methods of controlling deposition profiles have been applied in depositing a-C:H films on trench substrates at a low substrate temperature of 100℃, and realized conformal, subconformal and anisotropic deposition profiles [8,9]. Such deposition profile control opens possibility of selective coatings on top of nano-patterned structures. Here, we report experimental results of deposition of a-C:H films on photoresists such as PMMA by using the H-assisted plasma CVD method.

6.2 Experimental Details

We deposited a-C:H films on PMMA using the H-assisted plasma CVD reactor as

shown in Fig. 2.1. Excitation frequency of main discharge was 28 MHz and the supplied power voltage was 220 V. Excitation frequency of H atom source discharge was 13.56 MHz and the supplied power was 500 W. The self-biased RF discharge was not applied and the bias voltage was -7 V (floating). Toluene, Ar and H_2 were supplied at flow rates of 5, 60, and 30 sccm, respectively. The total pressure was 0.1 Torr. a-C:H film deposition was carried out on PMMA coated Si substrate. The substrate temperature was 100℃. To prevent PMMA from being etched and carbonized, a stainless steel cover plate was placed 5 mm above the substrate to block irradiation of photons and ions to PMMA as shown in Fig. 6.1. Carbon-containing neutral radicals and H atoms can pass though the plate to reach the substrate.

Thicknesses of PMMA and a-C:H films on Si substrate were measured with a scanning electron microscope (SEM: JEOL, JIB-4600F). Electronic states of PMMA and a-C:H films were measured in SPring-8 by BL46XU hard X-ray photoemission spectroscopy (HAXPES), where 8 keV hard X-ray was used as the excitation source, and probing depth was controlled by changing the detection angle of photoelectrons to the sample surface. As anti-static coatings, platinum (Pt) was deposited 3 nm on the surface of samples in advance, and peak shift correction for each spectrum was carried out on the basis of 71 eV which is the binding energy of Pt $4f_{7/2}$.

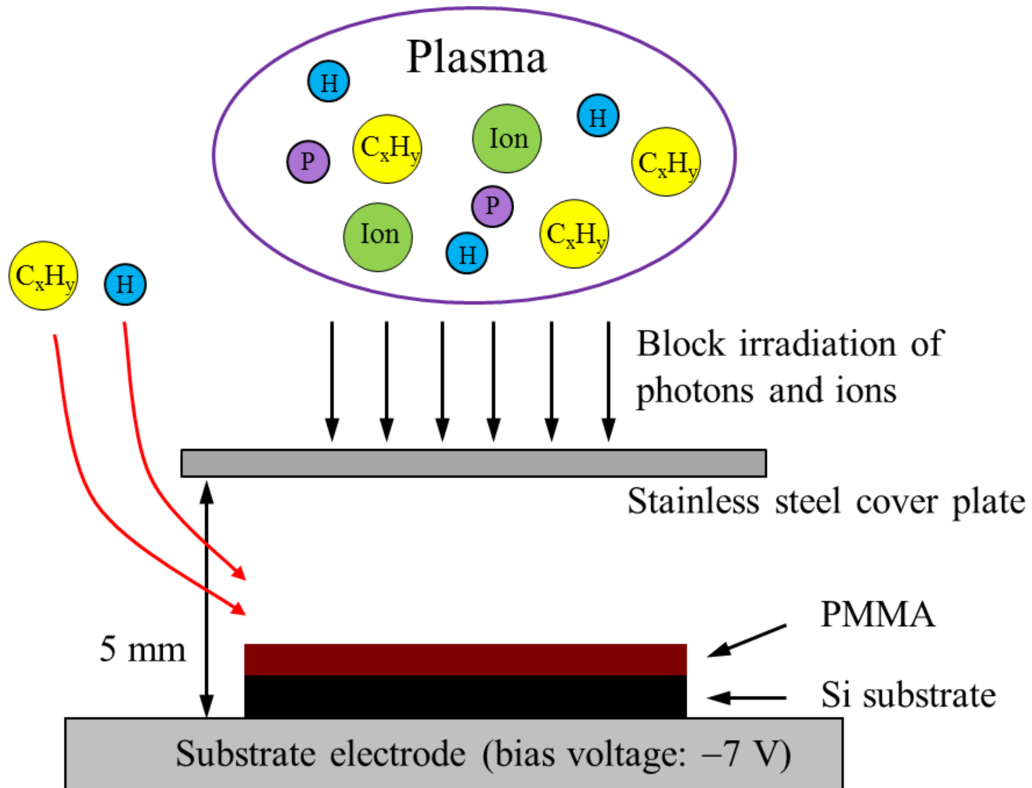

Fig. 6.1. Schematic of measurement of block irradiation of photons and ions.

6.3 Results and Discussion

Figure 6.2 shows cross-section SEM images before and after a-C:H film deposition, from which a two-layer structure on Si substrate is clearly observed. The thicknesses of the upper layer and the lower layer are 31 nm and 253 nm, respectively.

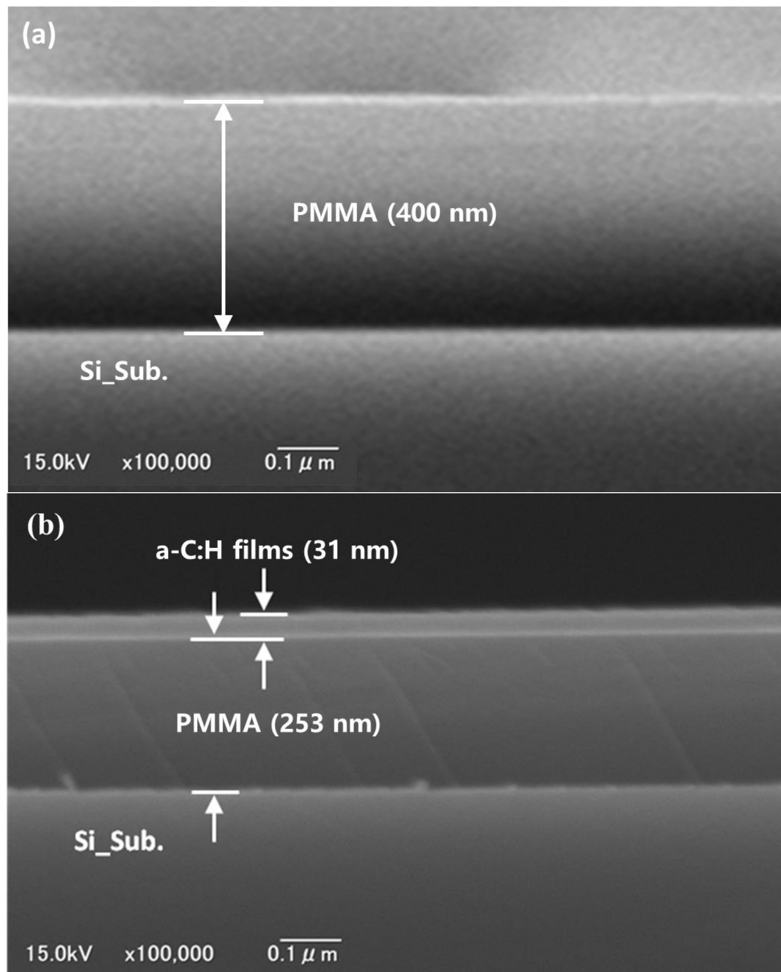

Fig. 6.2. Cross-section SEM images of PMMA (a) before a-C:H film deposition and (b) after a-C:H film deposition.

HAXPES measurements were carried out to obtain information on chemical bonds in films. Figure 6.3 shows normalized C 1s spectra of the deposited films at a detection angle of 80°. These spectra provide information of chemical bonds in the region around 50 nm in depth from the top of the films. The chemical structure of PMMA is shown in Fig. 6.4 [10,11]. The peaks associated with carbon-oxygen bonds and carbon-carbon bond in Fig. 6.3(a) are almost the same as the peaks in Fig. 6.3(b). The results of peak separation are summarized in Table V. Although all of peak positions in PMMA after deposition are 0.6~0.8 eV higher than those before deposition, spacings between peak positions in PMMA before and after deposition are nearly same. These results indicate that the lower layer of the films is PMMA.

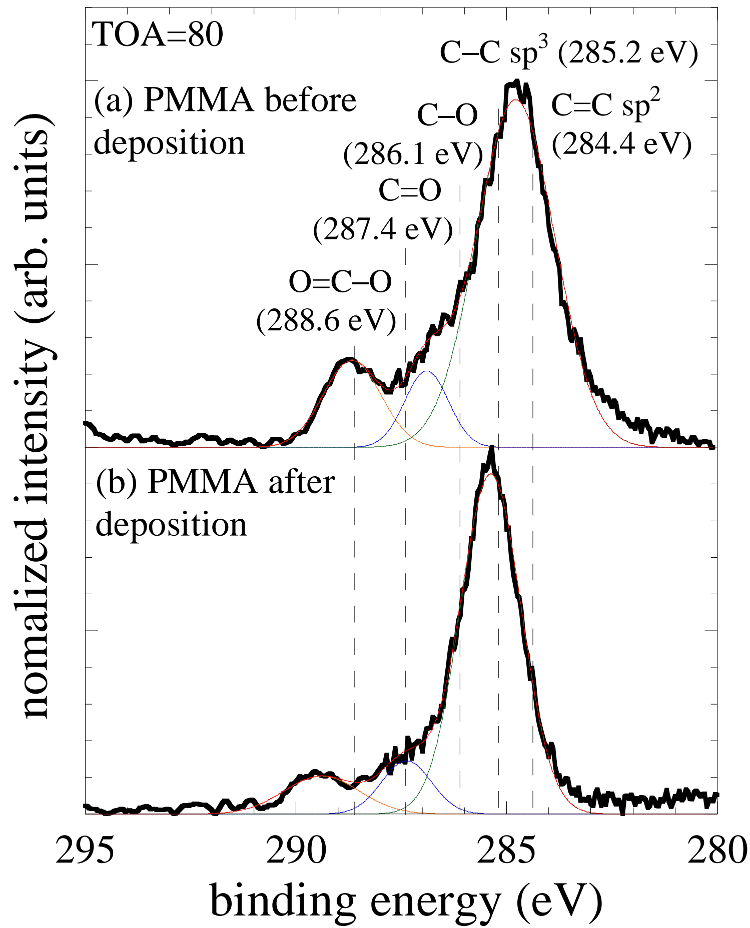

Fig. 6.3. Normalized C 1s spectra of (a) PMMA before deposition and (b) PMMA after deposition at a detection angle of 80°.

Table V. The peak separation results of PMMA before and after deposition.

	Peak	Int.	FWHM	Area	%Area
PMMA before deposition	284.69	0.94855	2.1871	2.20832	76.46
	286.80	0.20894	1.22288	0.27198	9.42
	288.57	0.23741	1.61386	0.40785	14.12
	Peak	Int.	FWHM	Area	%Area
PMMA after deposition	285.38	0.92768	1.69985	1.67858	79.03
	287.38	0.1454	1.38232	0.21395	10.07
	289.39	0.10367	2.09729	0.23144	10.90

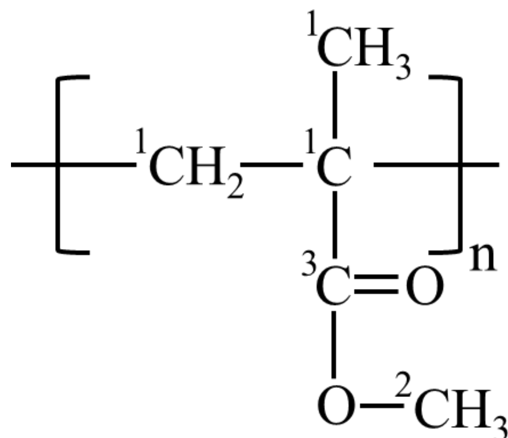

Fig. 6.4. The chemical structure of PMMA. The peak at 285.2 eV corresponds to ^{1}C–C, the peak at 286.1 eV corresponds to ^{2}C–O, and the peak at 288.6 eV corresponds to O=^{3}C–O.

Figure 6.5 shows HAXPES results at a detection angle of 20° which provides information on chemical bonds near the surface of films. The spectrum shape in 287−290 eV region which corresponds to carbon-oxygen bonds in Fig. 6.5(b) is different from that in Fig. 6.5(a). The results of peak separation are listed in Table VI. The peak area ratio of carbon-carbon bond (≈285 eV) in a-C:H films is more dominant than in PMMA before deposition, whereas the peak area ratio of carbon-oxygen bond (≈289 eV) in PMMA before deposition is 7 times as large as that in a-C:H films.

Figure 6.6 shows the spectra normalized by Pt peak of (a) C 1s and (b) O 1s at a detection angle of 20°. Since Pt was deposited on the surface of two samples simultaneously, spectral intensity varies according to the ratios of chemical bonds in the measurement area. From Fig. 6.6 we can see that the peak areas of O 1s in both films are nearly the same, whereas the peak area of C 1s in a-C:H films is larger than PMMA before deposition. These results indicate that the upper layer is a-C:H instead of carbonized PMMA.

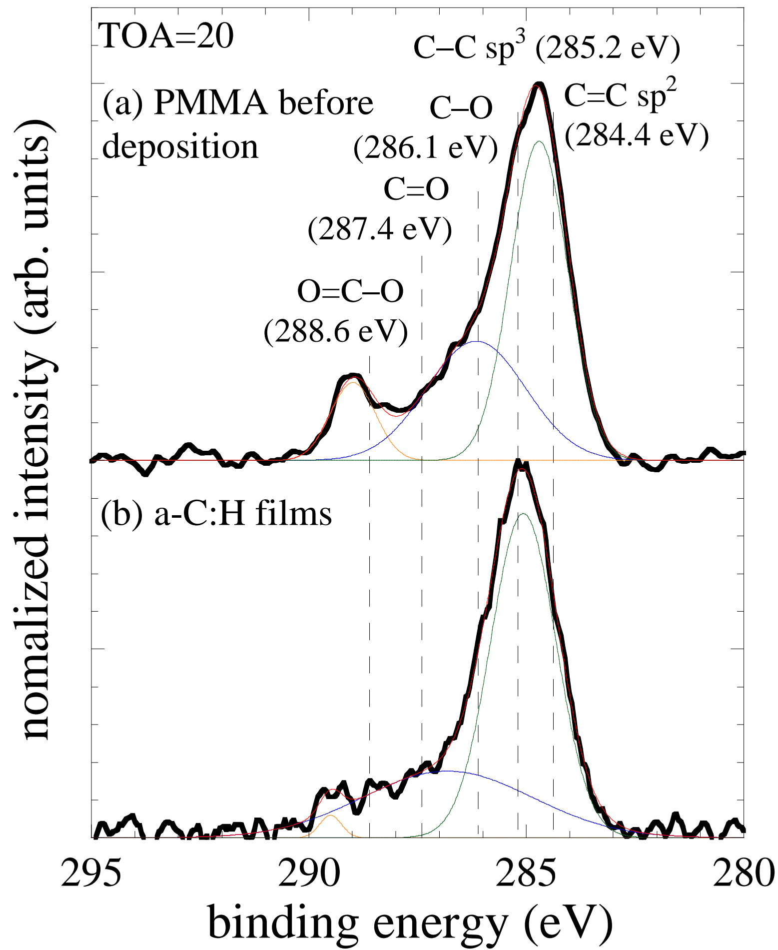

Fig. 6.5. Normalized C 1s spectra of (a) PMMA before deposition and (b) a-C:H films at a detection angle of 20°.

Table VI. The peak separation results of PMMA before deposition and a-C:H films.

	Peak	Int.	FWHM	Area	% Area
PMMA before deposition	284.71	0.84655	1.53931	1.3871	54.26
	286.15	0.3166	2.67348	0.901	35.25
	288.99	0.20696	1.217	0.26811	10.49
	Peak	Int.	FWHM	Area	% Area
a-C:H films	285.07	0.85938	1.76933	1.61855	64.23
	286.81	0.17679	4.59083	0.86395	34.29
	289.50	0.05972	0.58742	0.03734	1.48

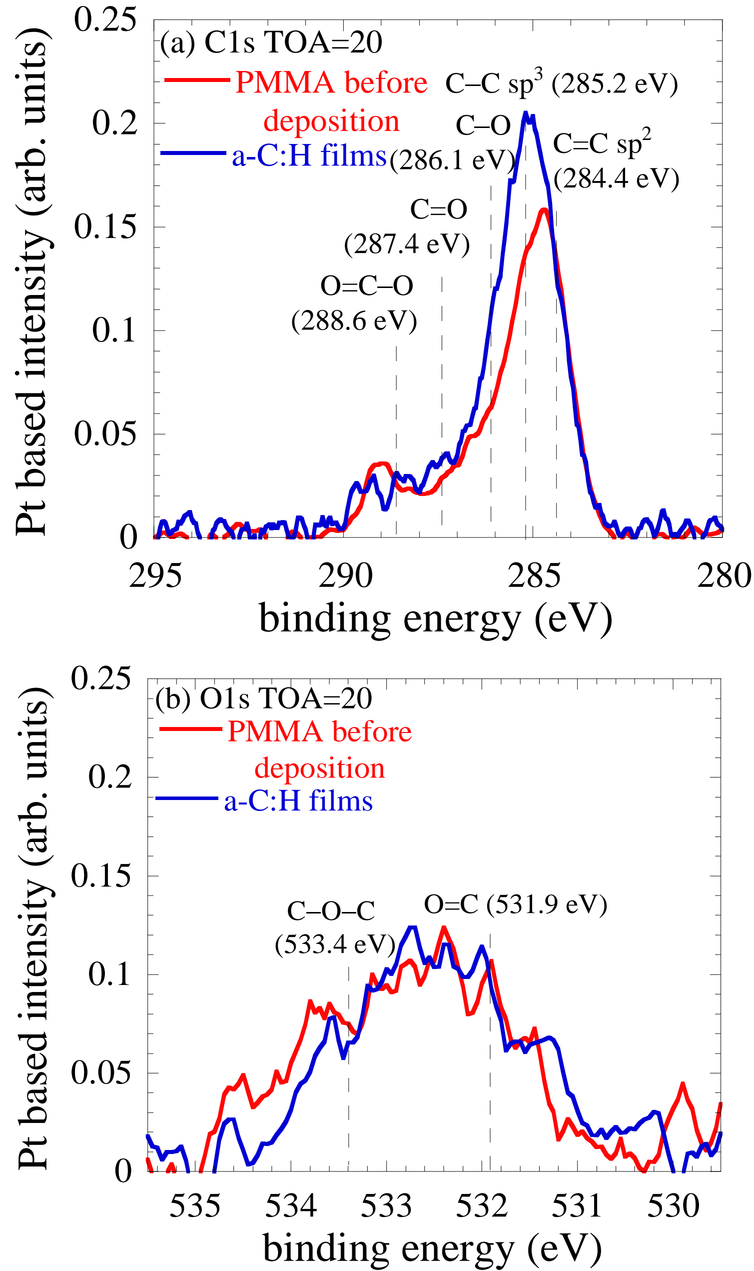

Fig. 6.6. Normalized spectra based on Pt of (a) C 1s and (b) O 1s at a detection angle of 20°.

6.4 Summary

We have deposited a-C:H films on PMMA by using the H-assisted plasma CVD method at a low substrate temperature of 100℃. The cross-section SEM images of deposited films shows a two-layer structure on Si substrate: the upper layer is a-C:H and

the lower layer is PMMA. This two layer structure may improve the low etch resistance of PMMA during plasma etching. Further experiments are required to deposit a-C:H films on other EUV photoresist materials using our method.

References:

[1] J.-P. Colinge, *FinFETs and Other Multi-Gate Transistors* (Chandrakasan, Cambridge, 2008).

[2] I. Ferain, C. A. Colinge, and j.-P. Colinge, Nature **479**, 310 (2011).

[3] A. E. Grigorescu and C. W. Hagen, Nanotechnology **20**, 292001 (2009).

[4] S. P. Beaumont, P. G. Bower, T. Tamamura, and C. D. W. Wilkinson, Appl. Phys. Lett. **38**, 436 (1981).

[5] P. P. Naulleau, C. Rammeloo, J. P. Cain, K. Dean, P. Denham, K. A. Goldberg, B. Hoef, B. L. Fontaine, A. R. Pawloski, C. Larson, and G. Wallraff, SPIE Proc. **6151**, 61510Y (2006).

[6] K. Takenaka, K. Koga, M. Shiratani, Y. Watanabe, and T. Shingen, Thin Solid Films **506-507**, 197 (2006).

[7] J. Umetsu, K. Koga, K. Inoue, H. Matsuzaki, K. Takenaka, and M. Shiratani, Surf. Coatings Technol. **202**, 5659 (2008).

[8] K. Koga, T. Urakawa, G. Uchida, K. Kamataki, Y. Seo, N. Itagaki, M. Shiratani, Y. Setsuhara, M. Sekine, and M. Hori, PSE Proc., 2012, p. 136.

[9] T. Urakawa, H. Matsuzaki, D. Yamashita, G. Uchida, K. Koga, M. Shiratani, Y. Setsuhara, M. Sekine, and M. Hori, Surf. Coatings Technol. **228**, S15 (2013).

[10] D. J. Li, F. Z. Cui, and H. Q. Gu, Appl. Surf. Sci. **137**, 30 (1999).

[11] Y.-B. Guo and F. C.-N. Hong, Diamond Relat. Mater. **12**, 946 (2003).

Chapter 7   Conclusions and Future Recommendations

7.1 Conclusions

To discuss deposition mechanism of a-C:H films, We investigated effects of gas pressure, discharge voltage, gas flow rate ratio, and ion bombardment (including ion flux and ion energy) using Ar + H_2 + C_7H_8 plasma CVD method, and characterized the deposited films by FTIR, HFS, XPS, and Raman spectroscopy. Firstly, we derived the plasma parameters in the bulk and related to spatial profiles by measurement of emission intensities by OES. The generation rates of plasma species are higher near the mesh powered electrode of the main discharge. For gas pressure, the effective electron temperature, Ar $1s_5$ metastable density and/or low-energy electron density decrease significantly with increasing the total pressure from 0.1 to 5 Torr, whereas they are almost constant irrespective of the spatial distance. For discharge voltage, the effective electron temperature remains nearly the same, and Ar $1s_5$ metastable density and/or low-energy electron density increase with increasing the discharge voltage from 150 to 180 V. For gas flow rate ratio, the effective electron temperature is constant, Ar $1s_5$ metastable density and/or low-energy electron density decrease with increasing the gas flow rate ratio from 11 to 55%.

Then the deposition rate of a-C:H films was studied, it increases from 3.7 to 94.5 nm/min. In a range of 0.1−5 Torr, the high deposition rate is obtained at the pressure of 5 Torr. Moreover, the deposition rate increases with increasing the discharge voltage from 150 V to 170 V, whereas it decreases significantly with increasing the discharge voltage from 170 V to 180 V. The decrease in deposition rate at 180 V is mainly attributed to a slight increase in radical generation rate and significant increases in etch rate by H atoms. By control of gas flow rate ratio and distance from the substrate electrode, the high

deposition rate is obtained at 20 mm for the gas flow rate ratio of 11%. From the above, we can see that the highest deposition rate is obtained under the conditions of gas pressure of 5 Torr, discharge voltage of 170 V, gas flow rate ratio of 11%, and distance of 20 mm from the substrate electrode.

We also studied the deposition mechanisms of soft and hard a-C:H films by ion bombardment experiments. The hydrogen bonding configurations in a-C:H films are closely related to the ion energy, whereas they are less dependent on ion flux. The structural transition of a-C:H films from soft PLCH to hard DLCH above the threshold ion energy of 84 eV. Moreover, the mass density of PLCH films deposited from without ion bombardment to the ion energy of 84 eV only depends on C–H sp^3 to C–H sp^2 ratio (H content) in films, while the mass density of DLCH films deposited in the ion energy range of 84 to 114 eV simultaneously depends on C–H sp^3 to C–H sp^2 ratio (H content) and C–C sp^3 to C=C sp^2 ratio in films. The highest mass density of 1.92 g/cm^3 is obtained at the ion energy of 109 eV. The characterization in film structure, H content, and mass density of our deposited a-C:H films can be greatly simplified using Raman spectroscopy.

Finally, we succeeded in depositing a-C:H films on PMMA at a low substrate temperature of 100℃. This a-C:H films as protective coatings are expected to overcome resolution limit of EUV lithography process and improve the low etch resistance of PMMA during plasma etching.

7.2 Future Recommendations

We have found out the conditions for depositing soft PLCH films with low deposition rate and hard DLCH films with high deposition rate, which is the key to obtain anisotropic deposition profiles. On the basis of this, we will challenge to realize more profiles of anisotropic deposition, especially the profiles (carbon deposited in trenches with top and

sidewall deposition) employed as protective coatings on nano-patterned photoresists. In section 4.2.2, more experiments are needed to elaborate on reasons of the increase in deposition rate at 5 Torr, especially for high substrate position. In section 5.3.2, Owing to the limitation of performance the apparatus, bias voltage is only able to reach to -80 V. The voltage of -200 V is expected to better study the effects of ion bombardment. In section 6.3, considering the differences in characteristics for different photoresists, further experiments are required to deposit a-C:H films on other photoresist materials such as poly(methyl glutarimide) (PMGI), phenol formaldehyde resin (DNQ/Novolac), and SU-8 [1].

Now the anisotropic plasma CVD apparatus in our laboratory is relatively large (240 mm in diameter), which leads to the discharge is difficult to sustain under high pressure condition. Minimal fabrication is required for high deposition rate, which indicates an atmospheric plasma deposition without vacuum pump would be better [2]. Moreover, the wafer of half-inch size suggests miniaturization of the apparatus. Therefore, it is necessary to develop a new apparatus about 50 mm in diameter that could sustain discharge under atmospheric condition. In this way, the realization of anisotropic plasma CVD for miniaturized high speed processes is aimed at.

References:

[1] A. del Campo and C. Greiner, J. Micromech. Microeng. **17**, R81 (2007).

[2] A. M. Ladwig, Ronald D. Koch, E. G. Wenski, and R. F. Hicks, Diamond Relat. Mater. **18**, 1129 (2009).

Acknowledgements

First and foremost, I would like to thank my thesis advisor Prof. Masaharu Shiratani for his wise guidance, kind support, teachings, and encouragement which motivated me during the time I was a researcher, and PhD student at his active laboratory. I appreciated all fruitful discussions I had with Prof. Shiratani, which kept me interested and curious about my research filed.

I am grateful to Prof. Kazunori Koga for all his valuable teachings, kind support, encouragement, and friendship. Prof. Koga’s valuable teachings and guidance were indispensables to me to sharpen my research skill at the laboratory.

I would like to thank the thesis defense committee member Prof. Tatsuo Okada. I would like to thank Prof. Yuichi Setsuhara, Prof. Makoto Sekine, Prof. Masaru Hori, and Prof. Kosuke Takenaka for fruitful discussions and encouragement.

I would like to thank Prof. Naho Itagaki, Prof. Giichiro Uchida, and Prof. Hyunwoong Seo for their help on experiments and valuable data analysis; as well as Mrs. Chizuru Onishi, Mrs. Keiko Konishi, Mrs. Kei Yamaki, and Mr. Daisuke Yamashita for their friendship and kind support.

I would like to thank JSPS KAKENHI Grant Number 26246036 and Japan Student Services Organization (JASSO) for all their support.

I would like to thank parents and all friends who supported me and encouraged me.

Xiao Dong

Dec. 15, 2015

Kyushu University

List of Publications

1. Deposition of Carbon Films on PMMA Using H-assisted Plasma CVD.

   JPS Conf. Proc. **1** (2014) 015072 (2013 年 7 月)

   共著者 Ryuhei Torigoe, Kazunari Koga, Giichiro Uchida, Naho Itagaki, Masaharu Shiratani, Kosuke Takenaka, Yuichi Setsuhara, Makoto Sekine, and Masaru Hori.

2. Pressure Dependence of Carbon Film Deposition Using H-assisted Plasma CVD.

   ICRP-8 Proc. (2014) 5P-PM-S08-P14 (2014 年 2 月)

   共著者 Kazunari Koga, Daisuke Yamashita, Hyunwoong Seo, Naho Itagaki, Masaharu Shiratani, Kosuke Takenaka, Yuichi Setsuhara, Makoto Sekine, and Masaru Hori.

3. Emission spectroscopy of Ar + H_2 + C_7H_8 plasmas: C_7H_8 flow rate dependence and pressure dependence.

   J. Phys.: Conf. Ser. **518** (2014) 012010 (2014 年 6 月)

   共著者 Kazunari Koga, Daisuke Yamashita, Hyunwoong Seo, Naho Itagaki, Masaharu Shiratani, Yuichi Setsuhara, Makoto Sekine, and Masaru Hori.

4. Formation of carbon nanoparticle using Ar+CH_4 high pressure nanosecond discharges.

   J. Phys.: Conf. Ser. **518** (2014) 012020 (2014 年 6 月)

   共著者 Kazunari Koga, Shinya Iwashita, Uwe Czarnetzki, and Masaharu Shiratani

5. Effects of discharge voltage on the characteristics of a-C:H films prepared by H-assisted Plasma CVD method.

   Trans. Mat. Res. Japan **40** (2015) 123 (2015 年 7 月)

   共著者 Kazunori Koga, Daisuke Yamashita, Hyunwoong Seo, Naho Itagaki, Masaharu Shiratani, Yuichi Setsuhara, Makoto Sekine, and Masaru Hori.

6. Raman Spectroscopy of a-C:H Films Deposited Using Ar + H_2 + C_7H_8 Plasma CVD.

ICRP-9 Proc. (2015) GT1.00145 (2015 年 10 月)

共著者　Kazunari Koga, Daisuke Yamashita, Hyunwoong Seo, Naho Itagaki, Masaharu Shiratani, Yuichi Setsuhara, Makoto Sekine, and Masaru Hori.

7. Effects of deposition rate and ion bombardment on properties of a-C:H films deposited by H-assisted plasma CVD method.

   Jpn. J. Appl. Phys **55** (2016) 01AA11 (2015 年 11 月)

   共著者　Kazunori Koga, Daisuke Yamashita, Hyunwoong Seo, Naho Itagaki, Masaharu Shiratani, Yuichi Setsuhara, Makoto Sekine, and Masaru Hori.